$NaTi_2(PO_4)_3$ as an Aqueous Anode: Degradation Mechanisms and Mitigation Techniques

Submitted in partial fulfillment of the requirements for

the degree of

Doctor of Philosophy

in

Materials Science and Engineering

Alexander I Mohamed

B.S., Materials Science and Engineering, Carnegie Mellon University
M.S., Materials Science and Engineering, Carnegie Mellon University

Carnegie Mellon University
Pittsburgh, PA

February, 2017

Acknowledgements

I would like to start by expressing my sincere gratitude towards my advisor, and former employer, Professor Jay Whitacre for all of the support he's provided me since I began research with him in as an undergraduate in 2008.

I'd also like to thank my committee members, Professor Bettinger, Professor Litster, and Professor Pistorius, for their time, feedback, and encouragement.

I'm sincerely grateful for the labmates I've had for the past several years, Han, Patrick, Sarah, Sneha, and Wei. They've helped keep me sane and provided me with endless entertainment in the lab over the years. I'd also like to thank the many others I've worked with in my lab, or theirs over the past several years.

Lastly, I'd like to thank my family, friends, and girlfriend for supporting me not only during my PhD but in life in general.

Abstract

With the proliferation of renewable energy sources, there has been a growing interest in battery chemistries for grid scale energy storage. Aqueous sodium ion batteries are particularly interesting for large scale energy storage because of their low cost and high safety, however, they tend to show poor long term stability. $NaTi_2(PO_4)_3$ shows promise as an anode for these systems with excellent long term stability when cycled quickly. When cycled slowly, $NaTi_2(PO_4)_3$ shows rapid capacity fade. The reasons for this rate depend capacity fade is poorly understood and is the topic of this document. It has been found that the products of the hydrogen evolution reaction, $H_2(g)$ and OH^-, are the two largest contributors to capacity fade. High electrolyte pH caused by generation of OH^- promotes dissolution of NTP during extend cycling, this is exacerbated when the pH increase above 11. The single greatest cause of apparent capacity fade for this material is loss of electrochemical surface area due to hydrogen gas entrapment within the porous structure of the electrode. Capacity lost in this manner can be recovered through reinfiltration of the electrode. The detrimental effects of gas entrapment within the electrode can be partially mitigated through compositing of the electrode with activated carbon and enhancing the wettability of the pores through addition of a surfactant to the electrolyte.

Table of Contents

List of Figures

Chapter 1: Introduction

1.1 Motivation

Large-scale energy storage is needed for the deployment of grid-tied and distributed renewable energy sources such as solar installations and wind farms, which rely on power generation that is inherently intermittent. For this kind of storage, the single most important performance attribute is the levelized cost of energy (LCOE) which is a measure of the total energy stored over the lifetime of an energy system per cost of that energy system (generally given as kilowatt-hours of energy delivered per dollar spent). As such, long life and robustness through thousands of use cycles are critical attributes. Because of this, battery researchers have sought to develop low cost, easy to manufacture battery chemistries that are composed of benign materials and have the necessary long-term stability[1,2]. Currently available commercial aqueous battery chemistries, such as lead acid (PbA), and nickel metal hydride (Ni-MH), are ill-suited for use in large-scale stationary energy storage applications. In the case of lead acid batteries, although the cost per kilowatt-hour is low when compared to Li-ion chemistries or the Ni-MH, their poor cycle life and high toxicity makes them undesirable for large installations[3,4]. The poor deep cycle life of PbA batteries is primarily caused by the continual decomposition of electrolyte as well as the thick insulating layers $PbSO_4$ formed on both electrodes during deeper discharge conditions. In the case of using PbA for energy storage of renewables, where it is desirable to allow the battery fully discharge when power may not be generated for long periods of time, the latter problem of deep-discharge becomes unavoidable. Ni-MH batteries are quite expensive due to the materials used and also suffer from relatively poor cycle life due to continual pulverization of the metal hydride materials upon cycling. Li-ion batteries by comparison offer higher energy densities, and for certain chemistries, much longer cycle life, though the highest performing cells have a

commensurately high cost per kilowatt-hour and poor safety when used improperly[1]. One analyses suggested that Li-ion battery manufacturing defect rates are roughly 1 in 10 million[5]. Although this is an exceptionally low rate, when considering a multi MWh storage installation, there is a relatively high probability of having a defective cell that might lead to a larger system failure or even catastrophic thermal runaway.

Aqueous alkali-ion batteries have attracted much attention in recent years as an attractive alternative to Li-ion batteries for grid-scale energy storage[6–26]. The primary electrochemical reactions of aqueous alkali-ion batteries are equivalent to those that occur in organic based Li-ion batteries. During these reactions, the cation (Li^+, Na^+, K^+) is transferred from the electrolyte into the host structure of the active material. However, due to the smaller stability window of water compared to organic electrolytes, there are fewer choices for what electrode materials can be used. For instance, the most common anode used in Li-ion batteries is graphite, but the potential at which lithium ions intercalate into the graphite layers is about 2.5 V below the potential at which the hydrogen evolution reaction (HER) occurs in neutral pH aqueous electrolytes. As such, graphite cannot act as an active material in aqueous systems.

Although aqueous systems have a more limited voltage stability window and consequently a lower energy density, their cost per kilowatt-hour can be much lower than that of traditional Li-ion cells. This is due not only to the lower cost of water compared to organic electrolytes, but also the less stringent manufacturing conditions, and the higher conductivity of aqueous electrolytes allowing for thicker electrodes and consequently a higher ratio of active material to

ancillary materials in the battery. Relatively expensive polyolefin based separators can also be replaced with cheaper glass fiber or non-woven cellulose separators[27–30].

Aqueous systems are also inherently much safer, aside from being non-flammable they are considerably less toxic and don't pose as large of an environmental hazard, particularly if neutral pH electrolytes are used. However, several hurdles must still be overcome before aqueous alkali-ion batteries can truly be commercialized. In particular, while some cathode systems have exhibited many thousands of stable cycles without loss in function[7,31–33], materials that exhibit useful reversible electrochemical capacity at anode potentials, with the exception of activated carbon, tend to lose function over tens or several hundred cycles, particularly when cycled slowly and deeply[29].

The most interesting class of anode active materials for aqueous anodes are polyanionic framework type titanium phosphates such as $NaTi_2(PO_4)_3$ (NTP), $LiTi_2(PO_4)_3$ (LTP), and TiP_2O_7 (TPO) [10,11,23,24,34–37]. These materials offer redox potentials in the desirable range (allowing for a high voltage cell), have high ionic conductivies, and relatively low costs of production. However, the low redox potentials of these materials puts them near or below the hydrogen evolution potential in neutral pH conditions. Of these materials, NTP with a theoretical capacity of 133 mAh/g and the ability to replace lithium salts with sodium equivalents should offer a cost-effective alternative to the lithium equivalent. However, this material, as well as LTP and TPO, commonly exhibit significant capacity fade, especially when cycled deeply/slowly (Figure 1.1), and the phenomena responsible for this loss in function remain poorly understood[38–40]. This failure has been attributed to the dissolution of active material,

irreversible phase changes, H_2 evolution from the decomposition of water, and/or self-discharge due to direct interactions with H_2O or dissolved oxygen[29]. While several papers have claimed significant improvements when cycling in low oxygen electrolytes, a loss in capacity during low rate deep cycling persists, and fundamentals behind this loss have not been deeply examined to date.
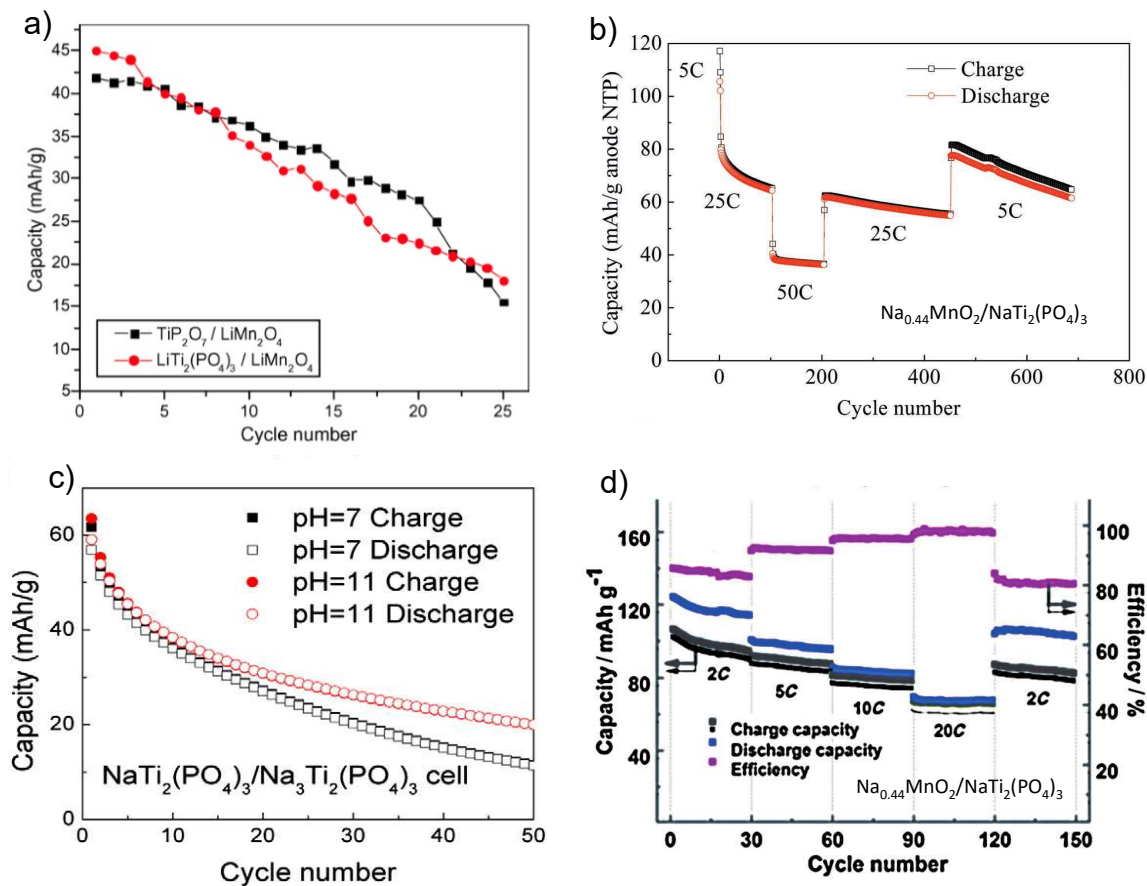
Figure 1.1 (a) Cells prepared with TPO and LTP in 5 M LiNO₃, (b) a cell prepared with NTP that shows a higher rate of capacity loss as low rates than higher rates, (c) a symmetric cell of NTP showing rapid capacity fade in neutral and high pH conditions, and (d) a cell prepared with NTP showing no capacity fade at a 20C rate, but moderate fade at rates of 2 C and 5 C. Graphs from[23,38–40]

1.2 Main Question to Answer

1) Do NTP electrodes suffer from dissolution of the active material at high pH? If so, at what pH does this become a concern?

2) How does the performance of NTP change after exposure to high pH electrolytes?

3) To what extent does the pH of electrolyte within an aqueous NTP anode change under normal operating conditions?

4) How does gas generation affect the cycling stability of NTP based aqueous anodes?

5) After determining what mechanisms are primarily responsible for loss of capacity upon cycling, what methods can be used to mitigate these degradation mechanisms?

1.3 Hypotheses

1) $NaTi_2(PO_4)_3$ will be soluble in high pH electrolyte solutions especially at high temperature.

2) pH swings in neutral electrolyte caused by electrochemical proton reduction from water and the direct chemical reaction between $Na_3Ti_2(PO_4)_3$ and water will lead to a dissolution precipitation reaction.

3) Hydrogen gas generated at the anode when below the hydrogen evolution potential will become trapped in the porous electrode structure leading to loss of electrochemical surface area, and consequently a loss of capacity.

4) Application of polymeric coatings and carbon coatings can prevent the problem of $NaTi_2(PO_4)_3$ dissolution in high pH electrolytes.

5) Addition of activated carbon to electrode composites of $NaTi_2(PO_4)_3$, and modification of the wetting characteristics of the electrode material will help mitigate loss of ECSA due to entrapment of hydrogen gas.

6) By enhancing the wettability of an NTP based electrode through addition of a surfactant to the electrolyte, we will be able to modify the effect of trapped hydrogen gas on ECSA.

Chapter 2: Background and Literature Review

2.1 Basics of Batteries

A battery is a device that converts chemical energy into electrical energy via a controlled reduction-oxidation (redox) reaction. In the case of a secondary, or rechargeable battery as it's more commonly known, this redox reaction is reversible. The elementary unit of a battery is known as a cell, with a battery consisting of one or more cells connected in series and parallel to obtain a desired voltage, capacity, and current rating for the given application. Generally speaking an electrochemical cell consists of three components: an anode or negative electrode, a cathode or positive electrode, and an electrolyte that allows ions to be transported from one electrode to the other. On top of this, most anodes and cathodes are porous composites consisting of three primary materials: the active material that undergoes the redox reaction, a conductive additive that allows electrons to be transported in/out of the active material, and a binder material that holds everything together and ensures the mechanical integrity of the electrode composite. Figure 2.1 illustrates the basic components of an electrochemical cell.

Anode Current Collector

Anode

Separator

Cathode

Cathode Current Collector

Active Material

Polymeric Binder

Conductive Carbon Additive

Electrolyte Filled Pore
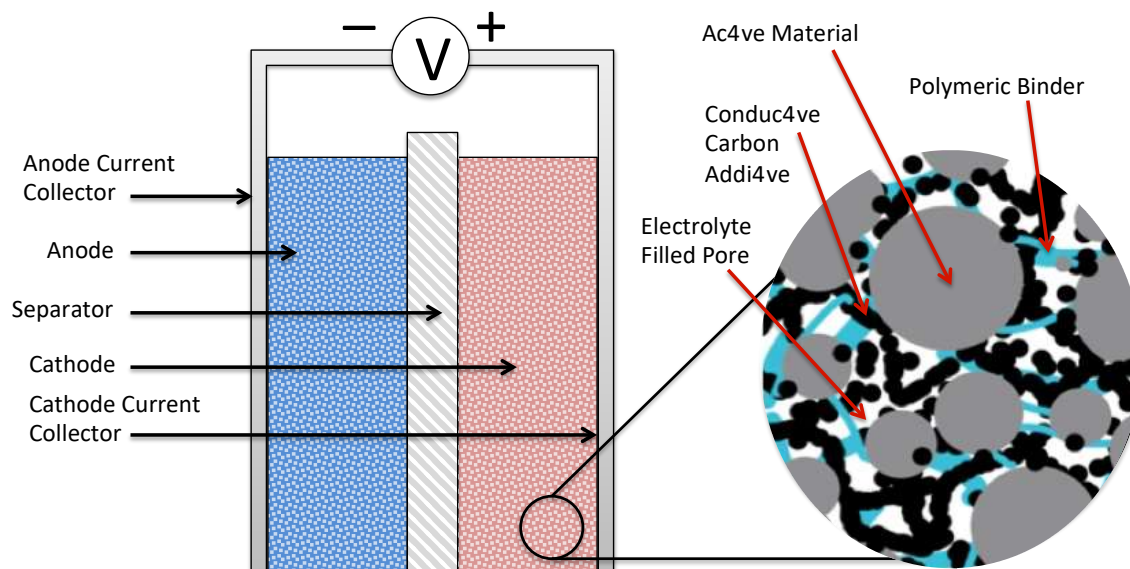
Figure 2.1 Schematic representation of a basic electrochemical cell with an enlarged view of the electrode composite.

In commercial cells, there are several more components that are necessary to have a working battery: including two current collectors (one for the anode and one for the cathode), a separator that prevents electrical contact between the anode and cathode while allowing ion transport between the anode and cathode, terminals (leads) that allow for an electrical connection between the device being powered and the current collectors, packaging material to keep the entire assembly contained, and generally some manner of safety features to prevent excess gas build up and/or thermal runaway. Figure 2.2 shows the complex design of a modern Li-ion cylindrical cell.
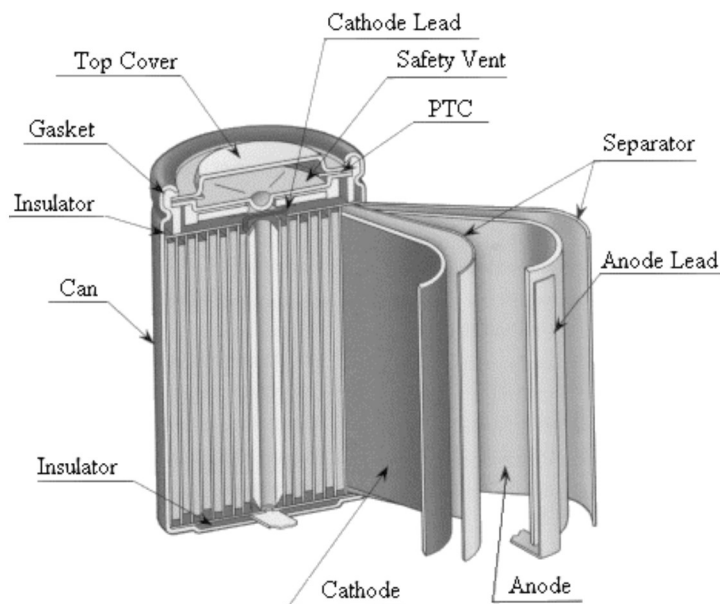
Figure 2.2 Cutaway schematic of a Li-ion cylindrical cell showing the large number of components that go into producing a commercial battery[3].

2.1.1 Operation

When an electrical connection is made between the anode and cathode of a battery, electrons will be removed from the anode as it is oxidized, travel through the external load that is making the electrical connection, and enter the cathode, which will then be reduced. This process is known as discharge. A simple example of a cell discharge would be a Zinc-Chlorine cell. Below are the two half-cell reactions and the full cell reaction.

At the anode or negative electrode: $Zn \rightarrow Zn^{2+}(aq) + 2e^-$

At the cathode or positive electrode: $Cl_2 + 2e^- \rightarrow 2Cl^-(aq)$

The full cell reaction: $Zn + Cl_2 \rightarrow Zn^{2+}(aq) + 2Cl^-(aq)$

The reverse reaction is known as the charge process. In the reactions given for the Zn/Cl_2 cell, there are no solid discharge products, only solvated ions, and the electrolyte does not take part in

the redox reactions, acting only to allow for ion transport. More complicated reactions can take place, however. Take for example the lead-acid battery:

At the anode: $Pb + HSO_4^-(aq) \leftrightarrow PbSO_4 + H^+(aq) + 2e^-$

At the cathode: $PbO_2 + 2HSO_4^-(aq) + 3H^+(aq) + 2e^- \leftrightarrow PbSO_4 + 2H_2O$

Full cell reaction: $Pb + PbO_2 + 2HSO_4^-(aq) + 2H^+(aq) \leftrightarrow 2PbSO_4 + 2H_2O$
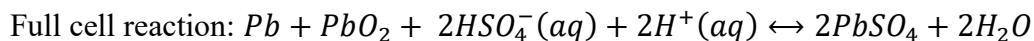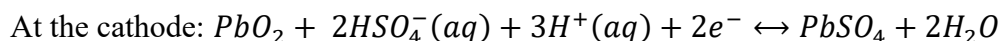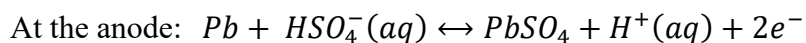
In this case, the sulfuric acid electrolyte is consumed during the discharge process producing lead sulfate at both electrodes and generating water through reaction of protons with the oxygen at the cathode. At the anode metallic lead is oxidized to Pb^{2+} and reacted with sulfate, and at the cathode lead oxide is reduced from Pb^{4+} to Pb^{2+} and reacted with sulfate.

Unlike PbA and Ni-MH cells, Li-ion and aqueous alkali-ion batteries do not utilize conversion reactions that fundamentally change the structure of the active materials but operate through intercalation of alkali ions into the host structure. Batteries that use this mechanism of operation are commonly termed as 'rocking chair' batteries. Figure 2.3 shows how this process works. Active materials that utilize this mechanism, known as insertion compounds, share one common feature: free volume within the structure that allows for easy diffusion of the alkali-ion. This free volume may be in the form of tunnels or space between layers of the active material; the important thing is that the free volume allows incorporation of ions without excess expansion of the structure and without fundamentally altering the bonding of the structure. Upon insertion/removal of an alkali ion into the structure, the oxidation state of the transition metal

cation is decreased/increased, all without changing the bonding environment of the transition metal.
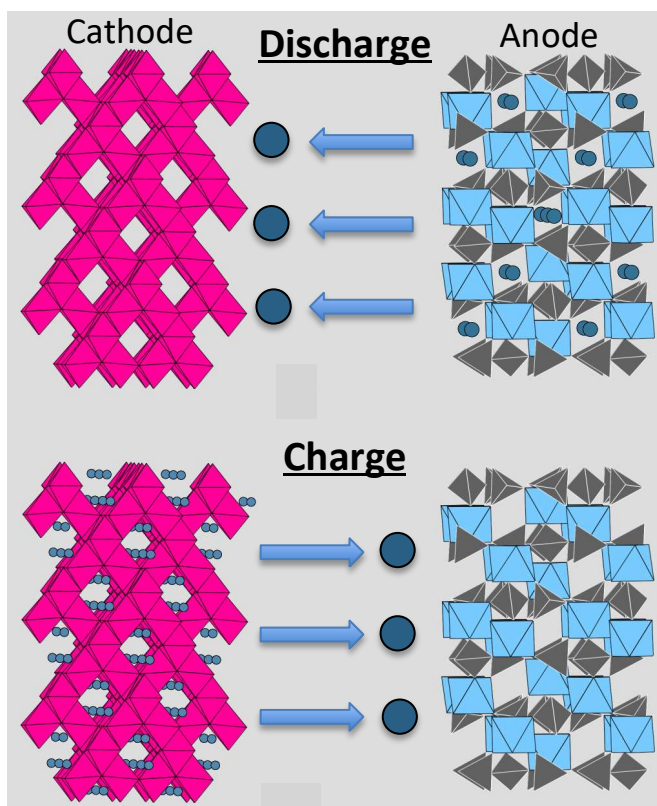
Figure 2.3 Schematic representation of the ion insertion and removal process for a rocking chair battery.

2.1.2 Thermodynamics

From thermodynamics we know that there is a decrease in free energy of a system any time a spontaneous reaction is allowed to proceed. This is most commonly given as the Gibb's free energy of reaction. There is a simple equation that relates the Gibb's free energy of a reaction to the electric potential of that reaction:

$$\Delta G^0 = -nFE^0$$

In this equation ΔG^0 is the Gibb's free energy of reaction, n is the number of moles of electrons transferred in the reaction, F is Faraday's constant that relates the number of Coulombs of charge

to the moles of reactants (96485 C/mol), and E^0 is the standard (theoretical) potential of the reaction. By convention the standard potential of the H_2/H^+(aq) is taken to be equal to zero; so you'll commonly see standard potentials reported as being some potential with respect to the standard hydrogen electrode (SHE). The standard potential of certain reactions can be found in tables but are given under the assumption of a temperature of 298 K. In order to account for deviations due to non-unit activity and non-standard temperatures the Nernst equation should be used. Consider a simple reaction:

$$a \cdot A + b \cdot B \leftrightarrow c \cdot C + d \cdot D$$
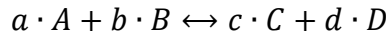
The Nernst reaction for this equation would be:

$$E = E^0 - \frac{R \cdot T}{n \cdot F} \ln(\frac{a_C^c \cdot a_D^d}{a_A^a \cdot a_B^b})$$

Where a_i^j is the activity of species i raised to the stoichiometric coefficient j, R is the gas constant, and T is the temperature in kelvin. For battery materials, the ratio of material that has been oxidized/reduced to the total amount of material is commonly known as the state of charge (SoC) and is given as a percentage. Take for example cubic spinel $LiMn_2O_4$ (LMO), which is of interest as a cathode material for Li-ion batteries. The reaction of LMO during charging/discharging is:

$$LiMn_2O_4 \leftrightarrow xLi^+ + Li_{1-x}Mn_2O_4 + xe^- \quad 0 \leq x \leq 1$$
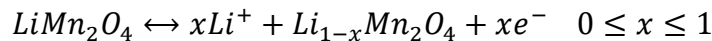
When x = 1, LMO has a 100% SoC. If LMO were capable of transferring 2 lithium during this reaction then when x = 2 LMO would be at 100% SoC. For insertion compounds it is useful to write the Nernst equation as a function of the fraction of filled sites within the host lattice.

$$E = E^0 - \frac{R \cdot T}{n \cdot F} \ln(\frac{x}{1 - x})$$

12

Figure 2.4a gives a qualitative representation of the potential, Gibb's free energy, and chemical potential versus the state of charge of a standard electrode. Certain insertion compounds, such as LiFePO$_4$ undergo phase separation during oxidation/reduction. This particular form of phase separation is known as spinodal decomposition. In order to account for this phase separation, a modification of the Gibb's free energy must be made, which consequently changes the chemical potential and the equilibrium potential of the Nernst equation. The practical effect of this phase separation is that the equilibrium potential of the redox reaction will be constant within the spinodal region. Figure 2.4b shows how phase separation affects the potential, Gibb's free energy, and chemical potential.
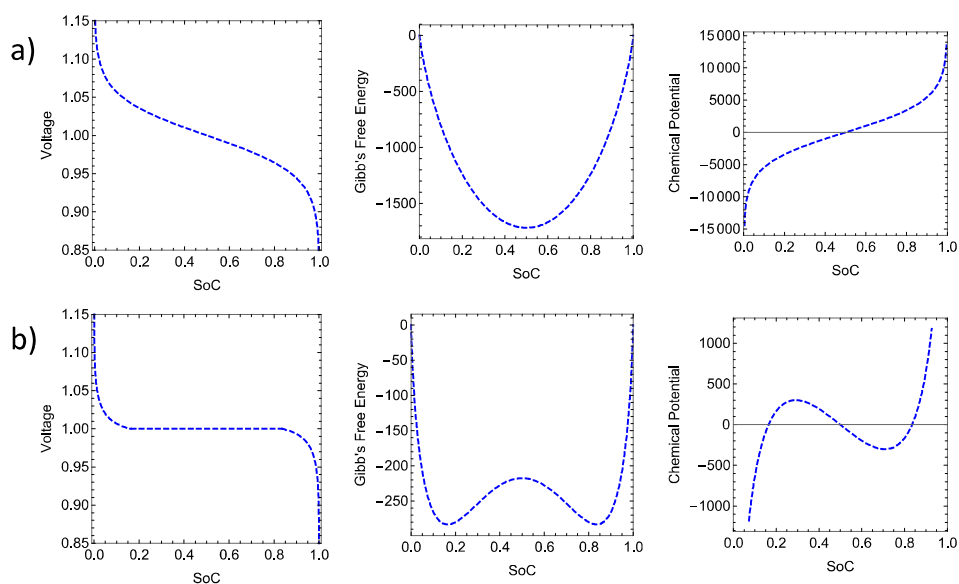
Figure 2.4 (a) The first row of figures shows a qualitative representation of the voltage, Gibb's free energy, and chemical potential as a function of SoC for an electrode that acts as a solid solution. (b) The second row shows the same properties for an electrode that undergoes spinodal decomposition into two separate phases (figures created in Wolfram Mathematica).

For a given material, we can also define the theoretical specific capacity available from carrying the redox process of interest to completion. Let us consider LMO. The molecular weight of LMO is 180.81g/mol and it is capable of transferring exactly 1 mole of lithium per mole of LMO. In order to calculate the specific capacity we simply multiply the number of moles of electrons

transferred by Faraday's constant, divide by the molecular weight, and divide by the number of coulomb's per mAh.

$$\frac{n \cdot F}{M_{LMO} \cdot 3.6} = \frac{1 \cdot 96485(\frac{C}{mole})}{180.81(\frac{g}{mole}) \cdot 3.6(\frac{C}{mA}h)} = 148 \; mAh/g$$

So the theoretical capacity for LMO is 148 mAh/g. The theoretical specific capacity is important for comparing the potential performance of different electrode materials. It also gives a starting point for deciding on what mass ratios of anode to cathode active materials should be used, since both electrodes should have roughly the same capacity in order to maximize the usage of material.

2.1.3 Non-equilibrium Effects

Although the standard potential of a cell can be determined from simple thermodynamic considerations, the practical voltage of a cell generally deviates drastically from this thermodynamic equilibrium potential. This deviation occurs because of the resistances related to the numerous processes occurring within the cell during charge and discharge. Deviations from the equilibrium voltage due to these resistances are known as overpotentials or polarizations. There are three overpotentials that should be considered when defining the actual voltage of an electrochemical cell: surface or activation overpotential, concentration overpotential, and ohmic overpotential. The activation overpotential is related to chemical kinetics, the available surface for the reaction to take place, and the activation barrier that must be overcome to drive the reaction of interest in one direction of the other. Concentration overpotential has to do with how quickly mass transport can occur through the electrolyte and solid phase and is dependent on the diffusional properties of the electrolyte, electrodes, and separator. The ohmic overpotential is

related to the electronic resistance of the electrodes and current collector, as well as the DC ionic resistance of the electrolyte, and will scale linearly with the applied current. These overpotentials must be accounted for at both electrodes, and the ohmic overpotential must also be accounted for at the current collectors and through the separator. A qualitative depiction (taken from reference [41]) of how these overpotentials affect the voltage profile of a battery is given in Figure 2.5a. In this figure, the solution, contact, and matrix resistance represent the ohmic part of the overpotential, the kinetic resistance represents the activation or surface overpotential, the diffusion resistance represents the concentration overpotential, and the upside down triangles represent the calculated voltage profile including all of these resistances. Figure 2.5b shows calculated voltage profiles, including all overpotentials, when the battery is operated at different currents.

$$V = E - (\eta_{sa} + \eta_{sc}) - (\eta_{ca} + \eta_{cc}) - i \cdot R$$

V = Voltage of the cell

E = Thermodynamic equilibrium potential given by the Nernst Equation

η_{sa} and η_{sc} = activation overpotential at the anode and cathode respecitvely

η_{ca} and η_{cc} = concentration overpotential at the anode and cathode respectively

i = operating current

R = internal resistance of the cell including electronic and DC ionic resistances

So in order to obtain the highest energy from a battery, it is important to minimize the overpotential losses.
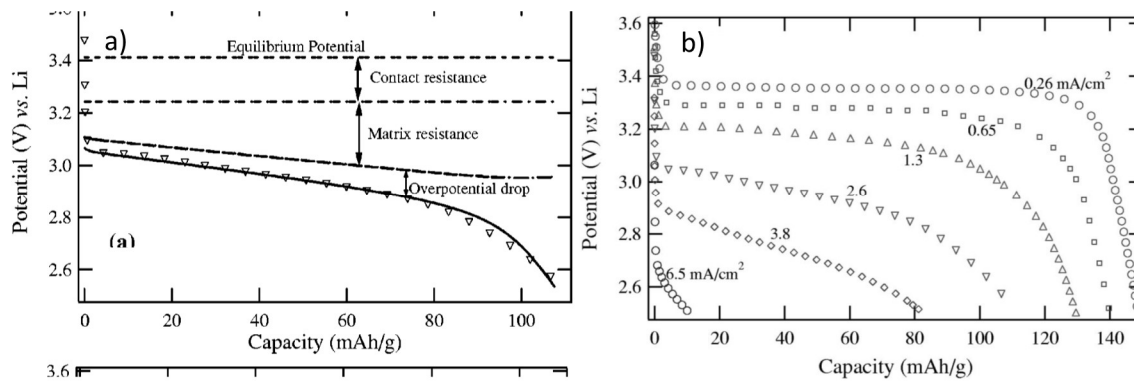
Figure 2.5 (a) Simulated overpotentials for a LiFePO$_4$ battery when run at a current density of 2.6 mA/cm^2 and their cumulative effect on the measure voltage. (b) The effect of overpotentials on the voltage at different current densities.[41]

2.1.4 The Electric Double Layer

In order to more fully discuss the kinetics and charge transfer in electrochemical systems, it is important to discuss the formation of what is known as the double layer. When an electrode is immersed in a solvent containing solvated ions (the electrolyte) the difference in electric potential between the electrode and the electrolyte will cause the ions in solution of opposite charge to the electrode to be attracted to the surface. The electrode will also cause an alignment of the solvent dipoles. In the case of a metal being place in electrolyte, the excess negative charge due to free electrons will cause the cations of the solution to be attracted to the surface. For the rest of the discussion we will assume that the electrode is negatively charged, but the mechanisms discussed hold for a positively charge electrode as well, with the cations being replaced by anions. The cations attracted to the surface are also accompanied by what is known as a solvation shell, a layer of solvent ions that surrounds the solvated ion. Generally speaking, the free energy of the system is such that a single layer of solvent molecules will adsorb strongly to the surface of the electrode rather than the cations losing their solvation shell and adsorbing. This layer of adsorbed species is known as the stern layer and the plane that passes through the center of this layer is known as the inner Helmholtz plane (IHP). Outside of the stern layer will

16

be a layer of cations and their solvation shells. The plane that passes through these cations is known as the outer Helmholtz plane (OHP) and is the plane of closest approach for the ions in the electrolyte. Because the OHP will have a much higher concentration of cations than anions, the electric field that is attracting the ions will be partially screened. This implies that the next layer of attracted ions will have a lower ratio of cations to anions then the OHP. This screening continues outwards from the OHP until the concentration of cations becomes that of the bulk electrolyte. This layer of excess cation concentration is known as the diffuse layer and is characterized by what is known as the Debye length, which is the distance at which the electric field has decrease to $1/e$ compared to the field at the OHP. The Debye length is inversely proportional to square root of the ion concentration in the electrolyte. This is because higher concentration electrolytes contain more ions with which to screen the electric field. A qualitative representation of the electric double layer can be found in Figure 2.6. For batteries, where the concentration of the electrolyte tends to be high, the double layer is often ignored, though should be considered in cases where ion depletion has led to lower concentration of ions in solution.
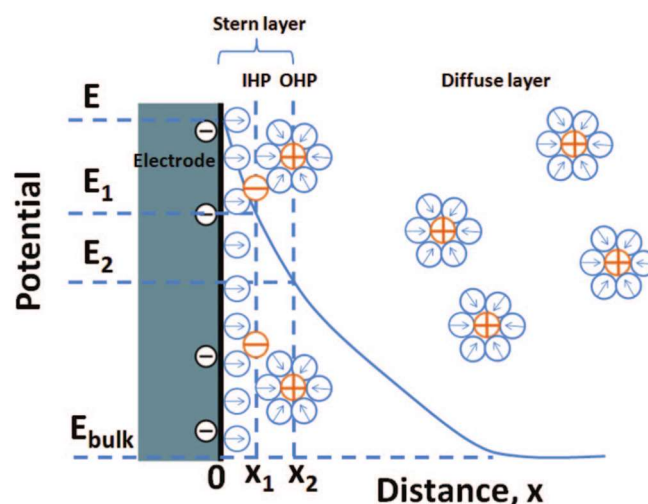
Figure 2.6 Qualitative representation of the electric double layer formed at a negatively charge surface.[42]

2.1.5 Activation Overpotential

The activation overpotential, also known as the surface overpotential or charge-transfer overpotential, is related to the kinetics of charge transfer at the surface of an electrode. It is most commonly modeled using the Butler-Volmer equation, though this is an empirical model and doesn't account for molecular reorganization energies of a system[43]. However, for most systems, under normal operating conditions the Butler-Volmer model is sufficient to describe charge transfer at the surface. The Butler-Volmer equation has its origins in chemical kinetics, in which it is assumed that there is some amount of forward and backward reactions occurring under equilibrium conditions. In order to drive the reaction in one direction or the other there should be some sufficiently large stimulus to push the system out of equilibrium. For electrochemistry, it is assumed that at the surface of an electrode there is always some amount of reaction occurring, but since both the forward and backward reaction are occurring at equivalent rates, zero current will be measured. The rate at which ions are being exchanged when zero current is flowing is known as the exchange current. This is generally normalized to the total surface undergoing electrochemical reactions, or the electrochemical surface area (ECSA), and called the exchange current density. In electrochemistry, negative currents imply that an electrode is undergoing reduction, and positive currents imply that the electrode is undergoing oxidation. The Butler-Volmer model assumes that there exists an activation barrier to charge transfer at the surface on an electrode, and that in order to overcome this barrier the electrode potential must be raised or lowered by some amount to obtain a desired current. The amount the potential is raised or lowered is known as the overpotential. It is normally assumed that this barrier is related to the Stern layer, and that in order for charge transfer to occur, and ion or electron must tunnel through the Stern layer. There is an exponential relationship between the

current generate and the applied overpotential, meaning that a relatively small current will run until a sufficiently large overpotential is applied, at which point the current will increase exponentially. Figure 2.7 illustrates the effect of applying an increasing overpotential on the height of the activation barrier. Note that after a sufficiently large overpotential is applied, the activation barrier for the reaction no longer exists.
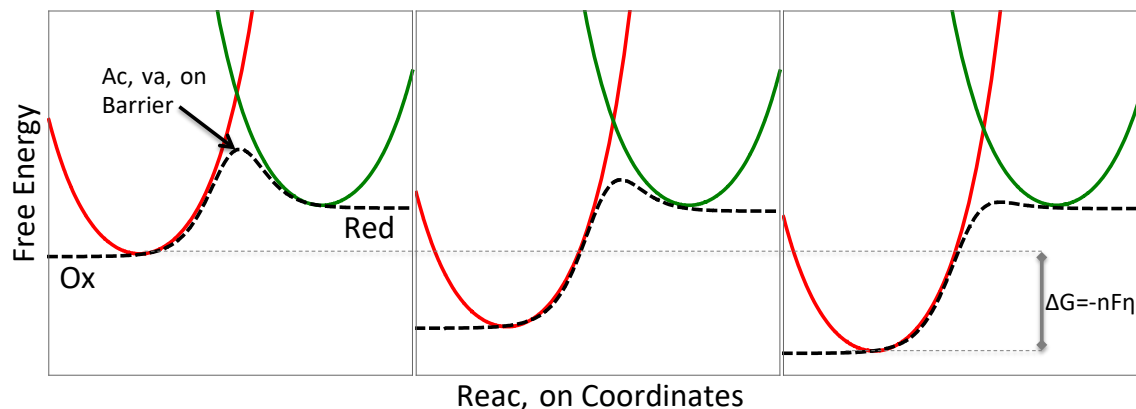
Figure 2.7 The black dotted line is the empirical representation of Butler-Volmer type charge transfer. Moving from left to right shows the effect increasing the overpotential has on the activation barrier.

The form of the Butler-Volmer equation that relates the current to the overpotential is:

$$i = i_0(e^{\frac{\alpha_a F}{RT}\eta_s} - e^{\frac{-\alpha_c F}{RT}\eta_s})$$

$$\eta_s = V - E$$

Here, i is the current density, η_s is the activation overpotential, V is the applied or measured voltage, E is the thermodynamic equilibrium potential given by the Nernst equation, i_0 is the exchange current density, and α_a and α_c are shape parameters with $\alpha_a = 1 - \alpha_c$. If the forward and backward reactions are assumed to be symmetric, than α_a and α_c are taken to be equivalent and equal to 1/2. Strictly speaking the shape parameter and the exchange current densities are considered to be fitting parameters for the empirical model, and as such cannot rationally describe the differences seen for different solvents or electroactive species.

2.1.6. Concentration Overpotential

Charging and discharging of an electrochemical cell implies that mass is being transported within the cell. Generally speaking, the rate at which a battery is being discharged is limited by the rate at which ions can be transport through the different components of the battery. For systems such as Li-ion batteries, where ions are being intercalated into and out of the electrodes a relatively simple picture describes the discharge of the cell: (1) upon creating an electrical connection between the anode and cathode, Li^+ will leave the anode material and enter the electrolyte while an electron will leave the anode (oxidation) and enter the current collector, (2) Li^+ in the electrolyte will begin to move through the electrolyte and separator due to both a concentration and potential gradient, and (3) an electron will enter the cathode from the current collector while a Li^+ will intercalate into the cathode material from the electrolyte (reduction). During this process mass transport is occurring in three primary regions, solid state diffusion of Li^+ is occurring in both the anode and cathode active materials and Li^+ transport is occurring through the electrolyte within the porous electrodes and porous separator. Because of the porous nature of the separator and electrodes, the diffusivity of Li^+ in the electrolyte must be given as an effective diffusivity. The diffusivity of Li^+ in the electrolyte is given as:

$$D_{Li}^{el} = D_0 \cdot e^{\frac{-Q}{RT}}$$

where D_0 is a characteristic diffusion coefficient related to the vibrational energy and intrinsic mobility of the ion, Q is the activation energy for hopping from one site to another, and R and T have their usual meanings. However, we must correct this ideal diffusion coefficient in order to account for the porosity (volume fraction of the electrode and separator filled with electrolyte)

and tortuosity (a measure of how far an ion must travel relative to a straight path). Correcting for these and calling it the effective diffusivity or D_{eff} we get:

$$D_{eff} = \frac{\varepsilon}{\tau} D_{Li}^{el}$$

where ε is the porosity of the region of interest, and τ is the toruosity of the region of interest. Note that ε will always be less than 1 and τ will be equal to or greater than 1, such that the effective diffusion coefficient is always smaller than the ideal. There are certain practical considerations that must be addressed when synthesizing and designing electrode materials: (1) if the active material particles are extremely large then the rate at which the electrode can be charged or discharged will be limited by the rate at which ions diffuse through particles, (2) it is possible to increase the volumetric energy density of an electrode by decreasing the porosity but this will limit the power density because of an increased concentration polarization, (3) if the effective diffusivity of an electrode is too small, depletion of the active ion within the pores during operation will cause a large drop in the conductivity of the electrolyte leading to a large increase in the ohmic polarization. There are many other aspects of mass transport that should be taken into consideration, such as preferential diffusion along certain crystallographic directions of particles, but to encompass all phenomenological aspects of mass transport in a battery are out of the scope of this document.

2.1.7 Ohmic Overpotential

Whenever a current is flowing in a material with a non-zero resistance, there will be a voltage drop that is directly proportional to the current being drawn. In a battery electrons must move through the solid phases of the porous electrodes, and through the current collectors, while ions

must move through the liquid phases. The relationship between current, conductivity, and potential drop can be defined by Ohm's law:

$$i = -\sigma_m \cdot \nabla \phi$$

Where i is the current, σ_m is the conductivity of the phase of interest, and $\nabla \phi$ is the gradient of the potential. Since the current collectors of batteries possess metallic conduction, unless extremely high currents are being considered, it is normally a good approximation to assume that their contribution to the electronic resistance is zero. However, the contact resistance between the electrode and the current collector can be quite large and should not be ignored. As stated earlier, battery electrodes consist of three primary components: active material, a conductive additive, and a binder material. Unless the active material has metallic or semi-metallic conduction, the conductive additive is responsible for the bulk of electronic conduction through the electrode structure. The conductivity of the electrode will exhibit a percolation type relationship between conductivity and volume fraction of conductive phase. This means that at low volume fractions of conductive additive the conductivity will increase relatively slowly until a critical volume fraction of conductive additive is added. At this point the conductive particles will begin forming connections that span the length of the conduction path and the conductivity will begin increasing exponentially. After the percolation threshold the conductivity will increase following a power law. Similar to porosity, increasing the volume fraction of conductive additive will increase the conductivity and power density of an electrode but at the same time decrease the energy density since there will less active material per volume. Because of this battery engineers tend to add enough conductive additive to pass the percolation threshold, but not much more unless the battery is being designed specifically for high power applications.

2.2 Degradation Mechanism in Aqueous Batteries

Since this work is primarily focused on understanding why NTP degrades when used as an aqueous anode, it is important to understand why other materials fail when used in aqueous electrolytes, and which of those mechanisms are relevant to NTP. We'll start by discussing the general modes of failure seen in aqueous alkali-ion chemistry and how this relates to failure in specific chemistries, and what has been tried to mitigate these failure mechanisms.

2.2.1 Dissolution and Fracture

Dissolution of the active material is a common problem found in aqueous alkali-ion batteries, particularly when transition metal oxides are used[9,26,44–46]. During the normal operation of a battery based on transition metals the metal cation will undergo reduction/oxidation during the insertion/removal of the alkali metal ion. It is possible that the transition metal will be insoluble or have extremely limited solubility in one oxidation state, but become highly soluble in another oxidation state. For example, Mn^{4+} in MnO_2 has very limited solubility in aqueous solutions over a wide range of pHs. However, upon reduction to Mn^{3+} it becomes unstable to a disproportionation reaction in which

$$2Mn^{3+} \rightarrow Mn^{2+} + Mn^{4+}$$

, where the Mn^{4+} will remain as MnO_2 but the Mn^{2+} will become solvated in the electrolyte[7,44,47]. This can lead to continual loss of manganese from the materials surface through each reduction/oxidation cycle and will cause rapid capacity fade. Figure 2.8 shows an electrochemical test cell before and after cycling, showing a drastic change in color of the electrolyte from clear to bright yellow due to dissolution of vanadium ions from LiV_3O_8[48].
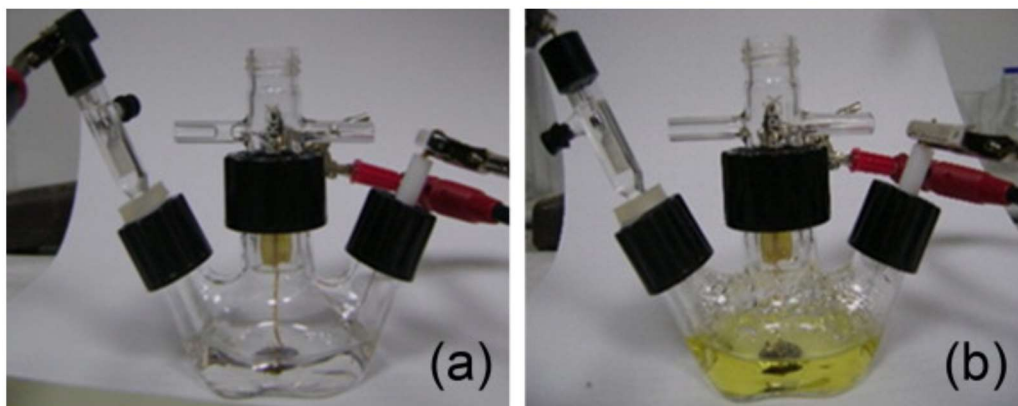
Figure 2.8 Before (a) and after (b) images of an electrochemical half-cell showing the drastic change in color cause by dissolution of vanadium ions from the LiV_3O_8 based working electrode.[48]

Loss of active material due to dissolution can be exacerbated by the use of nano-sized particles of active material. In order to minimize the diffusion path in the solid phase as well as decrease the ohmic losses and increase the electrochemical surface area (which will increase the exchange current), battery engineers will often try to synthesize nanoparticles of the active material in which they are interested. However, this will lead to an increase in the solubility of the active material for two reasons (1) the equilibrium solubility at a particles surface is inversely related to the radius of the particle (Gibbs-Thomson effect) [49]and (2) dissolution occurs at the particles surface and by decreasing the particle size you are increasing the surface to volume ratio of the material..

Electrode material may also undergo electrochemically induced fracture. During electrochemical cycling of intercalation electrodes, mass is being inserted and removed from the structure of the active material, with this mass transport there is an associated expansion and contraction of the host structure. The induced strain leads to a stress. If this stress becomes too large, the active material particles will fracture and lose electronic contact with the rest of the electrode structure (Figure 2.9a). The magnitude of the induced stress and strain is dependent on the particular

active material, the total quantity of inserted ions, and the nature of the redox process occurring.

For instance, cubic spinel LMO can exchange a total of one lithium during normal operation and

does so as a solid solution with 3D mass transport. This means that the cubic spinel exists as

$Li_xMn_2O_4$ with $0 \leq x \leq 1$, and that the diffusion of lithium through the structure occurs equally

quickly in all primary coordinates. Because of this, diffusion of lithium into or out of particles of

active materials such as LMO are generally modeled using a shrinking core type model. When

fully delithiated LMO has a cubic lattice parameter of 8.04 Å, and when fully lithiated LMO has

a cubic lattice parameter of 8.23 Å. If we consider a fully lithiated particle that has just started to

be oxidized, there will be a stress gradient through the particle related to difference in lattice

parameter between the fully lithiated center of the particle and the fully delithiated surface of the

particle. The magnitude of this stress will be highly dependent on the rate at which lithium is

being removed. The higher the current, the larger the stress gradient, implying that for active

materials that are solid solutions during reduction and oxidation, particle fracture is more likely

to occur at higher currents. Fig 2.9b shows the modeled radial stress of a spherical particle of

LMO as a function of C-rate.
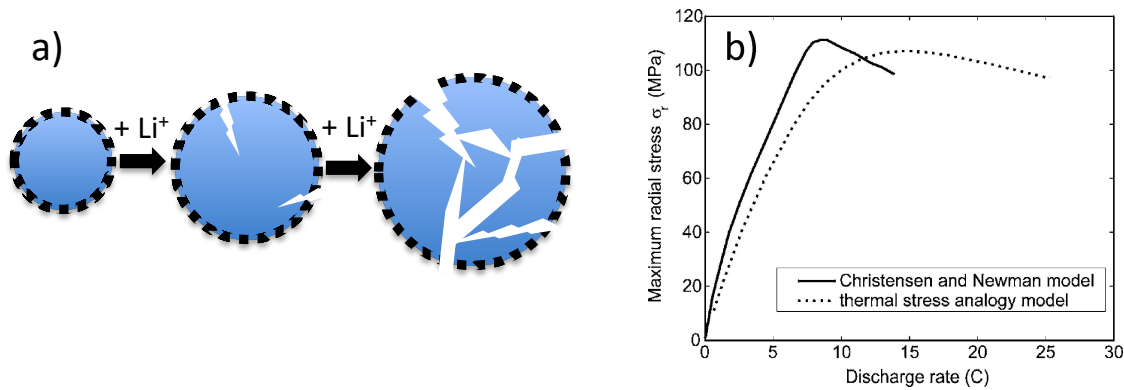
Figure 2.9 (a) A schematic representation of volume expansion of a particle leading to particle fracture and loss of contact with the conductive additive (represented here by black dots). (b) Two different simulations of radial stress in a spherical particle of LMO as a function of discharge rate.[50]

In battery engineering C-rate is used to describe the amount of time it takes to fully discharge/charge a battery, with 1C representing the current needed to discharge the battery in 1 hour, 2C representing the current needed to discharge the battery in half an hour, C/10 represents the current necessary to discharge the battery in 10 hours, et cetera. The other types of intercalation electrodes are those that undergo spinodal decomposition during reduction and oxidation. This means that the total quantity of alkali ions in the structure will only ever have two values. $LiFePO_4$ (LFP), with the phospho-olivine structure, is the most studied of these. During oxidation the material phase separates into $FePO_4$ and $LiFePO_4$ with no phase containing an intermediate amount of lithium (this isn't strictly true, small deviations from 0 and 1 are allowed, for instance $Li_{0.99}FePO_4$ can exist). This means that the induced strain is always close to the difference in lattice parameter between $FePO_4$ and LFP. Because of this, the stress will be mostly independent of the rate at which the material is being cycled.

2.2.2 H_2 and O_2 Evolution

The most obvious difference between aqueous and organic battery chemistries is the difference in stability windows of water when compared to organic solvents. Water has a stability window of 1.23 V, meaning any aqueous cell that operates above this voltage is likely to begin splitting water and generating H_2 and/or O_2 which will pose a serious problem for the long term stability of the cell. However, kinetic limitations related to the activation overpotential may push this window as high as 2 V, though this depends largely on how favorable the available surfaces are for the hydrogen evolution or oxygen evolution reactions. This last point is an important consideration when choosing electrode materials: the ideal cathode material should not act as an oxygen evolution catalyst, and the ideal anode material should not act as a hydrogen evolution

catalyst. Since in this work we are concerned with the failure mechanisms of NTP when used as an anode, we should discuss the nature of hydrogen evolution in a little more detail.

There are three primary reactions pathways that can occur during hydrogen evolution, (1) the Volmer reaction $* +H_2O + e^- \leftrightarrow H^* + OH^-$, in which a proton is reduced and adsorbed onto a surface site (*) and a hydroxide is generated, (2) the Tafel reaction $2H^* \leftrightarrow H_2 + 2*$, in which two adsorbed protons combine to form hydrogen gas and leave two free surface sites, and (3) the Heyrovsky reaction $H^* + H_2O + e^- \leftrightarrow H_2(g) + OH^- + *$, in which a proton is reduced from water at the site of an already adsorbed proton, forming hydrogen gas and a hydroxide[4]. The formation of hydroxide ions and hydrogen gas lead to two primary problems, a large increase in pH within a porous electrode may promote dissolution of the active material if it is unstable at high pH, and entrapment of hydrogen gas within the electrode structure will lead to active material that is excluded from participating in the electrochemical reactions because electrolyte can no longer reach its surface. The latter problem is one that has been well describe when designing electrolyzers, but has not been documented in aqueous alkali ion batteries[51–55]. The general mechanism by which the hydrogen gas is generated and entrapped is as follows. First reduction of protons from water creates adsorbed hydrogen on the surface of the electronic conductor (carbon) within the electrode. When the surface coverage of adsorbed hydrogen is high enough, the Tafel and Heyrovsky reactions will occur, converting the adsorbed hydrogen to hydrogen gas. At low concentration the hydrogen gas remains dissolved within the electrolyte solution. At some critical supersaturation of dissolved hydrogen, it becomes energetically favorable for a bubble to nucleate, after which the bubble will grow primarily by diffusion of solvated hydrogen towards the bubble. The hydrogen bubble will continue to grow until it fills

the pore. After this point, in order for the bubble to continue to grow it must overcome the

capillary pressure of the electrolyte filled pore. This implies that the smaller the pores of the

electrode, the higher the equilibrium pressure of the entrapped hydrogen gas, and as a

consequence they should take up less volume. Nonetheless, the entrapped gas bubble will cause

the pore wall touching the bubble to become electrochemically inactive since ions can no longer

access these regions (see Figure 2.10a). A qualitative representation of this process is given in

Figure 2.10b, showing the concentration of dissolved H_2 as a function of time (this diagram has

been taken from reference [49] and is generally applicable to nucleation and growth processes

involving two phases).
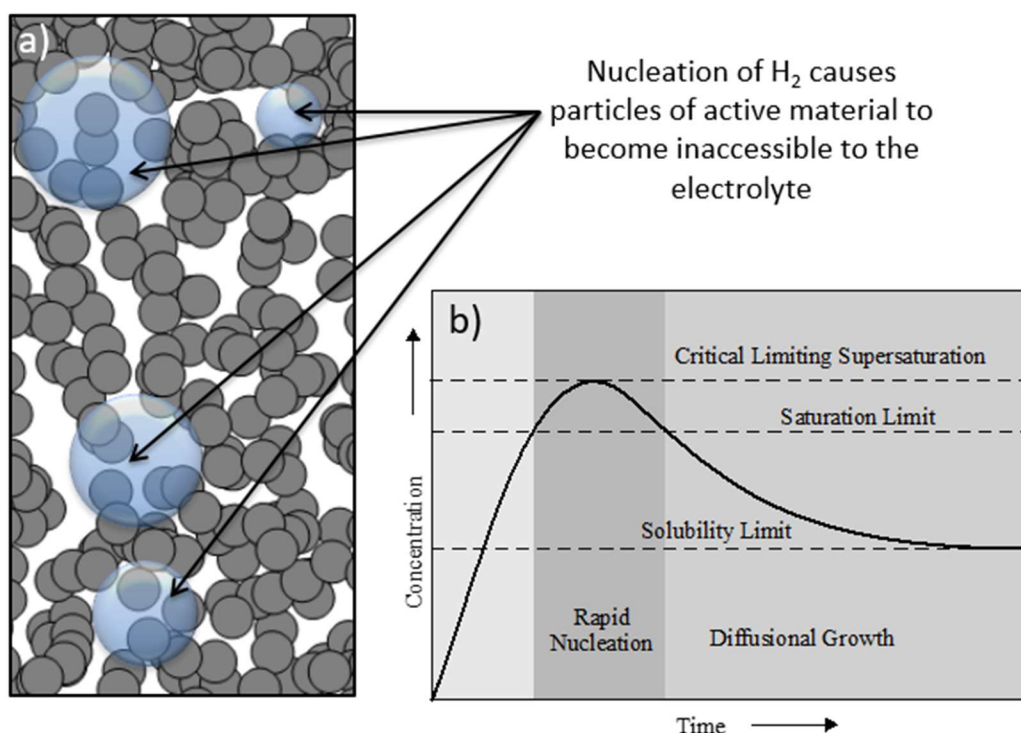
Figure 2.10 (a) Schematic representation of how gas generated within a porous electrode composite will block off electrochemical surface area as well as hinder ion flow through the pore network. (b) Qualitative representation of dissolution, nucleation, and growth of a two phase system.[49]

It should also be noted that once the reaction has stopped the entrapped gas will eventually

redissolve into the electrolyte and diffuse out of the electrode. This occurs because the

equilibrium solubility of gas near the bubble surface will be higher than elsewhere in the electrolyte since the pressure of the bubble will be higher than atmospheric. This leads to a concentration gradient that allows for the hydrogen gas to diffuse out of the electrode structure, though this diffusion will be extremely slow.

2.2.3 Reactions with H₂O ad Dissolved O₂

When choosing active materials for batteries it is important to consider the stability criteria of the electrodes with respect to the electrolyte as well as common contaminants. For instance, it is well known that all useful anode materials for aqueous alkali-ion batteries, when in their fully reduced (charged) state, are thermodynamically unstable in the presence of dissolved oxygen[56]. For a sodium ion intercalation compound the reaction with dissolved oxygen is:

$$Na(intercalated) + \frac{1}{2}O_2(aq) + \frac{1}{2}H_2O \leftrightarrow Na^+ + OH^-$$
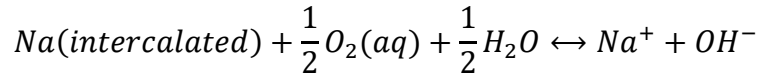
The potential at which this reaction will occur can be calculated from the difference in chemical potential between the two sides of the reaction. In doing this calculation it is found that the potential as a function of pH in an aqueous electrolyte with a concentration of 2 M Na$^+$ is:

$$V = 3.968 - 0.0591pH \quad (V \text{ } vs \text{ } Na/Na^+)$$

This implies that any intercalation material at useful potentials to be an anode in an aqueous alkali-ion battery will react with dissolved oxygen. Luckily, batteries are generally sealed to the atmosphere, and the overall quantity of dissolved oxygen is negligible compared to the total amount of active material such that it will be consumed on the first cycle. However, the active material may also be susceptible to reaction directly with water if its potential is too low[56]. A similar calculation can be carried out as that for dissolved oxygen and the potential at which the material becomes thermodynamically unstable in the presence of water can be found.

$$Na(intercalated) + H_2O \leftrightarrow Na^+ + OH^- + \tfrac{1}{2}H_2(g)$$
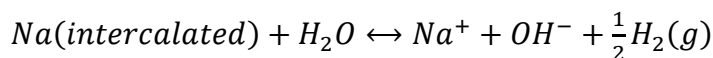
$$V = 2.739 - 0.0591pH \quad (V\ vs\ Na/Na^+)$$

This equation gives us the criteria for what pH electrolyte to use for a given anode material. It should be noted, however, that this is only a thermodynamic consideration and does not account for any kinetic limitations to the reaction with water. This particular reaction could cause an increase in the pH of the electrolyte, promoting dissolution and loss of ECSA due to entrapped hydrogen gas to occur, leading to degradation of the electrode.

2.2.4 Irreversible Side Reactions

Side reactions that lead to deactivation of the active material or consume electrons in such a manner as to lead to eventual cell failure can also occur. The previously discussed hydrogen and oxygen gas generation can be viewed as unfavorable side reactions that are irreversible under most cases. One common irreversible side reaction that is seen in aqueous cathode materials is the irreversible insertion of protons into the structure[16,57,58]. In aqueous alkali ion batteries, energy is stored through the transport and storage of small, monovalent ions. Often times, it is energetically favorable for protons to intercalate in place of Li^+ or Na^+. However, since protons are considerably smaller, they will tend to become associated with a single oxygen of the tunnel or layered structure rather than sitting at a location coordinated by several oxygen. This leads to a relatively high binding energy, which makes it energetically unfavorable for the proton to undergo diffusion and consequently be removed from the structure. The intercalated proton can also interfere with diffusion of the lithium or sodium. Another side reaction that is commonly seen involves a dissolution precipitation reaction. As stated previously Mn^{3+} ions are unstable to a disproportionation reaction that leads to the formation of both Mn^{2+} and Mn^{4+}, where the Mn^{4+}

becomes solid MnO_2 and the Mn^{2+} remains dissolved in solution. Under certain conditions that Mn^{2+} can precipitate out of solution. In particular, upon oxidation of the cathode material some Mn^{2+} can be oxidized back to Mn^{3+} where upon it can react with more Mn^{2+} to precipitate as Mn_3O_4 on the cathode materials surface[59,60]. Mn_3O_4 is electrochemically inert and will lead to deactivation of the cathode surface that it precipitates on. This particular phenomenon has been well documented in rechargeable MnO_2 cells that use lithium hydroxide based electrolytes. There are many more unfavorable side reactions that can occur within aqueous alkali ion batteries, but they are very much dependent on the chemistry, electrolyte pH, and operating conditions of the cell.

2.3 Mitigating Failure

2.3.1 Dissolution

Since dissolution occurs through direct interaction between the electrolyte and active material, an obvious tactic is to prevent the interaction is applying an inert conformal coating. These coatings can take many forms, a more stable ceramic outer shell[61], a conjugated polymer coating[20,62–64], but by far the most common method is application of a carbon coating[39,65–68]. This is generally achieved in one of two ways. The first method is to use carbon based precursors such as metal acetates during the solid state synthesis of ceramic electrode materials. Upon calcination at high temperatures under an inert atmosphere, the carbon containing precursor decomposes, leaving behind a carbon layer on the surface of the ceramic. The second way is to disperse the active material into a solution containing a carbon containing precursor, often carbohydrates or polymers that can be converted to carbon upon heating. This carbon layer acts an electronically conducting coating that helps mitigate degradation related to

the dissolution of active material, slows the evolution of H_2 and O_2 by providing a less catalytically favorable surface for HER and/or OER, and can enhance the fracture toughness of the particles by providing a rigid outer shell capable of handling the high stress related to volume expansion/contraction during cycling. On top of this the carbon coating often lowers the charge transfer resistance be providing an intimate conductor at the surface of the active material.[36]

The process of applying a conformal coating to prevent direct interactions with the electrolyte, aside from increasing the complexity of processing if it is produced in a secondary step, must be well controlled for coating thickness. This is because the coating materials often possess relatively poor ionic conductivity compared to the bulk and as such can drastically increase the concentration polarization if made too thick. It is also necessary to consider whether or not the active material is stable to reduction in the presence of carbon. For instance, high temperature synthesis of certain oxides and phosphates leads to the reduction of the transition metal in the case of oxides or the phosphate to phosphite in the case of the phosphates and the production of CO and CO_2. If the active materials are not thermodynamically stable to reduction by carbon, then a method that does not involve high temperatures should be considered for the production of a carbon coating. It is also important to consider whether or not the surface interactions between the coating and the active material are energetically favorable. If not, the production of a truly conformal coating is unlikely.

Dissolution can also be mitigated through modification of the electrolyte. Aside from the obvious method of controlling the pH such that the active material is essentially insoluble, it is also possible to presaturate the electrolyte with the soluble ion of interest. For instance, if one wants

to work with manganese oxides in neutral or slightly acidic electrolyte, it has been demonstrated that dissolving a certain amount of manganese sulfate into the electrolyte can greatly increase the cycle stability of the manganese based active material[44,69]. This method predicated on the dissolved ion remaining stable in solution. Otherwise it will precipitate out and the active material will begin to dissolve once the concentration drops below some threshold.

2.3.2 Fracture

There are a few ways to avoid particle fracture due to expansion and contraction during cycling. The method that is chosen depends largely on the chemistry involved and what can and cannot be introduced to the system. As mentioned above, application of a rigid outer layer, whether it is carbon or a ceramic can often help increase the fracture toughness enough to avoid particle fracture. Another method for increasing fracture toughness is to decrease the particle size. The fracture toughness of a particle is inversely related to the particle size, so by decreasing the particle size one can increase the critical stress at which fracture occurs. Decreasing the particle size has the added benefit of decreasing the solid state diffusion length as well as increasing the electrochemical surface area. However, if dissolution of the active material is a problem, then increasing the surface area should be avoided. Because of this it is rare to find engineers decreasing the particle size without also applying a carbon coating to the active material.

Aside from just increasing the fracture toughness of the particles, one can avoid high stresses by modifying the lattice in such a way that volume changes are minimized during charging and discharging of the material. This was the case for development of commercially available nickel metal hydride anodes. Anodes used in nickel metal hydride batteries tend to be complex mixtures

of rare earth and transition metals with what is known as an AB_5 structure. The prototypical AB_5 structure is $LaNi_5$, however, commercially available anodes tend to be of the form $MmNi_{3.55-4.3}Co_{0-0.75}Mn_{0.4}Al_{0.3}$ (the actual composition of Co, Mn, Al vary widely). Here Mm represents misch metal, and is used because it is much cheaper than lanthanum. Misch metal contains different amounts of Ce, La, Nd, Pr, Fe, O, C, N, Y, and Ca. The mixture of Mm, Co, Mn, and Al are chosen in such a way as to minimize volume expansion and maximize capacity and cycle stability. A good nickel metal hydride anode may have a volume expansion as low as 6% compared to a poorly chosen mixture having volume expansion >20% [3,4,70]. This alloying method works for nickel metal hydride anodes because the active redox reaction involves the reduction/oxidation of protons within the structure, not oxidation/reduction of the transition metals. For metal oxides, controlling volume expansion is more difficult, but can be controlled to some extent through cation substitution with non-active cations such as aluminum.

2.3.3 H_2 and O_2 evolution

Because the electrochemical stability window of water is 1.23 V, evolution of hydrogen and oxygen gas are mostly unavoidable for cells that operate above this voltage. However, certain methods can be used to minimize the rate of the HER and OER through increasing the activation overpotential for these reactions. As stated earlier carbon surfaces are not particularly catalytically active for hydrogen evolution, so coating the active material with carbon is a good first step to slowing down the HER. There are also certain chemicals that can be added to a system that will strongly adsorb to the electrode surfaces and prevent the adsorption step of the Volmer reaction. This particular method has been investigated for metal electrodes in aqueous metal air batteries through incorporation of alkanethiols, which are known to form strongly

adhering self-assembled monolayers (SAM) on metal surfaces. By choosing an alkanethiol of appropriate length Malkhandi et al. were able to decrease the rate of HER by two orders of magnitude without hindering the intended electrode reaction[71]. This approach, however, relies on use of a metal surface and is not a reasonable solution if hydrogen adsorption is a necessary step of the electrochemical process, such as in Ni-MH chemistries. Instead NiMH cells are designed in such a manner as to promote equal amounts of H_2 and O_2 generation, and the system is kept in an electrolyte starved condition to promote gas diffusion through the electrode structures[3]. This allows for hydrogen and oxygen recombination within the cell. Although this method does decrease the Coulombic efficiency of the cell since some quantity of electrons are lost to gas generation, it prevents potential drift of a single electrode allowing for a relatively stable cycling capacity.

2.3.4 Reactions with H_2O and Dissolved O_2

Unlike dissolution, these reactions cannot be fully prevented using a conformal coating. This is because the mechanism of these reactions relies on exchange of the alkali ion out of the reduced anode material at low potentials, coupled with an electron exchange between the redox active ion of the system and either the oxygen or water. As long as the active material is in both ionic and electronic contact with the electrolyte, this reaction can occur. And since ionic and electronic contact are necessary for the normal operation of the cell, they should not be prevented.

The reaction with dissolved oxygen can be prevented by ensuring that there is no dissolved oxygen within the electrolyte or that the cell being tested is well sealed prior to use, such that any dissolved oxygen is consumed during the first few cycles. The former can be achieved through

addition of an oxygen scavenger such as sodium sulfite, or through bubbling nitrogen through the electrolyte for an extended period of time. However, given the relatively low amount of electrolyte present in sealed cells and the low solubility of oxygen, the latter solution is generally more practical.

As for the reaction with H_2O, the most common method of prevention in increasing the pH of the electrolyte in order to lower the potential threshold for the HER reaction [40,56]. This is only feasible, however, if both the anode and cathode materials in the system are stable under those pH conditions.

2.3.5 Irreversible Side Reactions

Since irreversible side reactions tend to be highly dependent on chemistry it is difficult to assign any mitigation technique as general. An example, however, is the irreversible precipitation of Mn_3O_4 in rechargeable Zn/MnO_2 cells that use a LiOH based electrolytes. As stated previously the reaction that causes the precipitation of Mn_3O_4 is related to the dissolution on manganese when the system is reduced, followed by the partial electrochemical oxidation of solvated manganese at the surface of the particles. One method that addresses the electrochemical oxidation and precipitation process but not the dissolution process in this system is the addition of solvated bismuth to the electrolyte. Bismuth ions are believed to form stable surface complexes with the MnO_2 surface that prevent the local precipitation of Mn_3O_4[60,72]. Cells that utilized this method showed a slower rate of capacity fade since they only lost capacity due to dissolution of manganese rather than losing material to dissolution and inactivation of the surface due to precipitation of electrochemically inert Mn_3O_4.

2.4 Sodium Titanium Phosphate as an Aqueous Anode

Se we may now ask, which of these degradation mechanisms are at play during the cycling of NTP? One of the properties of NTP that make it attractive for aqueous sodium ion batteries is its relatively low redox potential, -0.6 V vs. SHE. Also, since NTP undergoes spinodal decomposition into sodium rich and sodium deficient phase, its voltage profile is quite flat, which is particularly favorable for design of battery management systems. The low potential allows for a comparatively high potential cell, 1.7 V when paired with a cathode such as LMO with a potential of about +1.1 V vs. SHE. However, this potential is below the hydrogen evolution potential when the cell is in neutral pH electrolyte. This means that not only will hydrogen be evolved directly from water at the surface of the conductive additive, but that the electrode material its self will be oxidized from its fully reduced state in the presence of water. This reaction is essentially a method of self-discharge, where electrons put into the system can no longer be removed, leading to lower round trip efficiencies.

$$Na_3Ti_2(PO_4)_3 + 2H_2O \leftrightarrow NaTi_2(PO_4)_3 + 2Na^+ + 2OH^- + H_2(g)$$
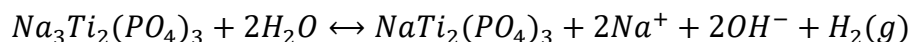
From thermodynamics, assuming 1 M Na_2SO_4 electrolyte, the potential at which this reaction will occur will be:

$$V = 0.029 - 0.059pH \quad (V \ vs \ SHE)$$

If we ignore kinetic factors and assume that we'd like the anode of the system to have a cut off voltage of -0.65 V vs. SHE, then the electrolyte will need to have a pH of 11.4 or higher to avoid this reaction. Along with this self-discharge reaction, we expect the direct electrochemical evolution of hydrogen at low potentials. Assuming ideal solutions, this reaction will have a potential of:

$$V = -0.059pH \quad (V\ vs\ SHE)$$

Assuming the same cut-off potential of -0.65V vs. SHE, then electrolyte with a pH of 10.9 or greater would be needed to avoid the electrochemical evolution of hydrogen gas. Given that NTP tends to be cycled in neutral pH electrolytes, we'd expect water decomposition within the porous electrode to eventually lead to an increase in pH with in the electrolyte. Several authors report that poor performance of NTP at high pH is probably due to dissolution of the material, though none have confirmed or directly studied the dissolution.

 Also associated with these hydrogen-evolving reactions, is the loss of ECSA due to gas entrapment within the pores. The actual relationship between loss of ECSA due to gas entrapment and loss of capacity will depend strongly on the pore size distribution and pore geometry. There is also the possibility for unfavorable side reactions to occur due to the formation of OH-. For instance, the conductive additive of choice for researchers is carbon black, which under most conditions is considered highly stable, but can be corroded under certain extreme conditions. For instance, in highly alkaline (pH = 14) electrolyte solutions, carbon can be electrochemically oxidized to carbonate [73].

$$C + 6OH^- \leftrightarrow CO_3^{2-} + 3H_2O + 4e^-$$
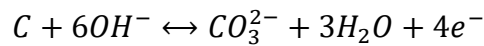
The alkaline oxidation of carbon will occur at potentials greater than -0.7 V vs. SHE, which under normal operating conditions, aqueous electrodes are always above. The main reason this isn't generally considered a problem is because of the mild electrolyte conditions normally used and the extremely slow kinetics of this reaction due to it being a four-electron process. However, since we may be generating high concentrations of OH- within confined pores, this possibility should not be ignored.

NTP has a $R\bar{3}c$ crystal structure with hexagonal lattice parameters of a = 8.617 Å, c = 22.02 Å and a unit cell volume of 1416.251 Å^3. Upon reduction, NTP takes up two sodium per formula unit and from neutron diffraction studies it is known that the structure distorts to a $P\bar{1}$ type structure [74]. However, XRD of the fully sodiated material can be interpreted as being close to $R\bar{3}c$ structure to facilitate direct comparisons with the unsodiated structure. If this is done, then the volume expansion ΔV/V is equal to 10%. Since NTP undergoes spinodal decomposition it is safe to assume there is a moving boundary between the sodium rich and sodium deficient phases, with a linear strain of ~3% for low index interfaces. This strain should be mostly independent of the C-rate at which the NTP is being operated. If this strain is enough to cause particle fracture, it should be visible after cycling using scanning electron microscopy (SEM).

Chapter 3: Materials and Methods

3.1 Overview

In order to enhance the performance of NTP based electrodes, it is necessary to determine the extent to which each of the aforementioned degradation mechanisms occurs within aqueous NTP anodes. In understanding how loss of capacity occurs, we should be able to propose engineering solutions that directly address the primary failure mechanisms. To that ends, we first characterized the inherent chemical stability of NTP in high pH electrolytes. After characterizing the inherent chemical stability, we carried out in situ pH measurements of NTP electrodes during electrochemical cycling, so that we could map the measured pH changes to the observed instability in high pH electrolyte. After this we tested a specific form of polymeric coating to help prevent the observed capacity fade. Next, based on observations from previous experiments, we characterized the effect of gas generation on the measured ECSA and mapped this to the apparent loss in capacity upon cycling at low rates. Lastly, we propose a method for overcoming loss of ECSA to gas entrapment through incorporation of activated carbon.

Throughout these experiments a number of techniques were used. Morphology and structure were characterized using scanning electron microscopy, transmission electron microscopy, x-ray powder diffraction, and Fourier transform infrared spectroscopy. Elemental analysis to determine loss of titanium and phosphorous from NTP were done using inductively couple plasma mass spectrometry and energy dispersive x-ray spectroscopy. A number of electrochemical techniques were used to characterize the performance of NTP including cyclic voltammetry, galvanostatic cycling with potential limitation, staircase potentiostatic titration, open circuit potential measurements, and electrochemical impedance spectroscopy. In the section that follows a brief

description will be given of each of these techniques in order to facilitate the readers understanding of the experiments that have been carried out. A short description of the synthesis methods used to produce the NTP used in these experiments will also be given in the section to follow.

3.2 Synthesis of NaTi$_2$(PO$_4$)$_3$

There are three ways in which NaTi$_2$(PO$_4$)$_3$ was synthesized in the experiments carried out, (1) solid state synthesis, (2) hydrothermal synthesis, and (3) solvothermal synthesis. The solid state synthesis of NTP has been report in numerous papers and involves mixing stoichiometric amounts of TiO$_2$ (either rutile or anatase), a sodium salt (NaH$_2$PO$_4$ or a salt containing an anion that decomposes during synthesis such as carbonate or acetate), and a source of phosphate, usually ammonium phosphate or phosphoric acid. In order to improve electrochemical performance and limit the growth of particles, carbon in the form of carbon black or graphite is often added to the precursor mixture. Once thoroughly mixed, the precursor is placed in a furnace (under inert gas if carbon black or graphite have been added) and fire between 700-1000 °C for anywhere between 1 and 12 hours. Although this method is relatively simple and scales well, it is difficult to obtain phase pure materials. TiP$_2$O$_7$ and amorphous sodium phosphates and phosphites are the primary impurity phases and are difficult to avoid due to thermodynamic considerations and phase stability.

Hydrothermal synthesis is the production of materials (normally ceramics) within an aqueous solution at elevated temperatures and pressures. Figure 2.10b shows the process of crystal growth in hydrothermal solutions as the concentration of materials in solution as a function of

time. As the concentration of dissolve species changes with increasing temperature and time, so too does the phase stability of the system. Eventually a point is reached where the dissolved species are no longer thermodynamically stable and a crystal will nucleate and grow. The nucleation and growth mechanism is analogous to how hydrogen gas bubbles nucleate in solution.

The hydrothermal synthesis of NTP offers the advantage of being able to produce well faceted, phase pure, and uniformly sized cubes. This can be achieved through mixing of equal parts TiO_2, NaH_2PO_4, H_3PO_4 (85 wt% aqueous solution), and deionized water in a mortar and pestle, then transferring the resulting paste into a PTFE lined autoclave. In order to obtain phase pure and uniformly sized cubes, it has been found that an oven temperature of 150 °C is optimal. It is also necessary to use nanoparticulate anatase as the TiO_2 source since the synthesis process relies on the dissolution of titanium in the form of $Ti(OH)_2^{2+}$ and the equilibrium solubility of a particle is inversely related to the particle size. Anatase is also more soluble than rutile. The highly uniform, well faceted crystals are ideal for being able to observe morphological changes in the system during reactions of the material in high pH solutions, and since the crystals are produced in solution, soluble byproducts (such as sodium phosphates and phosphites produced during solid state synthesis) are not a concern. However, given the particularly large particle size, ~ 500 nm on average, electrochemical testing must be done at low currents (scan rates) in order to minimized the overpotentials of the system. Hydrothermal synthesis also has the added step of rinsing the produced material several times. In our experiments this was accomplished by dispersing the mixture in deionized water, centrifuging at 4000 rpm, decanting, and repeating the process until the decanted liquid had a neutral pH.

Solvothermal synthesis is analogous to hydrothermal synthesis except in place of water a solvent, or mixture of solvents is used. In our experiments, we have synthesized NTP with a particle size of ~ 90 nm using a mixture of 20 mL butanol, 5 mL H_3PO_4 (85wt% aqueous), 5 mL deionized water, 5 g of NaH_2PO_4, and 3 g of titanium isopropoxide. The procedure for producing the solvothermal solution was (1) dissolve titanium isopropoxide in butanol and place into the PTFE autoclave liner, (2) dissolve the sodium salt into the mixture of phosphoric acid and water, (3) under vigorous stirring add the acid salt solution drop wise to the butanol solution, (4) after the solutions are completely mixed, seal the autoclave and place in the oven at 150 °C overnight, (4) disperse the product in deionized water or ethanol, centrifuge, and decant until the solution measures a neutral pH. Upon addition of the acid solution to the butanol solution, titanium isopropoxide quickly began to undergo hydrolysis forming a milky white solution. It was also observed that the reaction mixture bubbled, possibly from the dehydration of butanol by phosphoric acid, and the final product phase separated into aqueous and organic phases (the produced NTP was in the aqueous phase which was denser than the organic phase, and so separated to the bottom of the container). Figure 3.1 shows the XRD pattern from the solvothermally produced NTP used in this work, and shows the material to have a high phase purity.
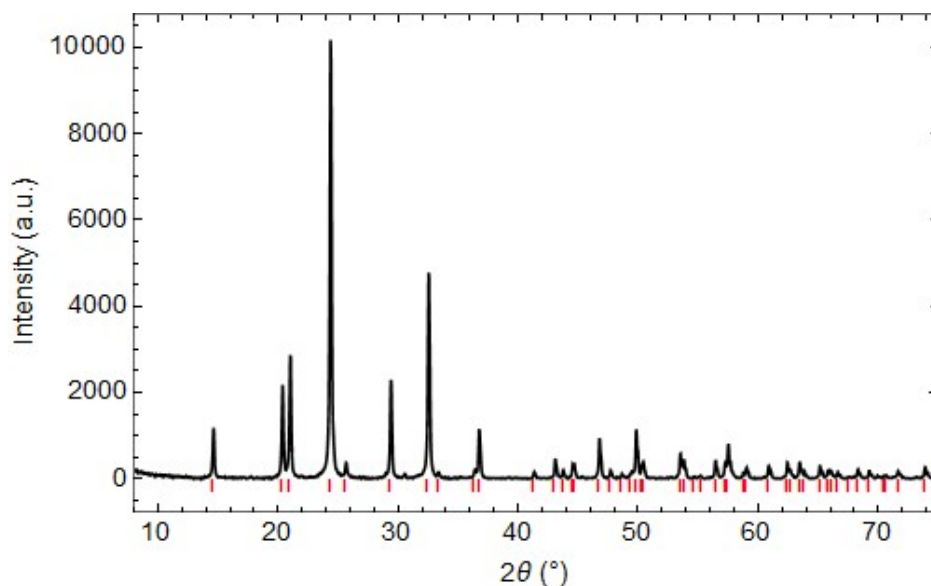
Figure 3.1 X-ray diffraction pattern for solvothermally produced NTP, with the expected peak positions from JCPDS 88-2265 shown as red has marks.

3.3 Morphological, Elemental, and Structural Characterization

3.3.1 Powder X-ray Diffraction (XRD)

Powder X-ray diffraction (XRD) is a powerful technique for characterizing the crystal structure of materials and is ubiquitous in the field of material science. In XRD a sample is exposed to a beam of X-rays of known wavelength, with the incident angle of the X-ray beam changing with time, while a detector measure the intensity of X-rays leaving the sample. This technique relies on the fact that crystals are well ordered with fixed plane spacing. When the incident x-ray beam is at certain angles, the path length the X-ray takes between adjacent crystal planes, with a spacing d, will be an integer value of the wavelength of the X-ray. This will lead to constructive interference and a spike in intensity will be measured at the detector. The relationship between the plane spacing d, the wavelength λ, and the angle θ is defined by Bragg's law.

$$n\lambda = 2d \sin \theta$$

Where n is the wavenumber, and except for a few special cases is normally taken to be equal to 1. Since the plane spacings, *d,* are set by the crystal structure of the material and the wavelength λ is set by the x-ray source, one can see that only specific values of θ, will satisfy the equation. At all other angles, the X-rays will destructively interfere and no change of intensity above background will be measured at the detector.

By using the angles measured from XRD, it is possible to calculate the value of the d-spacings, and with information about the crystal symmetries the calculated d-spacings can be used to determine the lattice parameter of the crystal structure. XRD is an extremely sensitive technique and, depending on the operating parameters, can calculate changes in lattice parameter on the order of picometers.

3.3.2 Scanning Electron Microscopy (SEM)

Electron microscopy is the method of choice for imagining of materials at small scale. Scanning electron microscopy works by scanning a focused beam of high-energy (5-30kV) electrons across a sample and collecting the outgoing signal with one of a few different types of detectors. There are two modes of imaging for SEM that rely on the two different types of electrons that can be collected, secondary electrons and back scattered electrons. Secondary electrons are electrons that are emitted from atoms of the sample after being excited by the incident electron beam. The emission of secondary electrons is an inelastic scattering process, so the emitted electrons will be of lower energy than the incident beam. An Everhart-Thornley detector is used to collect these electrons, and relies on positively charge faraday cage around the entrance of the detector to attract the emitted electrons. The magnitude of the voltage applied to the faraday cage is chosen such that it is too weak to influence the high energy beam and back scattered electrons,

but strong enough to attract the lower energy secondary electrons. Back scattered electrons are electrons from the incident beam that elastically scatter off of the specimen. Because of the high energy of these electrons, they must be collected from a detector at the end of the electron column, located directly over the specimen. Since the amount of electrons that will be elastically scattered depends on the atomic number of the elements in a specimen, back scattered imaging can be used to distinguish variations in elemental composition with higher Z materials appearing brighter.

SEM may also be used to carry out what is known as energy dispersive x-ray spectroscopy (EDX), a type of elemental analysis. EDX relies on the characteristic energy of x-rays emitted from electron transitions between different orbitals of an atom. When an electron is excited from a low energy orbital to a higher energy orbital by the incident beam, it leaves behind an electron hole. Since this hole is energetically unfavorable, another electron will drop into the lower energy orbital, emitting an x-ray that is of equal energy to difference in energy of the two orbitals. This energy will be characteristic of a specific element and transition and so by measuring the energies of X-rays being emitted, it is possible to obtain the elemental composition of a sample (because of the type of detector used it is not possible to measure H, He, or Li, within a sample).

3.3.3 Transmission Electron Microscopy (TEM)

TEM is similar in nature to SEM in that it relies on the small wavelength of high-energy electrons in order to image fine details in a sample. However, rather than collecting secondary or backscattered electrons, TEM relies on electrons that pass through the sample interacting with a

phosphor screen below the sample. Since TEM relies on electrons passing through a sample, the electron beam must be of much higher energy than SEM, with standard beam energies being anywhere from 200 keV to 400 keV. Because of this TEM systems have subnanometer resolution. One advantage of TEM over SEM is the ability to single crystal diffraction patterns from the diffracted electron beam. This allows for characterization of crystal structure (though the accuracy is much lower than XRD) of single crystals, and so can be used to determine surface faceting of single particles of a material.

3.3.4 Fourier Transform Infrared Spectroscopy (FT-IR)

FT-IR is a technique used to gain information about the local bonding structures of a material. It relies on the fact that different bonding coordination of atoms within a structure will possess different vibrational modes that may be of similar frequency to infrared light (with wave numbers between 4000 cm^{-1} and 600 cm^{-1}). In FT-IR a sample is illuminated with infrared light of varying wavelengths and the amount of light that is reflected or transmitted is then measured. If the vibrational modes of the material being tested are of a frequency within the IR range and are active modes, than upon illumination with the corresponding frequency, the light will be absorbed. This will lead to a decrease in the intensity of light measured at the detector. The particular pattern obtained can then be compared to databases of known materials and vibrational modes and changes in the bonding of the material can be determined. This is particularly useful for determining changes related to amorphous materials that may not be measurable by XRD.

3.3.5 Inductively Coupled Plasma Mass Spectrometry (ICP-MS)

When measurements of extremely low concentrations of elements are needed, ICP-MS is the technique of choice for most researchers. It allows for measuring concentrations as low as 1 part per trillion, and can be used to differentiate between different isotopic compositions of elements. The technique involves completely dissolving a sample (generally in nitric acid) in solution, atomizing the solvated sample as an aerosol that is carried into an argon plasma, within the plasma the atoms become ionized and are carried through a series of cones, to a quadrupole detector, where they are separated by their mass-to-charge ratio. The detector will give a signal that is directly proportional to the concentration of the ion of interest, but in order to obtain quantitative results, solutions of known concentration prepared from certified standards must be tested to establish a calibration curve.

3.4 Electrochemical Techniques

3.4.1 Cyclic Voltammetry (CV)

Cyclic voltammetry is perhaps the most common technique for electrochemical characterization of materials. In CV the potential of a sample is varied at a constant rate between two vertex potentials, and the current necessary to maintain this rate is measured. The setup for a CV involves a three electrode set up, the working electrode is the electrode material being studied, the counter electrode acts as a source or sink for the electrons being consumed by or removed from the working electrode, and the reference electrode is an electrochemical couple of known potential that is in ionic contact with the electrolyte solution containing the working electrode (Figure 3.2a). The reference electrode is vital in being able to compare the redox potential of the working electrode to other materials. Plenty of information can be obtained from CV; the area

under the current curve with respect to time gives the capacity of the sample, running samples at different scan rates allows the rate capability of different redox processes involved to be determined. Along with being used to determine capacity and rate capability, CV can give information on the stability window of a material, redox potentials, diffusion rates, and can be used to characterize hysteresis between the charge and discharge processes.
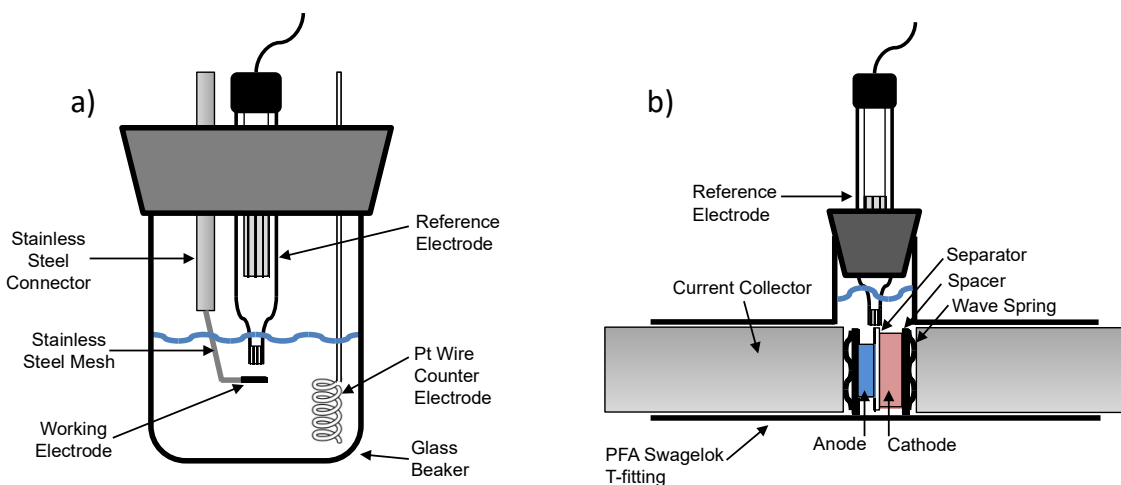
Figure 3.2 (a) The cyclic voltammetry half-cell set up used in most experiments within this work. (b) A three-electrode Swagelok type set up used for GCPL measurements in this work.

For all half-cell type configurations in this work, where a platinum wire counter electrode was used, the working electrode consisted of the electrode composite material pressed into a piece of stainless steel mesh (Figure 3.3).
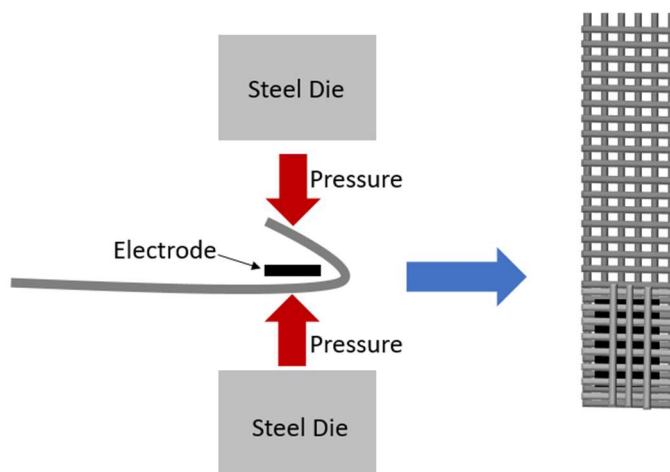
Figure 3.3 Sample preparation of electrodes used within the half-cell set up shown in figure 3.1a.

3.4.2 Galvanostatic Cycling with Potential Limitation (GCPL)

Galvanostatic cycling is the most common technique for evaluating the cycling performance of battery systems. In galvanostatic cycling a constant current is applied to the electrochemical cell until a potential limit is reached by the system, after which the current is reversed until the second potential limit is reached (note that galvanostatic cycling simply implies constant current, and so limits other than potential can be used as a trigger to switch current i.e. capacity limitation). Since the voltage of a battery changes during a single charge or discharge, current-voltage curves are not applicable as a measure of performance for a battery. Instead power density vs. energy density plots, known as Ragone plots (Figure 3.4), are produced by performing GCPL at different currents.
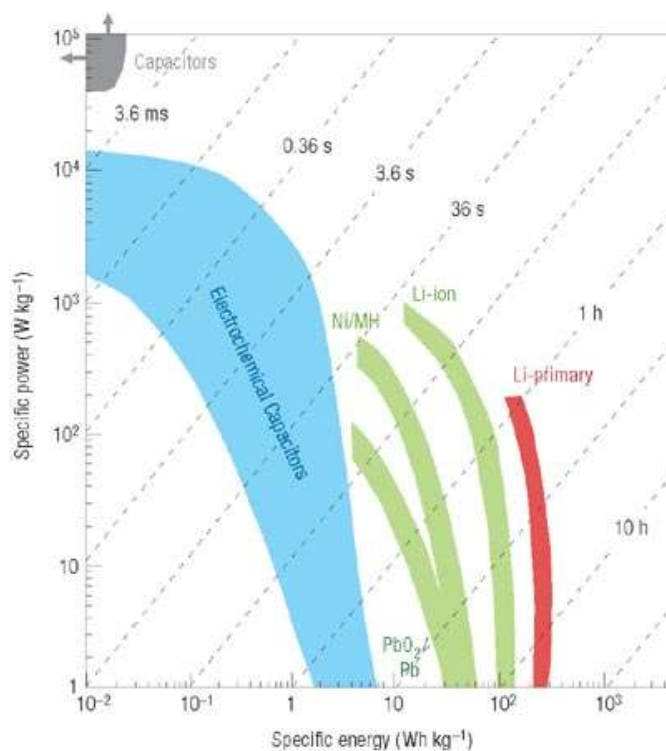
Figure 3.4 Ragone plot showing the relationship between power density and energy density for several forms of energy storage.[75]

Depending on the materials and mass ratios used, GCPL cells can be made to test either a single material of interest or specific full cell chemistry. In order to test a single material, it is usually favorable to use a three-electrode T-cell configuration (Figure 3.2b) with a counter electrode that is stable and at least an order of magnitude higher in capacity. This helps ensure that changes in performance are less likely to occur due to the instability of the counter electrode. For testing specific full cell chemistries, it is important to know beforehand what the stable voltage range and specific capacity of the electrode materials are so that proper mass ratios and potential limits can be set. Normally the anode and cathode are balance in capacity to maximize the energy density of the cell.

3.4.3 Electrochemical Impedance Spectroscopy (EIS)

Electrochemical impedance spectroscopy (EIS) is a powerful technique for investigating the many different transport properties of electrochemical systems. Analysis of the collected data can yield important information about the transport properties, nature of interfaces involved, and insights into the chemical reactions taking place at an electrode. In general, EIS consists of applying a sinusoidal, low amplitude, voltage (or current) with varying frequency (from hundreds of kilohertz to millihertz) and measuring the resulting current (or voltage). By measuring the resulting phase shift of the response current, it is possible to determine, for any given frequency, the impedance of the system. However, the technique is sensitive to set up and reliable interpretation of the collected data is dependent on some actual knowledge of the system being investigated and should always be considered in conjunction with other techniques.

Chapter 4: Inherent Chemical Stability of NTP in High pH Solutions

4.1 Overview

The first aspect of NTP that we'd like to understand, in order to quantify its degradation mechanisms, is its inherent chemical stability within high pH electrolytes. We know that under normal operating conditions porous NTP electrodes should become basic due to the generation of hydroxide during HER. Researchers have also indicated that in order to prevent HER using an electrolyte with pH > 11 is necessary. Although some groups have proposed that high pH is responsible for the capacity degradation they see, none have quantified or characterized the extent to which NTP is degraded at high pH.

Work has been done to understand the inherent chemical stability and degradation of materials similar to NTP such as $Li_{1+x+y}Al_xTi_{2-x}Si_yP_{3-y}O_{12}$ and $Na_3Zr_2Si_2PO_{12}$ because of their potential use as solid electrolytes in batteries or electrochemical sensors. For these materials, phase segregation of amorphous impurity phases formed during solid-state synthesis, dissolution at high pH, and direct reaction with H_2O have been concluded to be the primary failure mechanisms[76–79].

4.2 Experimental

4.2.1 Preparation of NaTi$_2$(PO$_4$)$_3$ cubes

To provide a consistent and well-defined platform for these studies, we synthesized and used NTP with uniform dimensions and interfacial qualities. Specifically, pristine faceted $NaTi_2(PO_4)_3$ cubes were prepared via a hydrothermal method following the procedure of Yang et

al. [80]. Briefly, 2 g of NaH_2PO_4, 2 g of TiO_2 (21nm Sigma Aldrich), 2 mL of H_3PO_4 (85 wt%

aqueous solution), and 2 mL of deionized water were mixed into a viscous paste inside of an

agate mortar and pestle. This paste was transferred into a 100 mL PTFE lined autoclave (Parr

Instruments Company), transferred into an oven with the temperature set to 150 °C, and left over

night. The resulting material was centrifuged, decanted, and rinsed with deionized water five

times. The resulting powder was dried in an oven at 120 °C overnight and then fired in an

ambient air furnace at 550 °C for 6 hours.

4.2.2 Preparation of Solutions

All concentrations of the prepared solutions are reported on the molal scale and all containers

used were made of polypropylene to avoid possible contaminations from using glass. All

samples were prepared using 18.2 MΩ deionized water from a Barnstead NANOpure. For the

solubility measurements buffer solutions at pH 9.5, 10.5, and 11.0 were created by adding an

appropriate volume of 0.1 m NaOH to fixed volumes of 0.01 m $B(OH)_3$ while actively

measuring the pH using an Electro Analytical Instruments 12-Channel MCC System with a

Microelectrodes Inc. MI-4144 pH probe. For the solutions at pH 12.2, 12.7 and 13.8 an

appropriate amount of 5 m NaOH was added to a background electrolyte of 0.1 m $NaNO_3$. To

these solutions approximately 300 mg of NTP cubes were added to 10 mL of the buffer solution

inside of a 15 mL centrifuge tube. These were mixed and ultra-sonicated for 15 minutes, three

times daily, to prevent excess agglomeration of particles at the bottom of the centrifuge tubes.

After one week of soaking the samples were centrifuged to force the sedimentation of solids and

a 2 mL aliquot was taken and added to 5 wt% HNO_3 for later measurement.

4.2.3 Materials Characterization

Inductively coupled plasma mass spectrometry (ICP-MS) was used to quantify the equilibrium concentration of titanium ions in the buffer solutions using an Agilent 7700x ICP-MS with He-mode octopole reaction cell. Calibration of the ICP-MS was carried out by preparing standards of 0, 1, 5, 10, 50, 100, 500, 1000 ppb titanium in the same 5 wt% HNO_3 solution used to dilute the aliquots. After calibration the system had a detection limit for titanium of 2.21 ppb with a measured background equivalent concentration of 1.43 ppb.

In order to characterize the morphological changes of the NTP cubes scanning electron microscopy (SEM) was carried out on a Philips XL-30 scanning electron microscope and tunneling electron microscopy (TEM) was carried out on a JEOL-2000EX. Selected area electron diffraction (SAED) was also performed on the TEM. Crystal structures of the samples were determined by X-ray powder diffraction (XRD) using a PANalytical X'Pert Pro MPD with a CuK_α source and a nickel filter. A scan range of 10-75 °2θ was used for all samples. Care was taken to ensure dense packing of powders with in the sample slide. In order to observe changes in bonding as well as monitor for the presence of structural water, Fourier transform infrared spectroscopy (FT-IR) was performed using a Perkin Elmer Frontier FT-IR in the range of 3500-600 cm^{-1} at a resolution of 1 cm^{-1}.

The electrochemical performance of the NTP cubes was tested by cyclic voltammetry (CV) and galvanostatic cycling with potential limitation (GCPL) using a Bio-Logic VMP3. Electrode materials were prepared by combining 70 wt% of the NTP powder with 20 wt% carbon black (Timcal Super P) and 10 wt% polyvinylidene fluoride (PVDF, Sigma Aldrich) in a mortar and pestle. Once a homogenous powder was obtained, a few drops of n-methylpyrrolidone (NMP) were added and the mixture was mixed into a thick, smooth paste. This paste was transferred into

a vacuum oven and dried under vacuum at 70 °C overnight before being granulated through a 80x80 mesh screen. Approximately 4 mg of powder was pressed into a 50x50 mesh stainless steel screen at 3 tonnes on a Carver Model C Laboratory press. The electrode area was approximately 0.25 cm^2 after pressing and the thickness was 500±75 μm. Based on bulk densities and electrode volumes, the porosity of these electrodes was 20-30 vol%. These electrodes were used for both CV and GCPL. All CV experiments were carried out at a scan rate of 0.100 mV/s from -0.5 to -1.5 V versus mercury sulfate electrode (MSE) in saturated K$_2$SO$_4$ (+0.654 V vs. SHE), in 1 M Na$_2$SO$_4$ solution using a platinum wire counter electrode and. Unless otherwise noted all potentials will be reported versus the MSE reference electrode. GCPL experiments were performed in 1M Na$_2$SO$_4$ at neutral pH in glass W-cells with porous glass frits separating each compartment, an MSE reference electrode, and a platinum wire counter electrode. The NTP electrodes cycled between -1.5 and -0.5 V at a C/3 rate.

4.3 Results and Discussion

4.3.1 Solubility of NTP by ICP-MS

The equilibrium solubility of NTP at 25 °C as measured by dissolved titanium can be found in Fig. 4.1. It was found that in aqueous solutions below a pH of about 11, the solubility of the NTP was quite low, with the concentration of dissolved titanium hovering around 10 ppb. This value is in good agreement with previously reported values for the solubility of titanium from TiO$_2$, which are also roughly 10 ppb, and have been attributed to formation of aqueous Ti(OH)$_4$[81]. At pHs > 11, Ti(OH)$_5^-$ becomes more stable than Ti(OH)$_4$ and the total solvated titanium increases. At the highest pH tested, pH = 13.8, the concentration of dissolved titanium is lower than expected. This is most likely due to the precipitation of another phase at high pH. Indeed,

SEM images of the samples prepared at pH =13.8, Fig. 4.2d, confirmed the presence of a long, needle like secondary phase. The authors would like to note that they have only presented solubility data for samples produced at 25 °C for two reasons, (1) it is not guaranteed that the concentration measured at 25 °C would be indicative of the actual concentration of samples produced at 70 °C, since upon cooling of the solution, Ti may precipitate out of the solution and (2) given the large amount of secondary precipitates that were observed in SEM it was clear the dissolved Ti was thermodynamically unstable in solution with respect to other phases so that the measured concentration would not be indicative of the actual solubility of NTP. It should also be noted that although the solubility measurements gave a good estimation of the equilibrium solubility of the titanium in solution, they did not account for particle size effects on the rate of dissolution or the thermodynamic stability of NTP in high pH solutions.
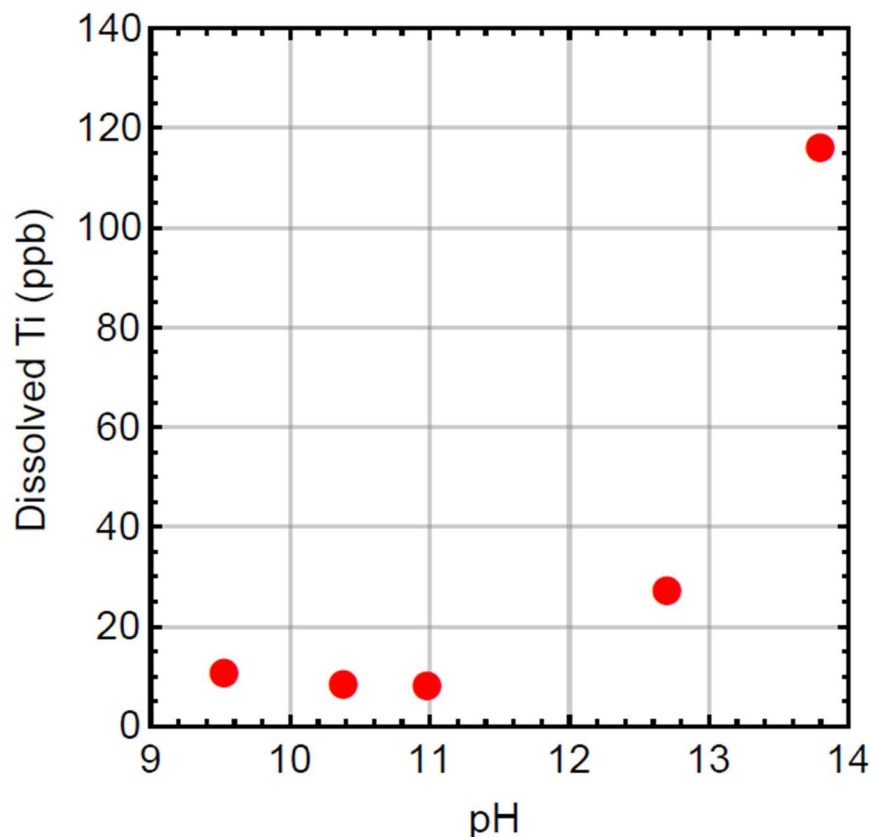
Figure 4.1 Total dissolved titanium from NaTi$_2$(PO$_4$)$_3$ in alkaline aqueous solutions at 25 °C.

4.3.2 Morphological and structural changes

SEM analysis was used to qualitatively observe the surface degradation of the NTP cubes due to dissolution, and was applied to the samples soaked in 0.1 m NaNO$_3$ and solutions of NaOH at pH > 12 at both 25 °C (Fig. 4.2) and 70 °C (Fig. 4.3) for 1 week. For the samples prepared in 0.1 m NaNO$_3$ at both temperatures, there appears to be almost no evidence of surface degradation, though the sample prepared at 70 °C appears to have small pits on the surface of a few particles (Fig. 4.3a). These samples also show rounded corners and some fracturing. The samples prepared from solution at pH = 12.2 and pH = 12.7 at 25 °C show a noticeable amount of surface pitting, with the one at higher pH showing a larger quantity of pitting, as well as having larger pits. A significant fraction of the pits in the sample prepared at pH = 12.7 show a square

58

morphology indicating that there is a preferential corrosion. For the sample prepared at pH =

13.8 and 25 °C (Fig. 4.2d), the degradation is severe, with the majority of particles showing large

surface pits. There is also a significant amount of a secondary phase that has precipitated onto

the surface of the particles, indicating that at high enough concentration of OH⁻ another solid

phase becomes thermodynamically stable and will continually absorb dissolved titanium,

allowing for the continued dissolution of the NTP particles. Given the anisotropic, wire-like

morphology of this secondary phase, and the high pH aqueous formation conditions, it is likely

some form of layered $Na_xH_{2-x}Ti_nO_{2n+1} \cdot yH_2O$[82]. TEM of the secondary precipitate can be

found in Fig. 4.4. Selected area diffraction of the wires (Fig. 4.4b-d) shows two broad amorphous

diffraction peaks as well as two sharper crystalline peaks. However, it was not possible to index

the measured diffraction peaks to a known crystal structure.
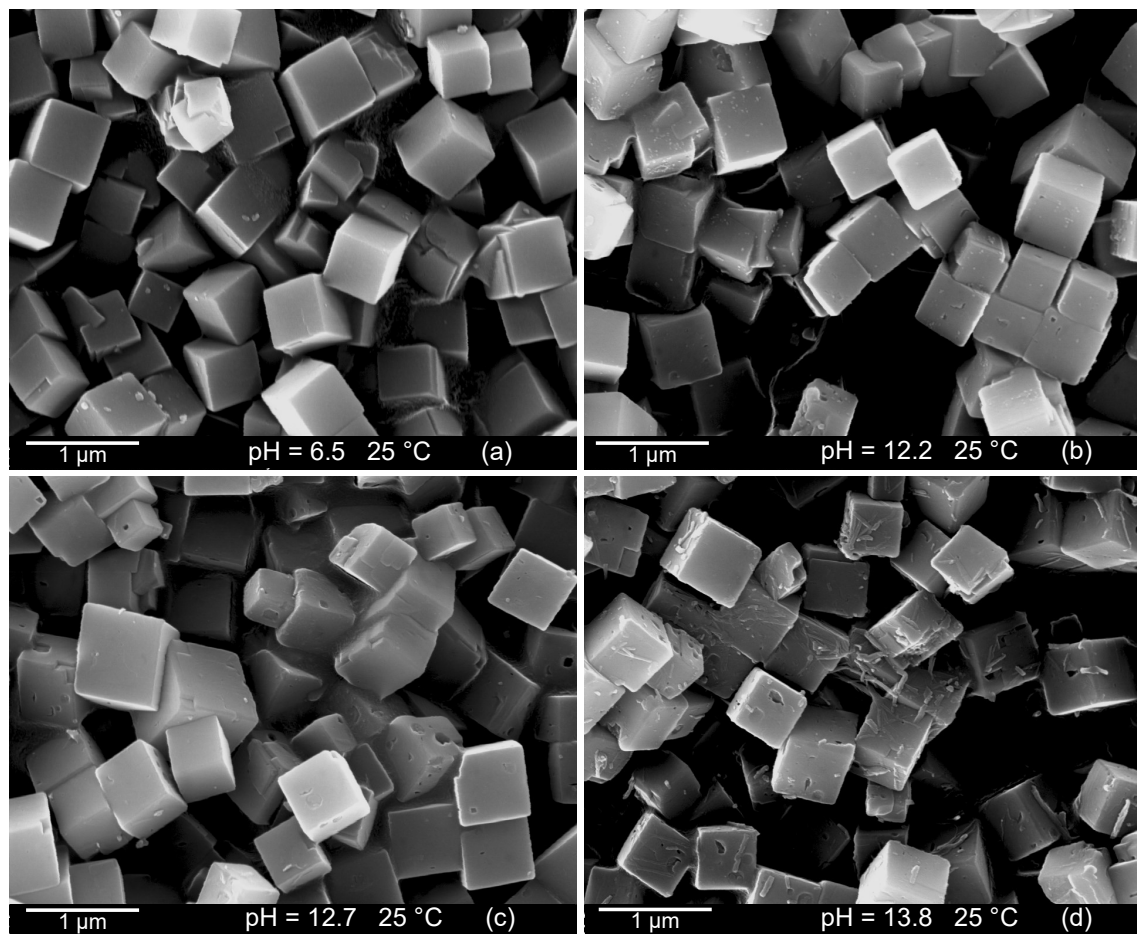
Figure 4.2 SEM images of the NaTi$_2$(PO$_4$)$_3$ samples processed at 25 °C and varying pH.

(Figure 4.4). This suggests that the secondary phase is most likely amorphous or poorly crystalline.

In the 70 °C exposure conditions, corrosion of NTP in aqueous solutions of pH > 12 is also severe. The sample prepared in pH = 12.2 NaOH shows extensive pitting, rounded corners and edges, as well as a large amount of some secondary phase dispersed throughout the particles. This secondary phase does not appear to be morphologically similar to that seen in the sample produced at 25 °C at pH =13.8. The sample produced in pH = 12.7 NaOH at 70 °C, showed a similar amount of corrosion as the one produced at pH = 12.2, though the ratio of distinguishable cubes to precipitate phase was noticeably lower. The precipitate formed at pH = 12.7 also shows

a distinct flake like morphology, in contrast to the more isomorphic morphology of the precipitate formed at pH = 12.2. As could be expected, the sample prepared at pH =13.8 at 70 °C showed the most severe corrosion, with no sign of remaining NTP particles remaining. The precipitated phase for this sample contained some number of particles with the aforementioned flaky morphology and some with needle-like morphology.
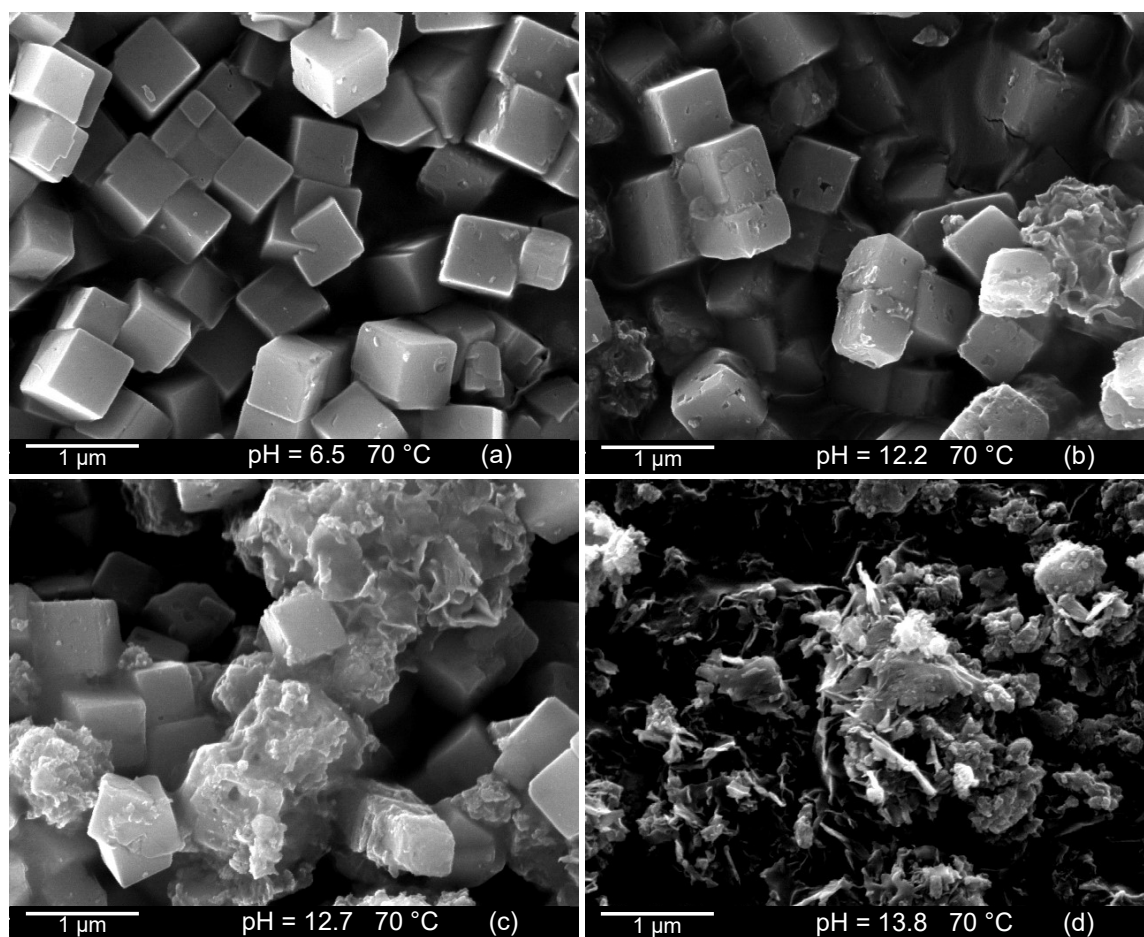
Figure 4.3 SEM images of the $NaTi_2(PO_4)_3$ samples processed at 70 °C and varying pH.

More strikingly, semi-quantitative EDS of the sample showed no residual phosphorous peaks, indicating that the PO_4^{-3} that dissolved from the NTP structure remained in solution. In

order for charge neutrality to be maintained, and assuming no oxidation/reduction of the solvated

titanium species, this would imply the precipitation of 3 OH⁻ for every phosphate dissolved.
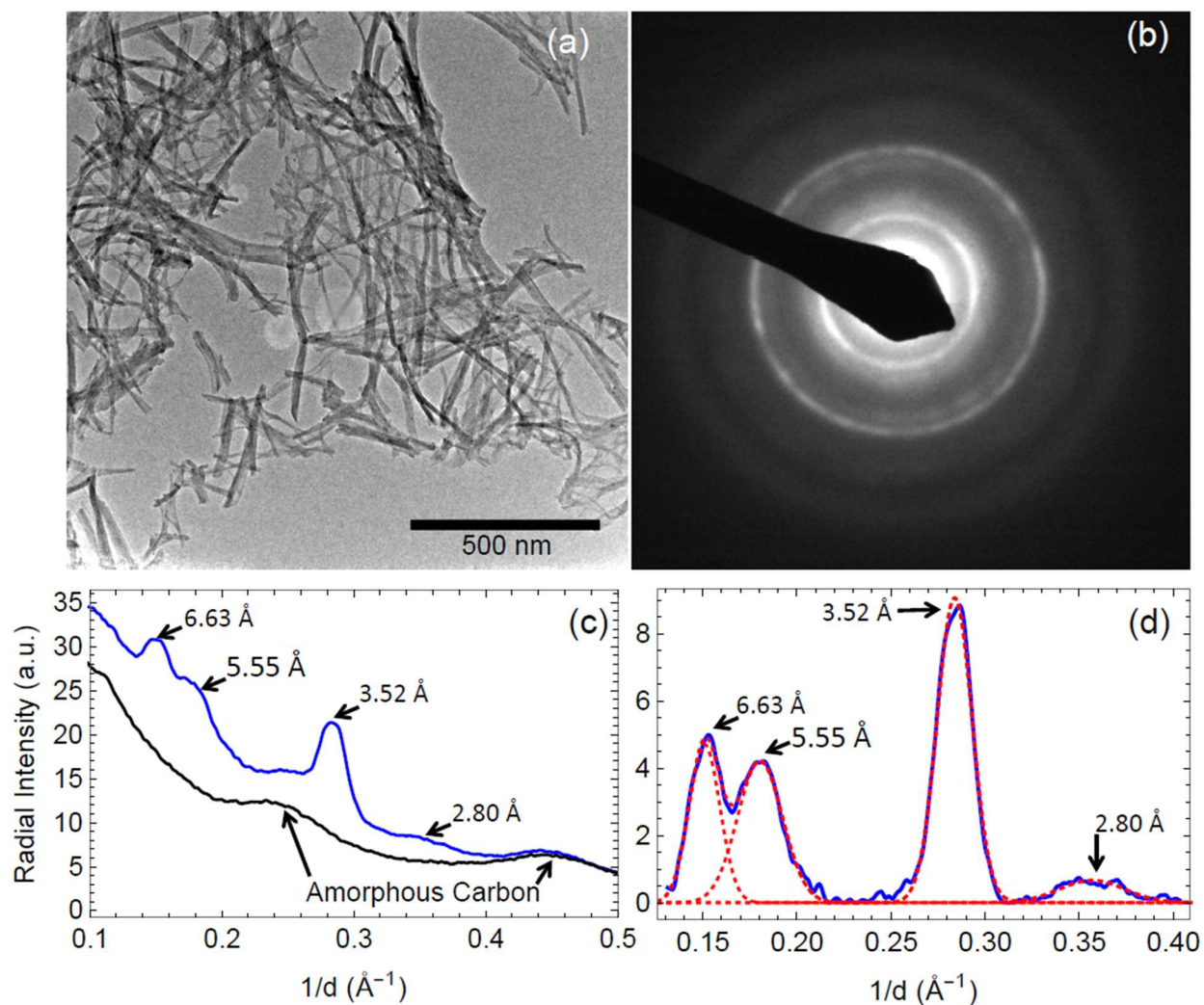
Figure 4.4 TEM image (a) and selected area electron diffraction (SAED) (b) of the secondary precipitate seen in the sample produced at 25 °C and pH 13.8. Radial intensity profile of the precipitate phase and the amorphous carbon grid (c). Radial intensity profile of the precipitate phase after removing the amorphous carbon background (d) and the fitted peak profiles.

Fig. 4.5 shows XRD patterns for the as-synthesized material and samples soaked in 0.1 m

NaNO₃ and 1 m NaOH (pH = 13.8) at 25 °C for 1 week. Samples soaked in pH = 12.2 and 12.7

NaOH at 25°C have not been shown, as they were indistinguishable from the neutral 0.1 m

NaNO₃ sample. In the as-prepared NTP there appears to be some residual amount of both anatase

and rutile, peaks at 25.3° and 27.5°, as well as an unidentified impurity phase with a peak at 22.5° but otherwise agrees well with JCPDS 85-2265. Both the sample soaked in 0.1 M $NaNO_3$ and the material soaked in pH = 13.8 NaOH remain essentially unchanged from the as synthesized material. The only discernable difference was a slight decrease in the peak intensities (to ~ 97% of the original) of NTP and the unknown impurity phase for the sample soaked in pH = 13.8 NaOH, with no decrease in peak intensity of either the anatase or rutile phases. This would seem to indicate that although some corrosion of the NTP phase is occurring it is not as severe as might be expected and that the NTP is preferentially being attacked in place of the anatase or rutile.
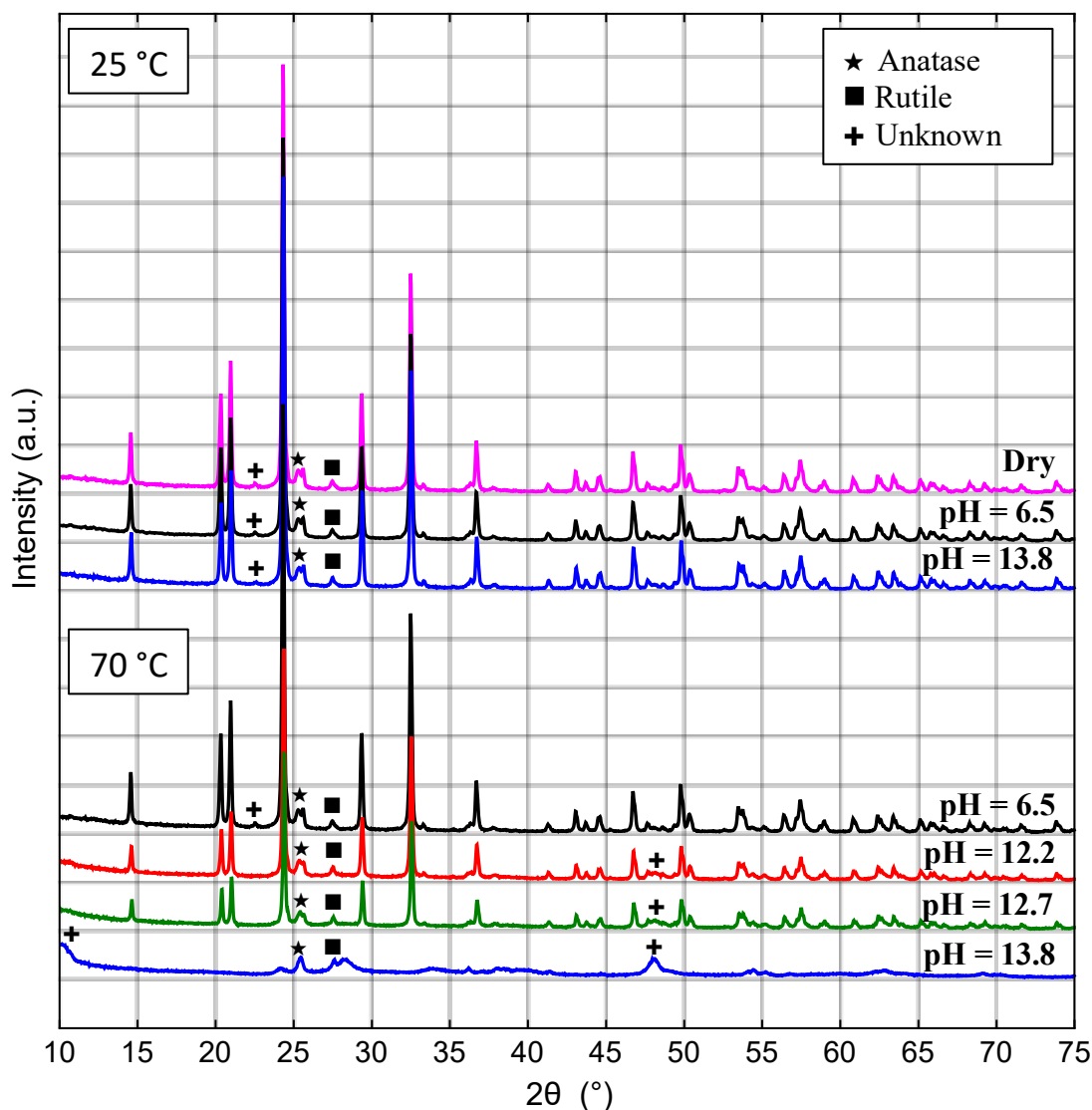
Figure 4.5 XRD patterns of the produced samples. Samples produced at 25 °C and pH 12.2 and 12.7 are not shown.

NTP appears to be stable in 0.1m NaNO₃, even at higher temperatures, but is readily attacked in higher pH solutions. Fig. 4.5 also shows XRD patterns for the samples soaked in 0.1 m NaNO₃ and pH 12.2, 12.7, and 13.8 NaOH at 70 °C for 1 week. Significant changes in peak intensity and the appearance of new peaks occurred in all of the samples at higher pH, with no discernable difference occurring in the sample soaked in 0.1 m NaNO₃. Along with the decrease in NTP peak intensities, a gradual shift to higher 2θ is seen Fig. 4.6a. The nature of this shift is not yet

understood but implies that there is some degree of contraction occurring within the crystal lattice that may be a result of reordering of sodium within the structure. It is also notable that both the anatase and rutile phases remain virtually unchanged in peak intensity. At pH 12.2 and 12.7, new peaks are evident 10.1°, 28.2°, and 48.1°. The peak seen at 10.1° shows up as a broad increase in the background intensity of the pattern, and is characteristic of many layered titanates, particularly those of the form $Na_xH_{2-x}Ti_nO_{2n+1} \cdot yH_2O$[82,83]. This is similarly true for the peak found at 48.1° and is in good agreement with studies of reactions of TiO_2 under hydrothermal conditions in high pH sodium hydroxide[82]. Because of the number of possible phases in this system that share peak positions, it is difficult to index the peaks found to any single phase, especially when the overlapping NTP peaks are taken into account. The sample prepared at 70°C in pH = 13.8 NaOH showed no residual NTP peaks (Fig. 4.6b), though a small peak near 24.3° could be the primary peak for NTP but deviates from the systematic shift to higher 2θ seen in the other samples, suggesting that it is not.
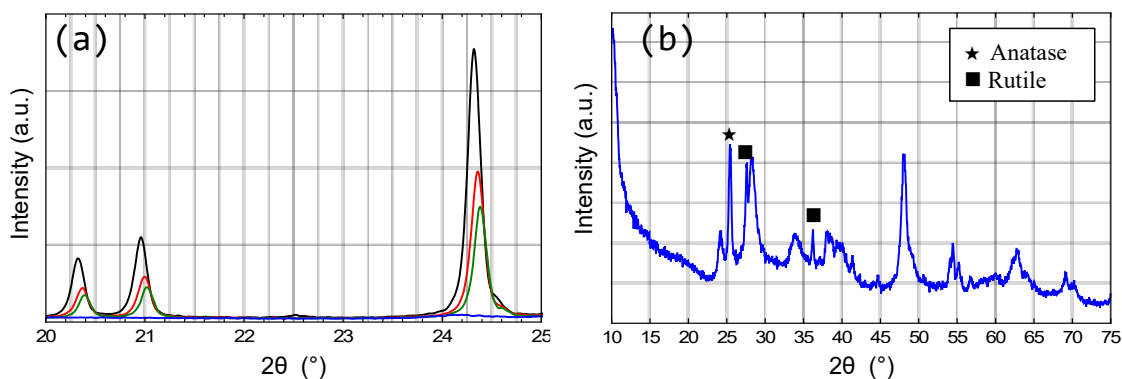
Figure 4.6 (a) Close up XRD pattern of the samples produced at 70 °C, showing the systematic shift to higher 2θ angles when soaked in higher pH solutions. (b) XRD pattern of the sample produced at 70 °C and pH =13.8 with the remaining anatase and rutile peaks labeled.

FTIR results, showing Ti-O vibrational modes in which the oxygen is under-coordinated, coupled with the lack of PO_4 vibrational modes suggest that the primary dissolution mechanism is related to the loss of PO_4^{3-} at high pH. These results can be found in Fig. 4.7. In the samples prepared at 25 °C strong absorption bands at 1230, 1017, and 936 cm^{-1} can be attributed to the antisymmetric and symmetric stretching of the P-O tetrahedrons[84–86].
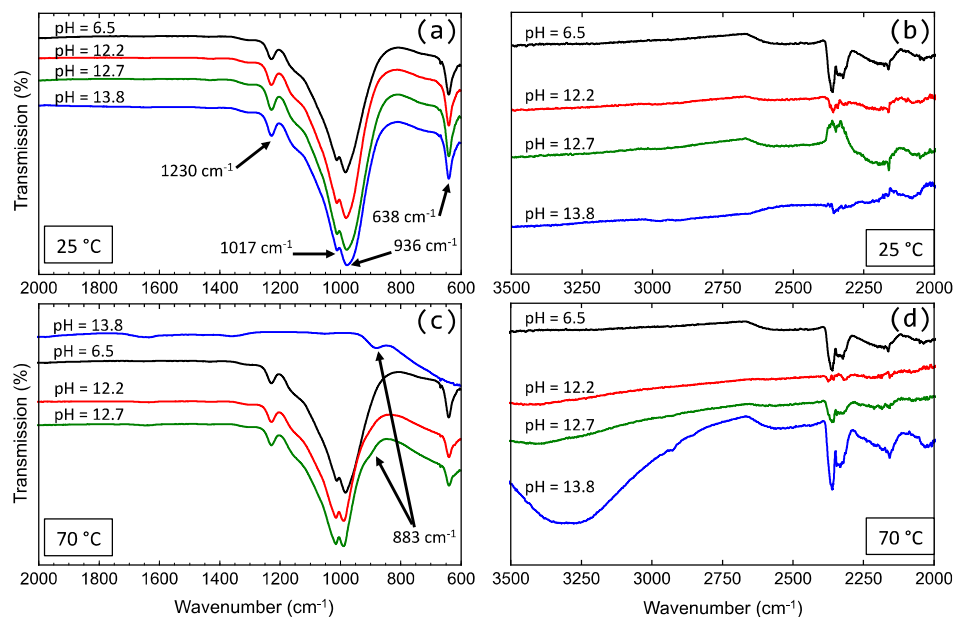
Figure 4.7 FTIR of the samples produced at 25 °C (a,b) and those produced at 70 °C (c,d). The pH at which the sample was produce can be found above the spectra line.

At 638 cm^{-1} the absorption peak has been attributed to bending vibrations of the PO_4 tetrahedron[84–86]. These data agree well with previously published spectrums for NASICON based materials including NTP. For the samples prepared at 70 °C, a broad peak at 3400 cm^{-1} (Fig. 4.7d) related to vibrations of physically absorbed H_2O develops and becomes more pronounced at higher pH. This is clear evidence for the formation of crystals containing structural water. The absorption peaks at 1640cm^{-1} and 1360 cm^{-1} (Fig. 4.8) can be assigned to H-O-H binding and the Ti-O vibrational modes[87]. In all of the samples prepared at 70 °C a peak develops at 883 cm^{-1} that can be attributed to Ti-O stretching modes in which the oxygen is

non-bridging, such as in the layered titanates[88]. A more complete characterization of the reaction products formed at 25 °C and elevated temperatures is an ongoing area of research within our group.
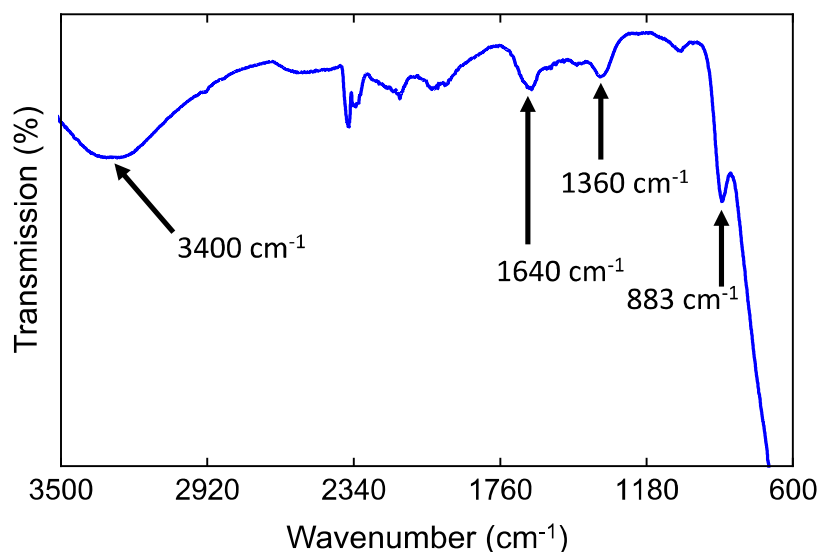
Figure 4.8 Close up FTIR spectrum of the sample produced at 70 °C and pH =13.8.

4.3.3 Electrochemical performance

Cyclic voltammetry and GCPL were used in order to determine the effect of the observed degradation on the electrochemical performance of the NTP. For samples conditioned at 25 °C at the pH = 12.2 and pH = 12.7 there is a small but measurable decrease in the specific current to 90 % and 88 % of the baseline respectively, for both the oxidation and reduction peaks, indicating that the alteration of the material at these pHs has caused some amount of capacity loss (Fig. 4.9a). This loss cannot be directly attributed to loss of material since the samples were prepared from measured masses and no secondary phase was visible in these samples. It is possible that poor dispersion of the carbon black conductive additive in areas where pitting had occurred resulted in regions of low electrochemical activity and consequently a lower specific

current was observed. The irreversible exchange of sodium for protons within the structure, leaving regions of the NTP crystal electrochemically in active, is another possibility in aqueous solutions that would explain the observed decrease in the specific current.
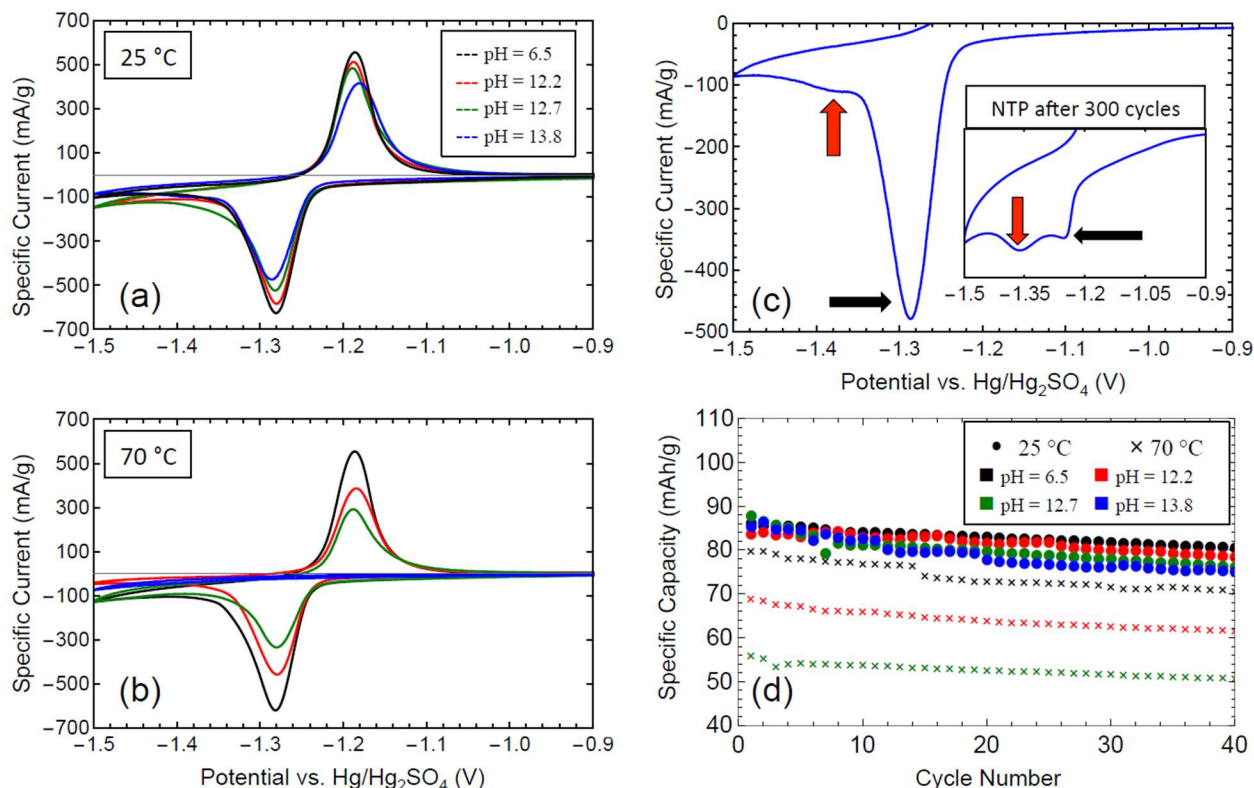
Figure 4.9 Cyclic voltammetry of the samples produced at 25 °C (a) and 70 °C (b). All samples were run at 0.100 mV/s and only the fifth cycle of each is plotted for clarity. The reduction peak of the cyclic voltammetry performed on the sample produced at 25 °C and pH =13.8 (c), with the primary reduction peak indicated by the black arrow and the secondary peak indicated by the red arrow. The inset of (c) shows pristine sample of $NaTi_2(PO_4)_3$ after 300 CV cycles at a scan rate of 0.25 mV/s. The same secondary reduction peak is much more visible. Specific capacity vs cycle number, under GCPL conditions at a C/3 rate (d) shows the performance of the samples in 1M, neutral pH Na_2SO_4 after exposure.

Samples prepared at 70 °C (Fig. 4.9b) showed considerable decreases in the specific current of both reduction and oxidation peaks, with the sample prepared at pH = 13.8 showing no peaks whatsoever. This is not surprising since the layered titanates do not undergo reduction until voltages substantially lower than those tested. Interestingly, this suggests that the secondary phase seen in the sample prepared at 25 °C and pH = 13.8 is not the same as seen in the materials prepared at higher temperatures. It was also found that after several weeks of exposure to air the sample prepared at 25 °C and pH = 13.8 no longer showed the secondary reduction peak. This

coupled with limited conditions in which this secondary precipitate forms suggests the phase is metastable under normal ambient conditions.

GCPL for all samples, except for the one prepared at 70 °C and pH=13.8 (the specific capacity was < 1 mAh/g for this sample), can be found in Fig. 4.9d. Samples prepared at 25 °C had roughly equivalent capacities for the first several cycles, with no trend in capacity for the initial 10 cycles. This is in stark contrast to the trends seen in the CV results, where the capacity is more closely related to the rate capability of the material.

By cycle 20 the specific capacities of these samples have separated such that the samples prepared at higher pH have lower capacity. However, the rate at which capacity is being lost appears to be equivalent in later cycles. This is true even for the samples prepared at 70 °C. Notably, the sample prepared in neutral pH and 70 °C shows a lower capacity then all samples prepared at 25 °C, which was not observed in the CV results. That the measured capacity of this sample should be comparably higher than the samples prepared at 25 °C when tested under CV conditions but lower when tested under GCPL conditions indicates that the reaction of NTP with high pH solutions, even at room temperature, causes a decrease in the rate performance of the electrochemical reaction. This could be due to changes in the crystal structure near the surface of the particles caused by reaction with hydroxide. Further investigation is needed to fully understand these changes.

The dissolution of NTP in high pH aqueous solutions appears to cause some amount of capacity fading, though the capacity loss is not as severe as has been reported in the literature when the material is cycled. However, since the performance here is normalized to a measured mass after exposure, we cannot accurately account for mass loss during cycling that results from dissolution of the NTP. It is also clear from comparing the CV and GCPL results that exposure to

high pH electrolyte causes a decrease in the rate performance of NTP such that the sample produced at 70 °C and neutral pH performs better than samples produced at elevated pH and 25 °C under CV conditions, but worse under GCPL conditions. It would also appear that unless the pH of the electrolyte within the electrode is on the order of ~13.8, the dissolution of material should stop once the solution becomes saturated with titanium species since there is not a thermodynamically stable phase to act as a sink for the continued dissolution. In an electrochemical system, however, it is possible that a pH swing within the electrode will cause a continual dissolution/precipitation process to occur with the steps being (1) upon reduction the direct reaction between the fully sodiated NTP and H_2O, as well as the electrochemical decomposition of water, generate some amount OH^-, (2) as the pH increases due to the increase in OH^- concentration some amount of NTP is dissolved, (3) upon oxidation the OH^- concentration within the electrode decreases as it diffuses out of the electrode into the bulk, (4) if the dissolved titanium species diffuse slower than the OH^-, then the solution inside of the electrolyte becomes supersaturated with titanium species, (5) the excess titanium species precipitate out as a secondary phase. Further investigation will be needed to determine whether or not this is occurring.

Furthermore, these results should be relevant to the electrochemical performance, upon exposure to high pH environments, of other NASICON type materials including, $LiTi_2(PO_4)_3$ and $KTi_2(PO_4)_3$. From the obtained results, it appears that the dissolution of NTP is mediated through loss of phosphate, or to put it another way, attack of the oxygen that bridges the PO_4 tetrahedra and TiO_6 octahedra in these materials. Because of this, the authors do not believe the overall solubility of titanium phosphate based electrodes should be affected by the particular alkali metal cations present. However, the difference in surface structure between Na, Li, and K based

titanium phosphates may change the overall rate at which the hydrogen evolution reaction occurs and thusly change the rate of OH- generation.

4.4 Conclusion

The inherent chemical stability of $NaTi_2(PO_4)_3$ in aqueous NaOH has been investigated and was found to begin dissolving above pH = 11, though the solubility remains quite low until pH > 13. At 25 °C and pH > 13 an unidentified phase with an elongated morphology becomes thermodynamically favorable and begins to precipitate from solution. This secondary phase acts as a sink for dissolved titanium allowing for the continual dissolution of NTP rather than eventual saturation of solvated titanium species. Electrochemical testing of the corroded material seemed to indicate that the corrosion seen at 25 °C had only a small effect on the overall performance of the NTP particles, indicating that the loss of capacity reported in the literature, under normal cycling conditions, cannot be fully explained by the dissolution of the material that occurs under no electrochemical bias.

These results suggest that increases in pH within porous electrodes of NTP will pose a long-term degradation problem. As such, a stable conformal coating, such as those used in organic Na-ion systems[89], would be necessary in order to prevent dissolution in higher pH electrolytes and is an ongoing area of research within our group. They also give clear evidence of a degradation mechanism, other than the reaction with dissolved O_2, that should be accounted for when designing aqueous batteries of these materials. Further investigation will be needed to quantify the degree to which pH changes occur in NTP based electrodes during electrochemical cycling in aqueous electrolyte, and what techniques can be used to mitigate the detrimental effects of the pH change. We will focus on understanding how compositing NTP with activated carbon

improves the long-term cycle stability of NTP electrodes. Previous results from our research

indicates such compositing is quite effective, however, the mechanisms for this improvement are

not well understood [90].

Chapter 5: In Situ pH Measurements During Electrochemical Cycling

5.1 Overview

Now that we have an idea of how high pH solutions will affect the performance of NTP, we'd like to know how the pH of an NTP electrode in neutral Na_2SO_4 electrolyte changes during cycling. We know that the solution should become basic, but since this assumption relies on thermodynamics only, it is hard to know a priori how kinetics will affect the actual magnitude of the pH swing. In order to do this we've designed two fixtures to allow for in-situ pH measurements of electrodes during cycling. One allows for measurements in a cyclic voltammetry type cell, where there exists a large reservoir of electrolyte and a platinum wire counter electrode that generates protons during cycling that will neutralize OH^- in the bulk. This particular set up allows us to carry out in situ pH measurements without worrying about complications caused by reactions at the cathode, and allows for more direct comparison to results in the literature where CV was used.

The second fixture allows for measurements in a galvanostatic full cell, with the anode in close proximity to the cathode (which can be made of any number of active materials) and with little to no excess electrolyte. Results from this setup are more closely related to what could be expected in a real-world application, though effects from the close proximity of the cathode may make interpretation of the data more difficult.

5.2 Experimental

5.2.1 Diffusion Reaction Model of NTP in a CV Half Cell

 The first fixture, found in Figure 5.1, is designed to allow for measurement of pH at the surface

of an electrode pellet, within electrolyte that is separated from the bulk electrolyte of a CV cell.

In order to understand how the measured pH relates to the pH within the pellet, it is useful to

construct a simple 1D diffusion reaction model, ignoring migration effects.

$$\frac{\partial c}{\partial t} = D \frac{\partial^2 c}{\partial x^2} + r(c)$$

In this equation, c is the concentration, D is the diffusion coefficient, and r is the reaction term as

a function of concentration. We assumed that hydroxide was generated only by the

electrochemical process with Butler-Volmer type kinetics, with the equilibrium potential for the

reaction being defined by the local pH as E^0 = -0.0591pH, and the actual potential being an input

that changes at a constant rate just as it would in a normal CV scan. We also assumed that the

reaction only occurs in one direction (water generation from hydrogen oxidation and reaction

with hydroxide does not occur). The exchange current was scaled to an assumed electrochemical

surface area, calculated as follows: Based on an electrode composition of 70 wt% NTP (2.8

g/cm^3), 20 wt% CB (1.8 g/cm^3), 10 wt% PVDF(1.8 g/cm^3), the bulk density of the composite

will be 2.5 g/cm^3. Based on the measured mass and volume of a 10mm diameter pellet, the

porosity was estimated to be between 0.2-0.3 for these composites. So the density of electrodes,

including their porosity would be $\sim$ 2 g/cm^3. If we then assume that the electrochemical surface

area for hydrogen evolution within this composite material is 50 m^2/g, Then a 50 mg pellet will

have a total area of 25000 cm^2 and a thickness of 0.03185 cm (319 μm). This implies an area per

unit thickness of 78.4 cm^2/μm.

For this given set up we assumed a no-flux boundary condition within the region that the pH is being measured and an infinite reservoir of electrolyte was assumed on the opposite side of the pellet. The diffusion of ions through the pellet was defined as an effective diffusivity based on the porosity and tortuosity. A diffusion coefficient for hydroxide ions of 5.27×10^{-5} cm^2/s was used and assumed to be constant. With these conditions, we discretized the domain into three regions, bulk electrolyte, pellet, and measured electrolyte chamber, and used the Crank-Nicolson method for solving this system.

The Crank-Nicolson method is implicit in time and is unconditionally stable for any time step [91]. It can be thought of as a central difference method in space and a trapezoidal method in time. This leads to the following discretization for the diffusion reaction equation:

$$\frac{\partial C}{\partial t} = \frac{D}{2 \Delta x} \left(C_{j+1}^n - 2 C_j^n + C_{j-1}^n + C_{j+1}^{n+1} - 2 C_j^{n+1} + C_j^{n+1} \right) + r(C_j^n)$$

$$\frac{(C_j^{n+1} - C_j^n)}{\Delta t} = \frac{D}{2 \Delta x} \left(C_{j+1}^n - 2 C_j^n + C_{j-1}^n + C_{j+1}^{n+1} - 2 C_j^{n+1} + C_j^{n+1} \right) + r(C_j^n)$$

If we collect discretization and diffusion terms into a single parameter and call that parameter σ, and collect the forward time step terms on the left and current time step terms on the right we obtain:

$$\sigma = \frac{D \Delta t}{2 \Delta x^2}$$

$$-\sigma C_{j-1}^{n+1} + (1 + 2 \sigma) C_j^{n+1} - \sigma C_{j+1}^{n+1} = \sigma C_{j-1}^n + (1 - 2 \sigma) C_j^n + \sigma C_{j+1}^n + \Delta t \, r(C_j^n)$$

Accounting for the difference in diffusional properties at the boundary of the pellet and the bulk electrolyte was accomplished by using the following expressions for the boundary nodes:

$$-\sigma_b C_{j-1}^{n+1} + (1 + \sigma_b + \sigma_P) C_j^{n+1} - \sigma_P C_{j+1}^{n+1} = \sigma_b C_{j-1}^n + (1 - \sigma_b - \sigma_P) C_j^n + \sigma_P C_{j+1}^n + \Delta t \, r(C_j^n)$$

$$-\sigma_P C_{j-1}^{n+1} + (1 + \sigma_c + \sigma_P) C_j^{n+1} - \sigma_c C_{j+1}^{n+1} = \sigma_P C_{j-1}^n + (1 - \sigma_c - \sigma_P) C_j^n + \sigma_c C_{j+1}^n + \Delta t \, r(C_j^n)$$

Here, σ_b represents the diffusional parameter within the bulk electrolyte, σ_P represents the diffusional properties within the electrode pellet, and σ_c represents the diffusional parameters

within the measurement chamber. Collecting the σ containing terms into two matrices, A and B, and writing the concentration terms and reaction term as vectors, C and r, we obtain:

$$A\,C^{n+1} = B\,C^n + r^n$$
$$C^{n+1} = A^{-1}(B\,C^n + r^n)$$

Although this solution method contains an inverse matrix operation, which is generally computationally expensive, we will assume the effective diffusion coefficients are constant so the inverse only needs to be calculated a single time. It should be noted here, however, that the diffusional properties within the electrode will most certainly change during cycling. Aside from the HER reaction generating OH-, it also generates $H_2(g)$. As the dissolved $H_2(g)$ reaches high enough concentrations, it will precipitate out as bubbles within the porous structure of the electrode, occluding the pores. Occlusion of the pore volume of the electrode would have noticeable effects on the porosity, tortuosity, and electrochemical surface area of the electrode and as a consequence, the effective diffusivity and exchange current used in this model would change during cycling. This has not been accounted for in the model for the following reasons: (1) the equilibrium volume of a $H_2(g)$ bubble will depend largely on pore size (which varies throughout the electrode) and hydrophilicity, so determining the decrease in porosity of the electrode based on the total current passed is not straight forward, (2) the effect of the equilibrium volume of $H_2(g)$ bubbles on the ECSA depends on the pore geometry, with flat pores losing more ECSA than cylindrical pores for a given volume of $H_2(g)$, because of this the decrease in exchange current due to lost surface area is difficult to predict, (3) it is not clear what the relationship between occluded pores and tortuosity would be since the geometry of the pore network is not known, and (4) the two matrices A and B would need to be rebuilt during each step and the inverse of A would need to be recalculated, greatly increasing the computational expense of the simple model.
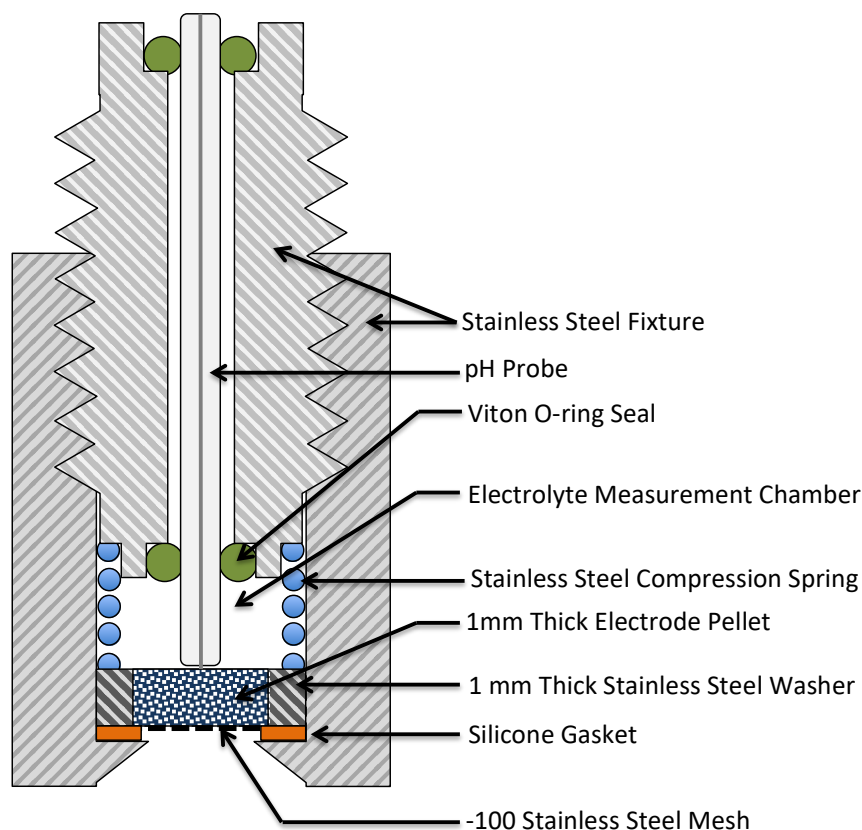
Figure 5.1 Cut away schematic of the test fixture used for in situ pH measurements in a CV type half-cell.

5.2.2 Material Preparation

The NTP electrode material for both test setups was prepared by the solvothermal method described in chapter 3.2. This NTP was mixed with carbon black and PVDF in a weight ratio of 70:20:10 in a mortar and pestle, after which several drops of NMP were added. This mixture was creamed into a thick paste before being placed in an oven at 80 °C overnight. The dried material was run through an 80 x 80 mesh stainless steel screen to obtain a homogenous granulate. For the CV type set up, this powder was compacted within the cavity of a 1 mm thick 316 stainless steel washer. A 10 mm diameter pellet was pressed at 3 tonne for the GCPL set up.

5.2.3 Electrochemical Characterization

For the CV type set up, a platinum wire counter electrode and MSE reference electrode were used. The electrode was scanned from -0.5 V to -1.5 V at a scan rate of 0.100 mV/s for a total of twenty cycles. The pH probe used was first calibrated using pH 4, 7, and 10 calibration solutions, with temperature correction. During cycling the pH was measured every 30 seconds.

The test set up for the GCPL experiment can be found in Figure 5.2, the pH probe is inserted through the hole on the left. In this particular setup there was no excess electrolyte, just enough to provide a film for ionic contact between the reference electrode and the electrode assembly, and the counter electrode was $Na_{0.44}MnO_2$ (NMO) rather than a platinum wire. NMO electrodes were prepared with carbon black and PVDF in the same manner as the NTP electrode. Two different mass ratios of cathode to anode were used 2.5:1 and 1.75:1, this allowed us to observe the effect of cathode potential on the pHs experienced in the cell.
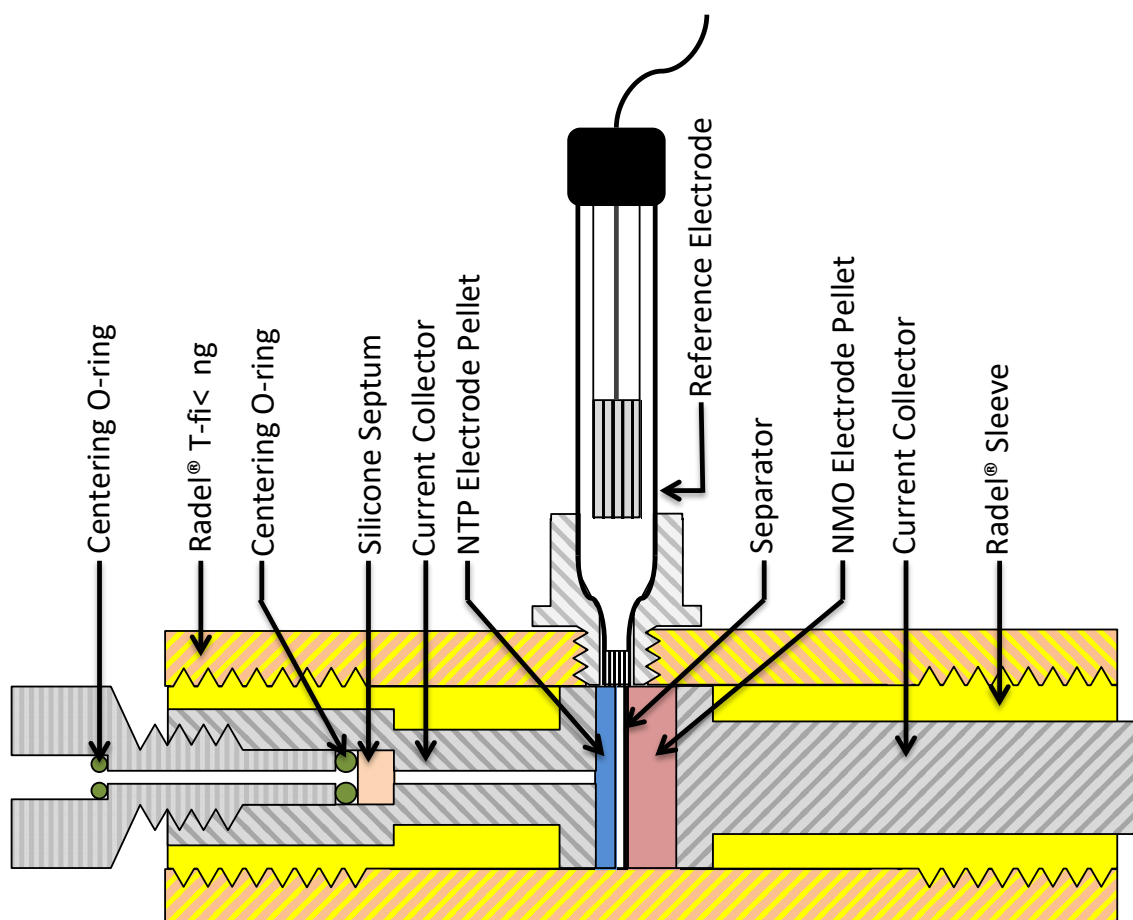
Figure 5.2 Cut away schematic of the test fixture used for the in situ pH measurement in a galvanostatic full cell type configuration.

5.3 Results and Discussion

5.3.1 In Situ pH Measurement of a CV Half Cell

The results of this simple simulation (Figure 5.3) indicated that the pH should increase during the reduction process and decrease as hydroxide ions diffuse through the pellet and into the bulk of the system during oxidation. Since the overpotential of the reaction is defined by the local pH, as the pH increases within the pellet the rate of hydroxide generation decreased. This led to a slower and slower increase in pH with each cycle and a smaller and smaller swing in the measured pH.
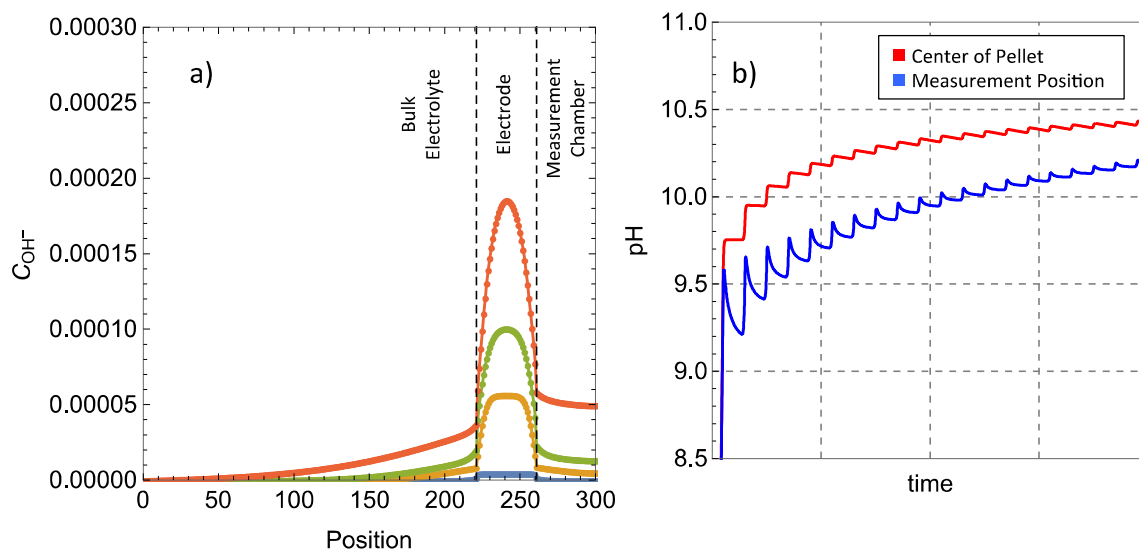
Figure 5.3 Simulated results of (a) concentration profile of hydroxide as a function of position, showing the change with time during the first CV cycle and (b) pH at the edge of the measurement chamber and in the center of the pellet.

The general trends of the simulation matched well with the measured experimental results (Figure 5.4), with the exception of a few features that cannot be captured with such a simple model. The first obvious difference was the initial swings in pH during cycling. The measured pH values showed a considerably larger swing between the low and high potentials. This could be explained by certain chemical reactions that are not captured in the model. For instance, the initial pH of the experiment was always between 3.5 and 4.5 indicating that upon submerging the NTP electrode in electrolyte protons are released into the system. These protons would then react with any hydroxide generated in the system decreasing the concentration of protons in a manner that could not be captured in the simple simulation. Similarly, the platinum wire counter electrode will produce protons when the working electrode is undergoing reduction, so rather than the measured pH being related solely to the diffusion of OH⁻ it is expected that there will be some degree of neutralization in the bulk electrolyte which could account for the difference in magnitude of the pH swing between the simulation and experiment.
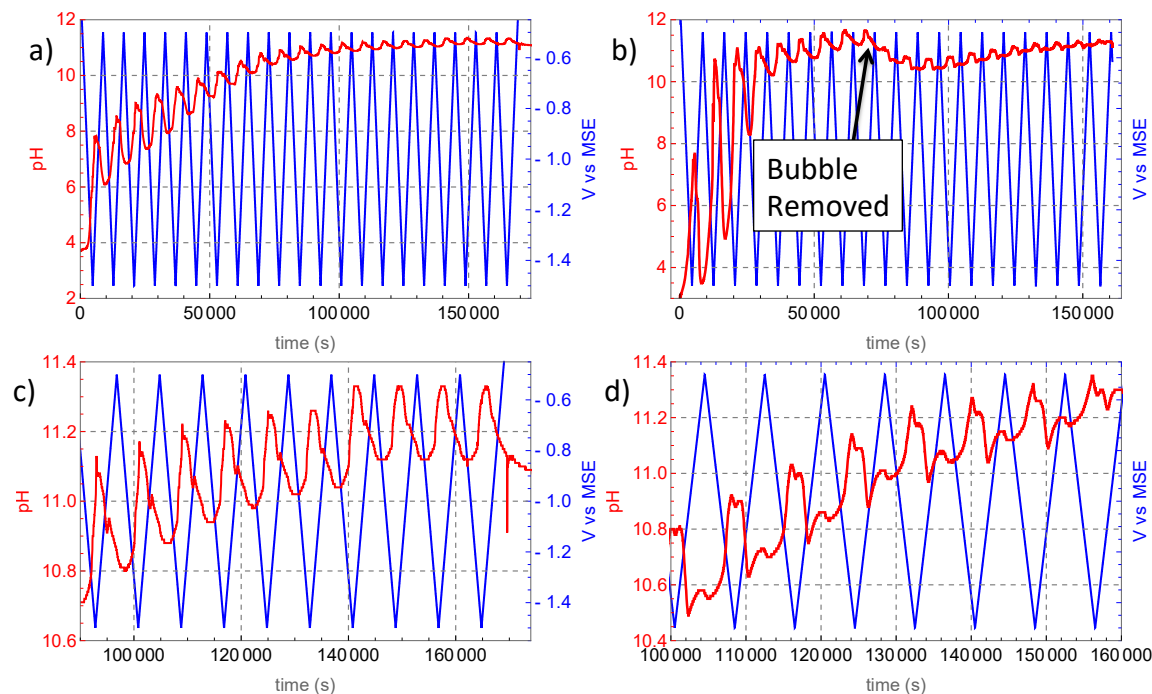
Figure 5.4 (a,b) In Situ pH measurements for two different test runs. The red line represents the pH and the blue line represents the applied potential. A close up of (a) can be found in (c) and a close up of (b) can be found in (d). The sudden drop seen in (b) was caused by bubble removal from the surface of the pellet into the bulk electrolyte.

The experimental results also showed an unexpected increase in pH during oxidation, where hydroxide ions should be continuing to diffuse out of the system. A plot of the pH as a function of potential, shown in Figure 5.5, gives a better view of this phenomenon, which appears as a hump around -0.85 V vs. MSE. The nature of this increase in pH is unknown. However, given that the soluble phase of titanium at high pH is $Ti(OH)_5^-$, it is possible that once the pH begins to drop $Ti(OH)_5^-$ becomes supersaturated and precipitates as $Ti(OH)_4$ back into the system, releasing OH⁻ back into the system. Although this could account for a small increase in pH, the magnitude of the hump is far too large, and the total solvated Ti far too low at these pH to fully account for this affect. A similar hump was reported at a potential of -0.7 V vs. MSE when cycling a high surface area porous carbon electrode in 0.172 M NaCl [92]. In that experiment, the shape of the pH curves were attributed to some amount of surface reactions on the carbon as

well as the incorporation of ions into the double layer during reduction/oxidation of the electrode. Since the NTP electrodes used in these experiments contain a large quantity of carbon black to enhance conductivity, it is possible that the feature is related not to the chemistry of NTP but to that of the conductive carbon surface.
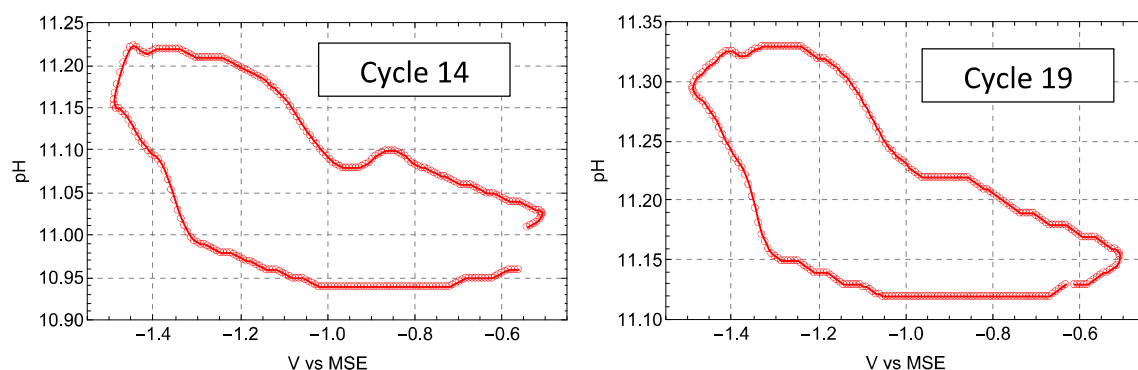
Figure 5.5 Graphs showing the pH as a function of potential for the 14th and 19th cycle from figure 5.4a. The data obtained from the run shown in figure 5.4b showed similar behavior until after the surface bubble was removed.

The experimental results were somewhat inconsistent in the magnitude of pH swing, rate of increase of the pH, and the equilibrium pH attained after numerous cycles. This was in part due to the nucleation of bubbles on both the reference electrode and the opening of the text fixture that connects the pellet to the bulk electrolyte. An example of how this effected the measurement is shown in Figure 5.4b. There were also variations that arose from differences in just how well the silicone gasket sealed the electrolyte measurement chamber from the bulk. Despite these shortcomings, the tests were remarkably consistent in the features that they show when the pH is plotted as a function of potential.

As mentioned in the previous section on the inherent chemical stability of NTP in basic solutions, if a pH swing occurs during electrochemical cycling, dissolution at high pH followed by supersaturation and precipitation of titanium species at lower pH will lead to a persistent

capacity fade. The measured pH during cycling, though lower than the pH at which the

secondary phase precipitated in the previous experiment, does increase above the pH 11

threshold for increased solubility of NTP. In order to form a better understanding of how the pH

changes during cycling, a rate study should be carried out. It would also be useful to measure

how the cutoff potential for reduction affects the measured pH of the system.

5.3.2 In Situ pH Measurement in a Galvanostatic Full Cell

The experimental results for galvanostatic cycling of full cells can be found in Figure 5.6

(cathode to anode mass ratio of 2.5:1) and Figure 5.7 (cathode to anode mass ratio of 1.75:1).

Both cells showed sudden changes in measured pH upon switching from charge to discharge

conditions.
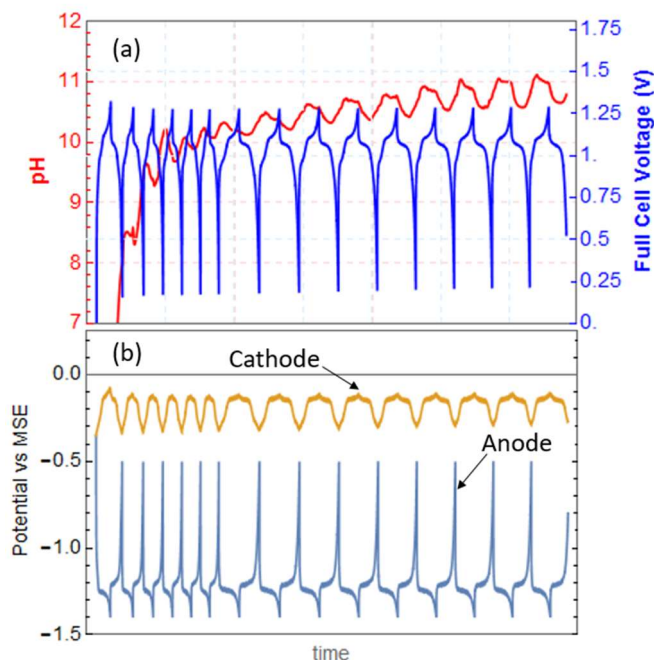
Figure 5.6 Results for the (a) pH and full cell potential and (b) anode and cathode potentials, for a full cell with a cathode to anode mass ratio of 2.5:1.

This indicates that either migration effects or double layer effects are influencing the measured pH. When the electric field is switched at the electrode, switching the current from reductive to oxidative, we observed a sudden increase in the measured pH. After this sudden spike the measured pH stabilized back to the trend line. The opposite effect is seen when the current is switched from oxidative to reductive. In both cases the actual time for the pH to spike and then relax was a few minutes, which indicates it is not likely to be measurement artifact of the pH probe.
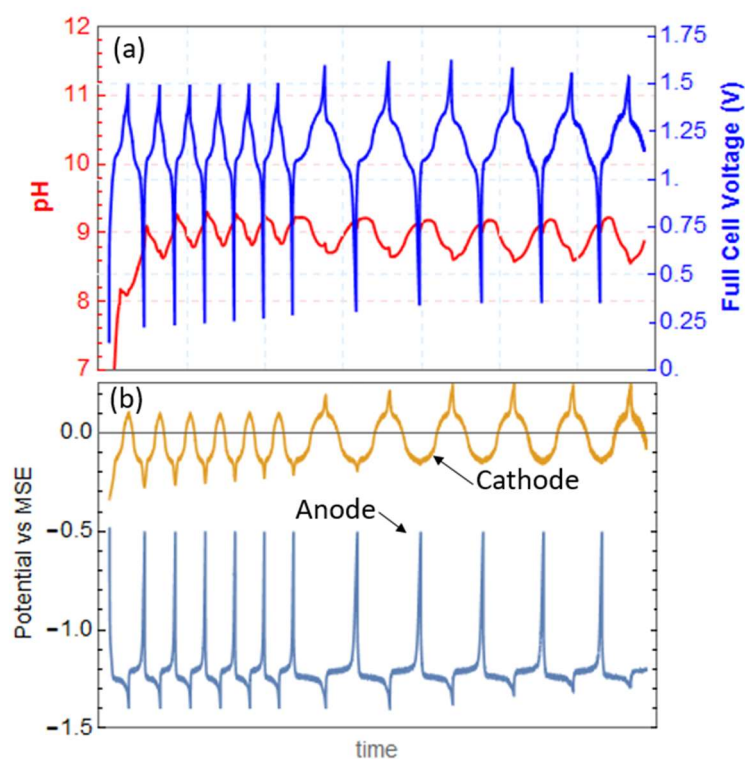
Figure 5.7 Results for the (a) pH and full cell potential and (b) anode and cathode potentials, for a full cell with a cathode to anode mass ratio of 1.75:1

Interestingly, it was found that the measured pH actually begins to decrease during the charge step (reduction at the anode), which is counter-intuitive and in stark contrast to what was observed during half-cell cycling. When the mass ratio of cathode to anode was 2.5:1, the upper potential of the cathode was -0.1 V vs MSE (Fig 5.6b) during cycling. This upper potential was

reached both at the fast and slow rates and did not drift to higher potentials with increasing cycle number. This resulted in a measured pH that continued to increase during cycling, with a maximum measured pH of 11.2.

When the mass ratio of cathode to anode was 1.75:1, the upper potential was 0.1 V for the fast rate and 0.25 V for the slow rate. Upon switching from the slow rate to fast rate, the upper potential of the cathode drifts to higher potentials, finally reaching 0.25 V which was set as the potential limit for the cathode material (NMO is almost completely desodiated at this potential and begins to become overoxidized if pushed to higher potentials). This means the cycling of the cell switched from an anode limited potential to a cathode limited potential. Correspondingly, the measured pH was much lower than in the cathode heavy cell, reaching a maximum pH of 9.3. In addition to having a lower pH, because the cell became cathode limited, the anode experienced less extreme negative potentials leading to a decrease in pH with increasing cycle number. These results, a decrease in pH during charging and the maximum pH being dependent on the cathode to anode mass ratio, indicate that the cell pH is being stabilized by the oxygen evolution reaction (OER) that occurs at the cathode.

OER at the cathode is induced at the cathode-separator interface through an increase in pH caused by OH^- diffusion from the anode. Figure 5.8 gives a qualitative picture of the mechanism involved. The steps in this process are as follows assuming a starting electrolyte that is neutral: (1) a current is applied to the full cell, this leads to the anode potential decreasing and the cathode potential increasing, and because NTP is a phase change electrode NTP reaches HER well before the cathode reaches OER (Fig 5.8a), (2) as the anode's pH continues to increase, OH^- diffuses through the separator to the cathode causing the cathodes pH to increase(Fig 5.8b), (3)

eventually the potential of the cathode and the pH near the cathode separator interface are high enough for OER to begin at the cathode, $H_2O \leftrightarrow \frac{1}{2}O_2(g) + 2H^+ + 2e^-$ (Fig 5.8c), (4) protons generated from OER diffuse through the cell neutralizing the hydroxide that has been generated(Fig 5.8d). Aside from protons, OER also generates $O_2(g)$, which raises the problem of chemical oxidation of the charged anode. The magnitude of the OER reaction will depend on the catalytic properties of the cathode materials towards oxygen evolution, as well as the cathodes upper potential. For instance, manganese(IV) oxides, such as those used in this experiment, are among the best oxygen evolution catalysts.
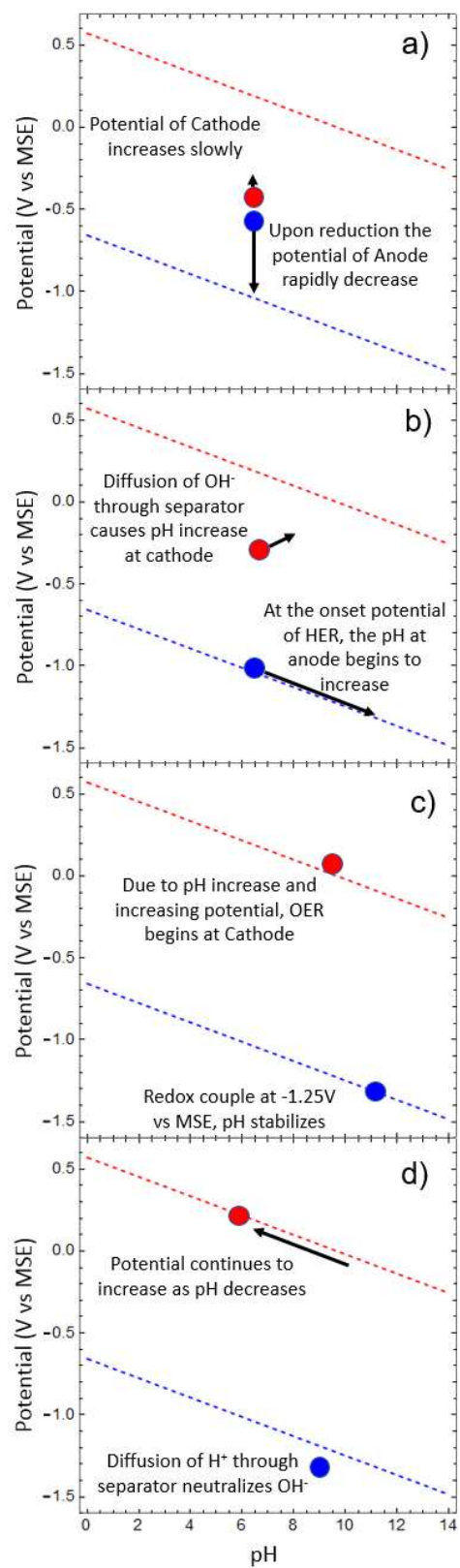
Figure 5.8 Pourbaix diagrams showing the qualitative explanation of observed pH swings in full cells.

5.4 Conclusion

Reports in the literature indicate that when cycled at high rates, the capacity fade of NTP is minimal, but when cycling slowly the capacity fade is significant. This can be easily explained by noting the reactions that generate hydroxide and hydrogen will occur below a certain potential, and so the total amount of hydroxide and hydrogen generated will be proportional to the total time spent below that potential. The degree to which the reaction products remain or interfere with cell performance will depend on the test cell being utilized. When an NTP electrode is in close proximity to a NMO cathode, diffusion of OH^- through the separator leads to a lowering of the onset potential for OER at the cathode. Once the OER reaction has begun at the cathode, proton diffusion towards the anode acts to neutralize the OH^- being produced at the anode.

Chapter 6: Impacting Cycle Stability via Polymeric Coatings

This work has been published in The Journal of the Electrochemical Society.[37]

6.1 Overview

As mentioned in chapter 2.3.1, application of carbon based surface coatings is the most commonly used method to enhance long term stability of electrode systems. A properly chosen coating can lower charge transfer resistance, increase chemical resistance, and enhance fracture toughness of the active material. One method that has proven useful in the stabilization of aqueous electrode materials is the coating of active material with an electronically conducting or functionalized/conjugated polymer material that is stable in the electrolyte [14,26,45,93,94]. Conjugated polymers are linear molecules with partially filled valence or conduction bands. Their structure is based on a series of alternating double and single bonds, which leads to a network of sp^2-hybridized bonds with the p_z-orbitals of the carbon atoms overlapping, leading to the delocalization of charge carriers along the backbone of the polymer chain[95]. Similar to inorganic semiconductors, these polymers can be doped to become either n-type or p-type, dramatically increasing the electronic conductivity of the polymer. The conductivity of these polymers can range from 10^{-10} to 10^3 S/cm depending on synthesis method and the degree of doping[96–98]. Although the conductivity of conjugated polymers can be varied through electrochemical reduction and oxidation, the conductance will be highly dependent on the morphology of polymer film formed. Generally speaking, the more ordered the polymer chains are, the higher the conductance of film. This degree of order can be varied by changing counter-ion dopant, synthesis parameters (time, temperature, solvent), and processing method. The p-type conjugated polymers are most widely studied as they can be easily synthesized through oxidative polymerization in the presence of an appropriate counterion to act as the dopant.

These polymers have been widely tested in Li-ion type batteries as standalone cathode materials with moderate specific capacities[96,97], or as additives/coatings to help prevent particle fracture due to volume expansion or dissolution of active materials[26,63,93,99,100]. More recently some groups have demonstrated their use in aqueous rechargeable lithium batteries. Liu et al. showed that coating α-MoO$_3$ with polypyrrole vastly improved the cycling stability of the material by preventing the dissolution of molybdenum ions[26,45]. In addition, although the PPy coating would be expected to be in the neutral state at the redox potentials of α-MoO$_3$ and thusly provide no enhancement of electronic conductivity, a decrease in charge transfer resistance was reported but no potential mechanism was offered. Similarly, Tang et al. showed that coating a composite of V$_2$O$_5$ and multi-walled carbon nanotubes with polypyrrole improved the cycling performance of the material by preventing the dissolution of vanadium ions[94]. Although only the increased cycling stability and lack of change in electrolyte color were given as reasons for supporting the conclusion that vanadium ions were not solvated in the electrolyte. Therefore, we propose coating of NaTi$_2$(PO$_4$)$_3$ with polypyrrole will improve the cycling stability of the material by preventing unwanted side reactions with the electrolyte. It should be noted that, similar to the case of α-MoO$_3$, the low redox potential (-1.25V vs. Hg/Hg$_2$SO$_4$) of NaTi$_2$(PO$_4$)$_3$ implies that the polypyrrole coating will be in its fully reduced state and provide no enhancement of the electronic conductivity. However, given a sufficiently thin coating, electron transport should still be possible.

6.2 Experimental

6.2.1 Materials Synthesis

All chemicals used were of reagent grade. In a typical synthesis, 0.71 g Na_2HPO_4, was dissolved in a solution of 10 mL deionized H_2O containing 2.88 g of 85 wt % aqueous H_3PO_4. Under vigorous stirring 1.60 g of TiO_2 (21 nm Sigma Aldrich) was slowly added to the mixture. This mixture was then heated, until enough water had evaporated that a thick paste was formed. This paste was then decomposed at 500°C for 3h before being placed in a furnace at 1000°C for 6h. The as-formed material was lightly ground in a mortar and pestle before use. This material, $NaTi_2(PO_4)_3$, is referred to as NTP.

Reagent-grade pyrrole (Py) and 4-dodecylbenzenesulfonic acid (>95%) (DBSA) were purchased from Sigma-Aldrich and used without further purification. To produce the polypyrrole doped with DBSA (PPy-DBSA), 0.588 g (1.8 mmol) of DBSA was dissolved in 6 mL of distilled water at 25°C under vigorous stirring. Then 250 μL (3.6 mmol) of Py was added and dissolved into the solution. The reaction was cooled in an ice water bath for several minutes. The oxidant solution was prepared by dissolving 0.164 g (0.72 mmol) ammonium persulfate (APS) in 1.2 mL distilled water before being added drop-wise to the monomer solution. The reaction was warmed to 25°C and was left stirring for 48 hours. The mixture was transferred to a 50 mL centrifuge tube, filled to the top with distilled water, and centrifuged at 4400 rpm on an Eppendorf Centrifuge 5702 R for approximately 15 minutes. The supernatant was then decanted and the process repeated twice more with water and twice with methanol. Afterwards, the product was left to dry in a fume hood for two days, redispersed in water, sonicated, and then washed with water over a Buchner funnel under vacuum.

6.2.2 Materials Characterization

For galvanostatic cycling with potential limitation (GCPL) a sodium manganese oxide cathode consisting of $Na_{0.55}MnO_2$ (NMO) was prepared. This was used as a sodium containing cathode material, and has been shown to be stable through hundreds of cycles in neutral aqueous electrolytes[33]. Stoichiometric amounts of Na_2CO_3 and Mn_2O_3 (~7 g total) were milled for 30mins in a SPEX 8000M high-energy ball mill using a Si_3N_4 canister with one grinding bead. This mixture was then place in a box furnace under ambient air conditions and heated to 800°C followed by a 12 hr soak before being cooled to 25°C.

X-ray powder diffraction using a PANalytical X'Pert Pro MPD with a CuK_α source and a nickel filter was used to characterize the crystal structure of the tested materials. A scan range of 10-60° 2θ was used for all scans. The morphology was examined by SEM and TEM imaging using a Philips XL-30 scanning electron microscope and a JEOL-2000EX transmission electron microscope.

For comparison, an electrode composite was prepared containing 80wt% NTP, 10wt% carbon black (CB), and 10wt% polyvinylidene fluoride (PVDF). Briefly, an appropriate amount of NTP was ball milled with the carbon black in a SPEX 8000M for 30 minutes. This was then mixed with the CB in a mortar and pestle, before N-methylpyrrolidone (NMP) was added to the mixture and ground until a uniform thick paste was formed. This paste was dried in a vacuum oven at 80°C overnight before being granulated over an 80 mesh stainless steel screen. This material will be referred to as NTP-C.

The composite of NTP and PPy-DBSA was made through a high-energy ball milling process. Previous results within the group have shown this to be a reliable method for coating hard ceramics with polymers. Two composites were tested, one containing a weight ratio of NTP to PPy-DBSA of 80:20 and another containing ratio of 95:5, these ratios would produce an idealized coating between 5-25 nm in thickness. To form these composites an appropriate amount of NTP and PPy-DBSA were added to a Si_3N_4 milling canister and milled for 30 minutes. After removing the powder, a mixture of 80wt% NTP-PPy (either 80:20 or 95:5 ratio), 10wt% CB, and 10wt% PVDF were mixed in a mortar and pestle containing NMP until a smooth thick paste was formed. This mixture was then dried and granulated in the same manner as the control. These mixtures will be referred to as NTP-PPy-8020 and NTP-PPY-955 for the 80:20 and 95:5 ratio respectively.

A Bio-Logic VMP3 was used for all electrochemical tests. Cyclic voltammetry (CV) was used to characterize the produced composites between -1.5 V and -0.5 V vs. Hg/Hg_2SO_4 and between -1.5 V and 0 V for the as produced PPy-DBSA. Samples for testing were prepared by pressing about 2 mg of the material into a 50-mesh stainless steel screen, with a sample area of about 0.25 cm^2. The sample was then cycled in a three electrode set up containing 1M Na_2SO_4 made with 18.2 MOhm deionized water with platinum wire as a counter electrode and a Hg/Hg_2SO_4 in saturated K_2SO_4 as a reference electrode. In order to test for changes in conductivity upon cycling electrochemical impedance spectroscopy (EIS) was carried out in conjunction with a cyclic voltammetry experiment. The same experimental cell was used as previously described. The test procedure consisted of a single CV scan at 0.50 mV/s between -0.5 V and -1.5 V vs.

Hg/Hg$_2$SO$_4$ in 1M Na$_2$SO$_4$ followed by EIS under potential control at the end of oxidation. This procedure was repeated for 50 total cycles. A scan range of 100 kHz to 100 mHz with a 5 mV amplitude was used. The sampling frequency was 10 points per decade with 3 measures per frequency and a 0.1 second wait between measurements.

Three electrode Swagelok cells with stainless steel rods as current collectors were used for GCPL testing, with voltage limits of the NTP being set at -1.0 V and -1.4 V at a C/5 rate (based on initial discharge times). In these cells the NTP-containing composites were used as an anode and an NMO-containing composite, prepared in the same manner as the other electrode materials, was used as a cathode. The anode was prepared by pressing a 35 mg pellet of composite material in a 10 mm die set at 3 tonnes on a Carver Model C Laboratory Press. The cathode was prepared by pressing 300 mg of the NMO composite in a 15 mm die set at 3 tonnes. An Hg/Hg$_2$SO$_4$ in saturated K$_2$SO$_4$ reference electrode was used. The difference in mass and area between the anode and cathode ensured that the limiting electrode would always be the anode, so any loss in functionality at the cathode due to cycling would be minimal. Only the NTP charge-discharge curves are presented in this work. Figure 3.1 shows the experimental cells used for testing.

6.3 Results/Discussion

SEM of the prepared raw materials are shown in Figure 6.1. NTP shows a relatively isometric morphology with an average particle size of 270 nm. There are two different morphologies present in the PPy-DBSA: a larger primary particle on the order of 20-100 μm with a glassy

morphology and relatively smooth fracture surfaces, and smaller, isometric secondary particles interspersed with a particle size of around 0.1-3 μm.
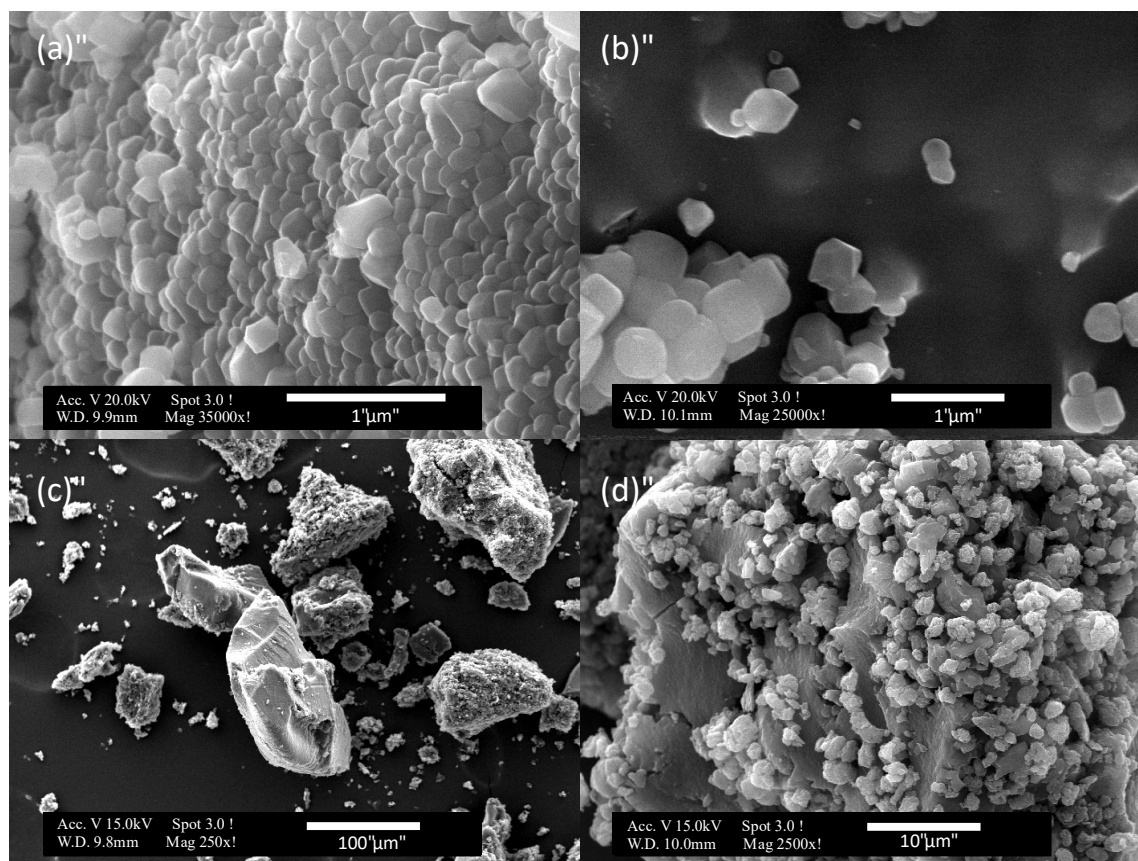
Figure 6.1 Scanning electron microscope images of the as produced (a,b) NTP and (c,d) PPy-DBSA.

For the composites NTP-PPy-8020 and NTP-PPy-955, assuming spherical particles and densities of 2.8 g/cm^3 and 1.8 g/cm^3 for NTP and PPy-DBSA respectively, the predicted thickness of coatings is ~23 nm and ~8 nm. SEM of the composites (Fig. 6.2a, b) shows the NTP to be relatively tightly bound into dense agglomerates. It is also apparent that the high-energy ball milling process did not entirely coat the NTP particles, with some sharp facets of the particles still clearly visible. Inspection of particle surfaces using TEM (Fig. 6.2c, d) shows the polymeric coatings, with thicknesses close to that predicted from the particle sizes. It is evident from these

coatings that the high-energy ball milling process is a reliable method for coating NTP particles with PPy-DBSA.
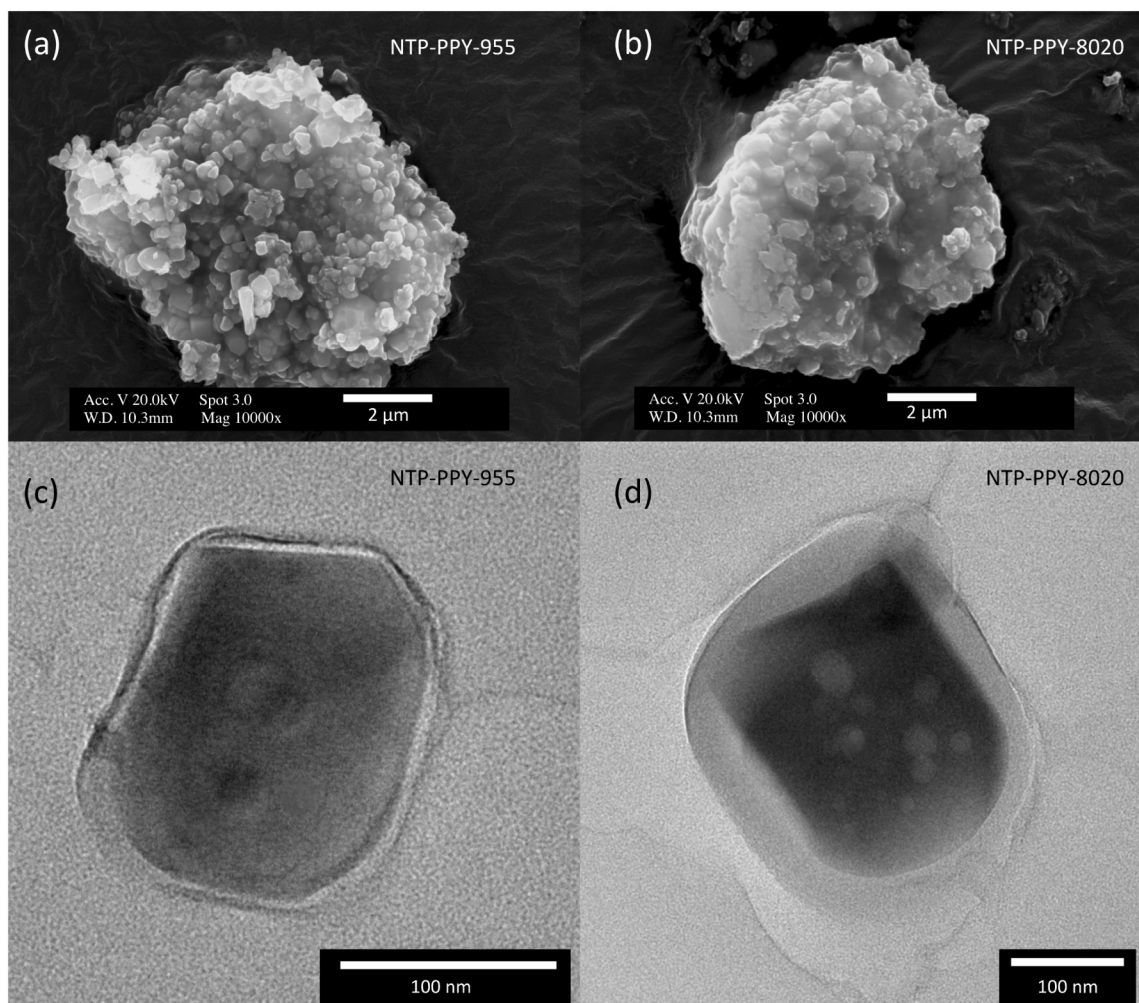
Figure 6.2 SEM and TEM images of the PPY-DBSA containing composites (a,c) NTP-PPy-955 and (b,d) NTP-PPy-8020

SEM of the prepared electrodes' microstructures, both before and after cycling, can be found in Fig 6.3. The prepared NTP-C electrode shows a markedly different microstructure than the NTP-PPy-955, with large, smooth surfaced particles being present in the composite. This difference in agglomerate structure with in the prepared electrodes indicates a relatively better coating of NTP in the NTP-PPy-955 composite. After cycling there is no apparent difference in the NTP-PPy-955 material. However, for the NTP-C electrode, the once smooth surfaces now show a

roughened surface texture. The nature of this texturing is not known, though it could indicate a dissolution and precipitation type mechanism being present. It could also be residual PVDF binder that has had the embedded carbon particles corroded away.
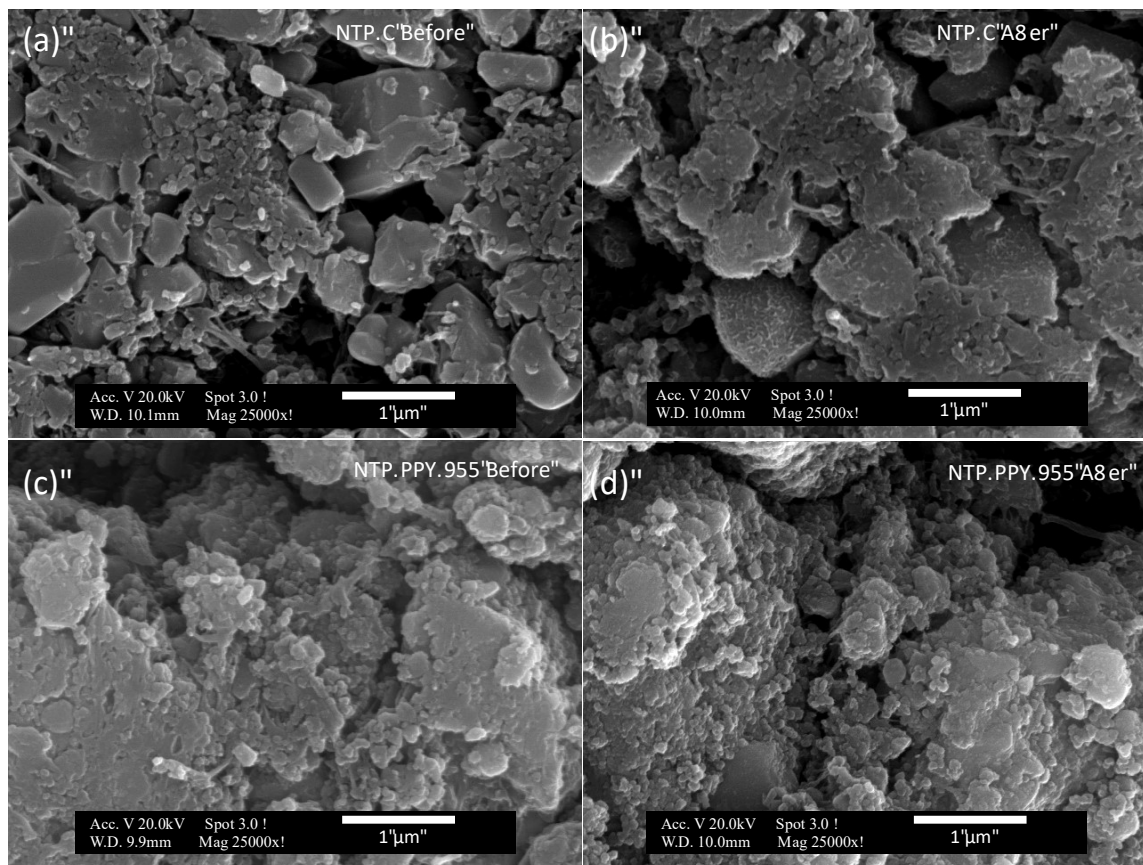
Figure 6.3 SEM images of the prepared electrodes' microstructure (a,b) NTP-C and (c,d) NTP-PPy-955, both before and after cycling.

X-ray diffraction patterns of the NTP contain composites and PPY-DBSA can be found in Figure 6.4. The raw NTP shows no presence of crystalline impurity phases and assuming a R$\bar{3}$c crystal structure has calculated lattice parameters of a=b=c=8.76 Å and α=β=γ=57.95°, in good agreement with JCPDS 85-2265. PPy-DBSA shows a low intensity, broad peak around 20° 2θ, indicative of an amorphous type structure. This peak can be deconvolved into two peaks centered at 19.6° and 25.5° 2θ, in good agreement with previously reported values of 20° and 26° that

have been attributed to the pyrrole-counter ion and pyrrole-pyrrole interaction scattering[101].

X-ray diffraction patterns of the composites NTP-PPy-955 and NTP-PPy-8020, prior to the

addition of carbon black and PVDF, show the same pattern as the NTP, but with decreased peak

intensity, as would be expected from the presence of an amorphous coating.
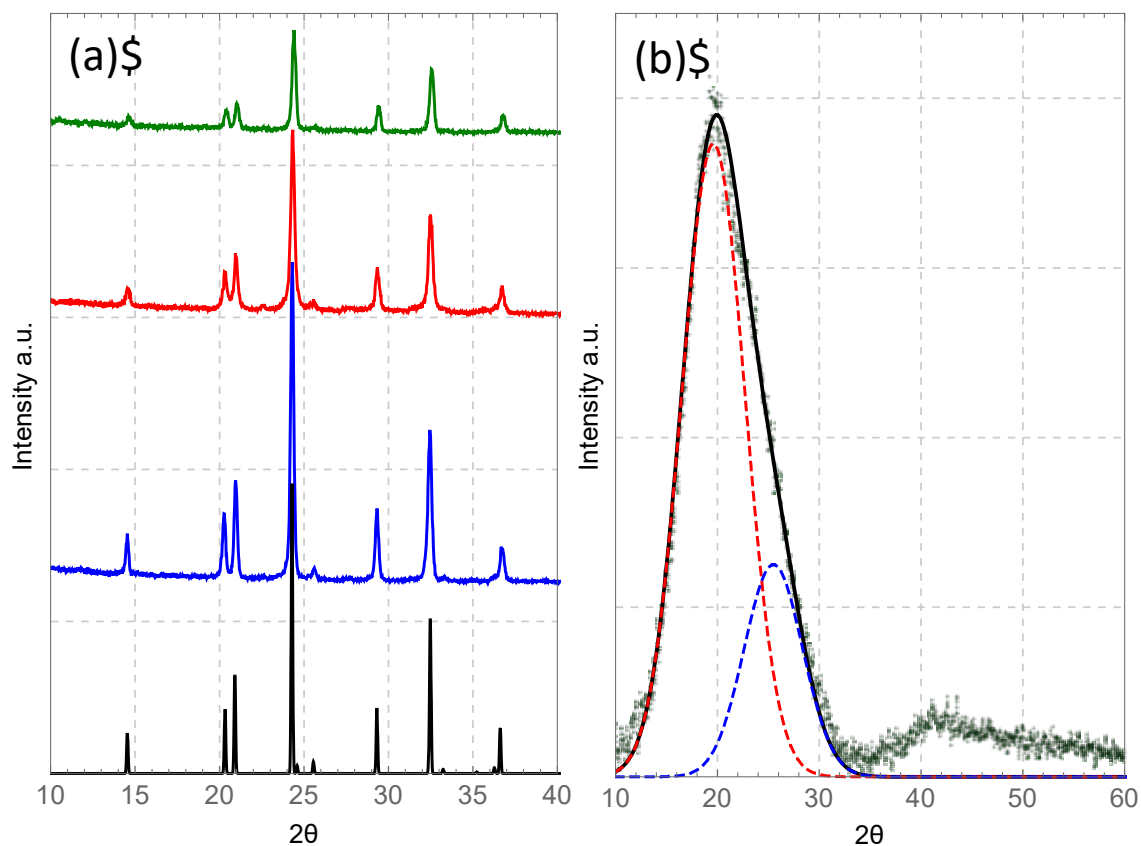
Figure 6.4 X-ray diffraction patterns of (a) NTP (blue), NTP-PPy-955 (red), NTP-PPy-8020 (green), and JCPDS 85-2265 (black) and (b) PPy-DBSA (green) showing the deconvolution of the primary peak into two separate peaks at 19.5° (red) and 25.5° (blue).

Electrochemical characterization of PPy-DBSA (Figure 6.5) shows a moderate specific discharge

capacity of ~28 mAh/g, with some hysteresis between the charge and discharge processes. This

hysteresis is clearly visible in the inset of Figure 6.6b, with the discharge curves showing a sharp

inflection at the start of discharge that is not present during the end of the charge curve. This

hysteresis has been attributed to variation in the conductivity upon oxidation/reduction and the

lag between the current flow and relatively slow ion-exchange process. It is also clear from the

98

Coulombic efficiency that there exists a relatively long break-in period, in which the PPy-DBSA experiences some form of a side reaction that consumes charge. This side reaction dissipates and is no longer present by about the 50th cycle. This charge consumption could be caused by some electrochemically unstable regions of the polymer reacting with the electrolyte due to the applied current. Further investigation is needed to elucidate the precise nature of this charge consumption.
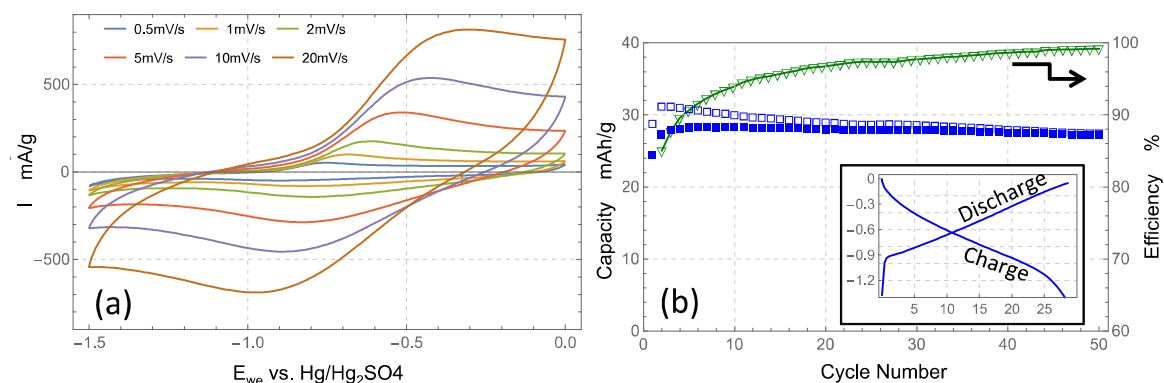
Figure 6.5 Cyclic voltammetry (a) of PPy-DBSA. Cycling performance and Coulombic efficiency of PPy-DBSA at a C/5 rate (b). The inset shows the charge-discharge curves of the PPY-DBSA as a function of specific capacity.

Cyclic voltammograms of the composite materials and the control can be found in Figure 6.6 and Figure 6.7 in which only the fifth cycle for each of the scans from 0.5-20 mV/s have been presented. Cyclic voltammetry of the NTP-PPy-8020 in 1M Na_2SO_4 (Figure 6.6a) indicates that if the coating of PPy is too thick, sodium ion diffusion into the NTP is completely absent at the redox potential of NTP. This manifests as a visible capacity from the PPy-DBSA coating but no visible redox peaks from the NTP even though it is the dominant component of the composite. This finding is somewhat contradictory to potassium and lithium ion diffusion in previously reported polypyrrole coatings of thicknesses 10-20 nm and 10-12 nm on α-MoO_3 and V_2O_5 respectively[26,93]. NTP is known to undergo redox reactions with lithium similar to those with sodium[102], and thus should still present a redox peak if Li^+ is capable of diffusing through the

coating. However, no redox peaks for NTP are seen (Figure 6.6b). Potassium sulfate was not

tested with the composite material since NTP is not known to undergo redox reactions with K^+.
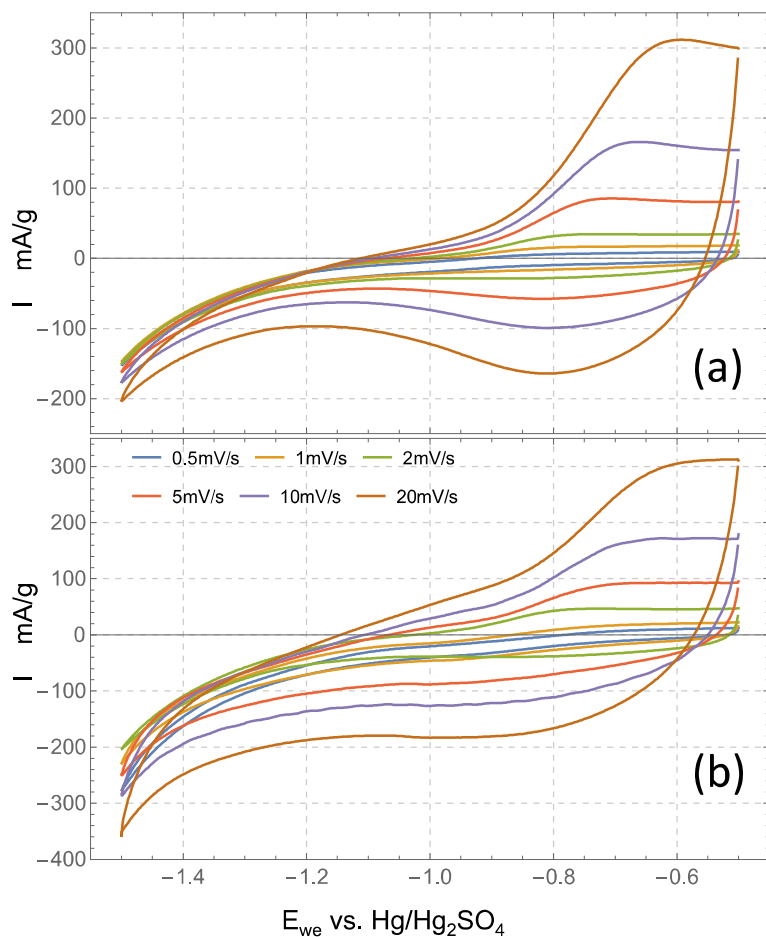
Figure 6.6 Cyclic Voltammetry results for the NTP-PPy-8020 composites cycled in (a) 1 M Na_2SO_4 and (b) 1 M Li_2SO_4.

The results of the CV indicate that the difference is not a function of the electrolyte cation in this

case. It is possible that this poor ionic transport is a function of the synthesis process, method of

compositing the polymer with the active material, overall thickness of the coating, or some

combination thereof. It is clear from comparing the CV curves of NTP-PPy-8020 (Figure 6.6a)

and NTP-PPy-955 (Figure 6.7b) that somewhere between 8-23 nm of coating, cationic transport

through the PPy-DBSA incorporated through milling becomes too limiting for efficient energy

storage.
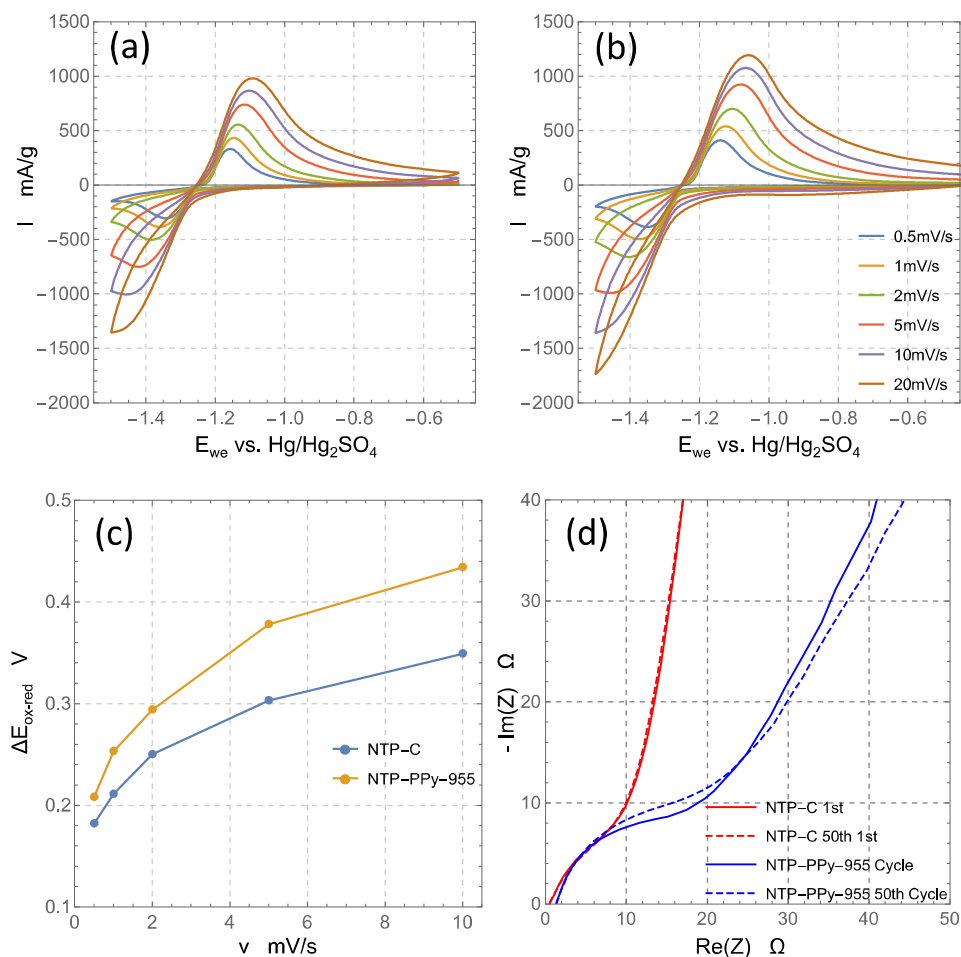
Figure 6.7 Cyclic voltammetry results of (a) NTP-C and (b) NTP-PPy-955, (c) the potential separation between the reduction and oxidation peaks as a function of scan rate for these composites, and (d) EIS of these materials after 1 and after 50 cycles.

This is not to be wholly unexpected, as the nature of the redox reaction in these polymers, when doped with relatively mobile anions, involves removal and insertion of these anions and in some cases solvent molecules, but not cations[96,103]. Polypyrrole in its neutral, or fully reduced state is also known to have poor ionic and electronic transport properties[104,105]. Previous reports of coating anode materials with PPy have used in-situ synthesis of the polymer in the presence of the active material; the authors attempted in situ synthesis, but it appeared that the synthesized PPy did not readily adhere to the NTP surface. This manifested as visible phase separation during the centrifuging process, with a layer of white uncoated NTP, and a layer of black PPy or

PPy coated NTP. Because of this, the results of this material have not been presented here. Further investigation will be needed to promote adhesion of PPy to the NTP surface.

EIS results after one cycle and after fifty cycles can be found in Figure 6.7d. The high frequency response indicates that both NTP-C and NTP-PPy-955 have similar electronic resistances of 0.8 Ohm and 1.2Ohm respectively. Since this electronic resistance is a combination of the apparatus resistance, electrode resistance, and DC ionic resistance of the electrolyte, the difference may be a result of small differences in apparatus set up or electrode placement with respect to the reference electrode. In particular since no change in the high frequency intercept is seen after 50 cycles, it would appear that the electronic resistance of the composite is negligible compared to the electrolyte resistance. Since the spectra were taken at a potential of -0.5V vs. Hg/Hg_2SO_4, a potential at which the PPy-DBSA coating will be electrochemically active (seen as a noticeably different charge transfer response in the medium frequency range), comparison of the medium and high frequencies is not straight forward. Though it is clear that the response of the NTP-C electrode material remains almost unchanged over the fifty cycles. The NTP-PPy-955 shows a small change after fifty cycles, with a slight decrease in the slope of the low frequency response.

Comparing the cyclic voltammetry results of the NTP-PPy-955 to the control of NTP-C, we see quite similar performances (Figure 6.7a,b). However, analysis of the difference between reduction and oxidation peak potentials (Figure 6.7c) shows that the NTP-PPy-955 is more rate-limited, as the peaks separate more quickly upon increasing the scan rate. However, given the intended use of grid-scale energy storage, where relatively long charge/discharge times are expected, this rate-limiting aspect of the coating should be of little significance.

Charge-discharge curves of the first and 50th cycle of both NTP-C and NTP-PPy-955 are shown

in Figure 6.8a, and specific capacity and efficiency as a function of cycle number are found in

Figure 6.8b. The control, NTP-C, shows an initial charge capacity of 89 mAh/g, normalized to

the mass of active material, whereas the NTP-PPy-955 shows a capacity of 104 mAh/g

normalized to the mass of NTP and PPy in the composites, the bulk of which is delivered in

between -1.2 and -1.3V vs. MSE. The reason for this increased charge capacity on the first cycle

is not readily apparent and cannot be account for by the added 5 wt % of PPy-DBSA. Both

composites delivered similar initial discharge capacities of 65 and 68 mAh/g. The initial

Coulombic efficiency of the control is higher at 73% versus the PPy-DBSA containing

composites initial efficiency of 65% and remains more efficient for the first 15 cycles, after

which efficiencies are roughly equivalent at ~98%. This lower initial efficiency of the NTP-PPY-

955 can be accounted for by considering the long break-in time for the PPy-DBSA coating on the

material, which undergoes some electron consuming side reaction that persists for many cycles.
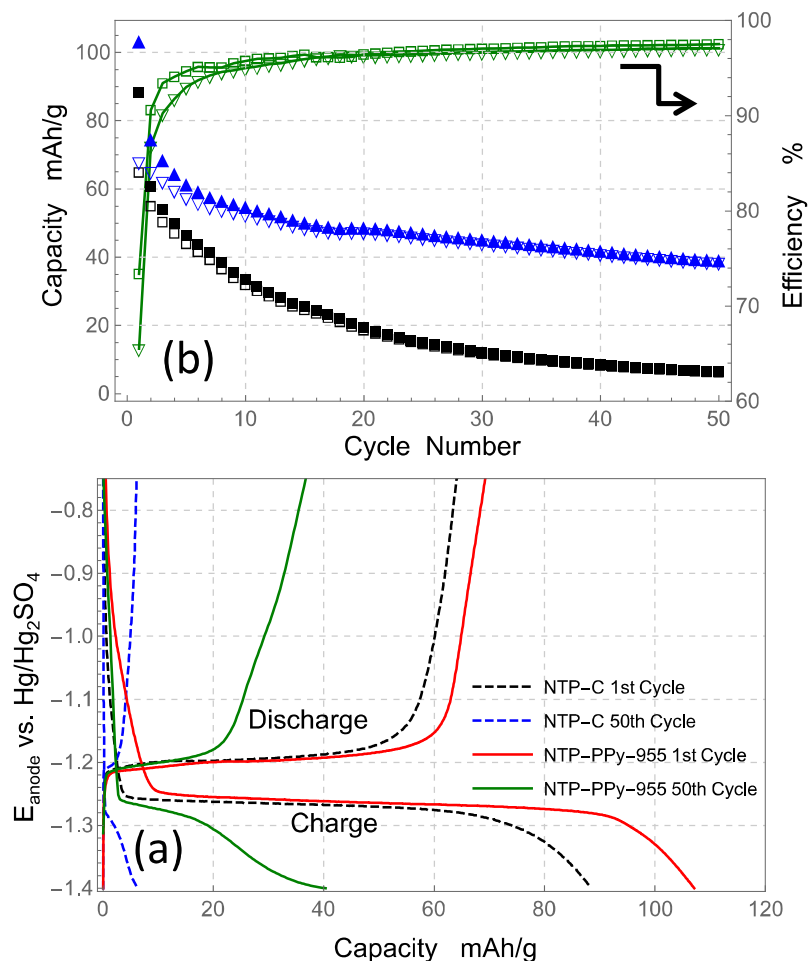
Figure 6.8 Charge-discharge curves for the 1st and 50th cycles of the NTP-C and NTP-PPy-995. (b) Cycling performance of NTP-C (black squares) and NTP-PPy-955 (blue triangles) and their corresponding efficiency.

Taking a closer look at the charge-discharge curves in Figure 6.8a we see the expected long plateau of NTP centered at -1.25V, typical of a two-phase redox reaction. It is also apparent that the voltage separation between the initial charge and discharge plateaus is smaller for NTP-PPY-955 than NTP-C. This would seem to contradict the CV results that show the NTP-PPYy-955 to have slower kinetics. However, given the GCPL was carried out at a C/5 rate, which is relatively slow, the overpotentials associated with higher rates may not be appreciable. This smaller separation may then be a consequence of a smaller charge transfer resistance, as was reported for polypyrrole coatings on α-MoO$_3$[45].

The composite containing polypyrrole also showed considerably better cycling performance when compared to NTP-C. By the 10th cycle NTP-C has lost 50% of its initial discharge capacity compared to NTP-PPy-955 having lost only 23%. After 50 cycles the control has lost 90% of its discharge capacity and NTP-PPy-955 has lost only 43%. Although the specific capacity is somewhat lower than previous works, the cycle stability is notable when compared to previous results of NTP that has been cycled at low rates. The NTP-C shows a similar percentage decrease in capacity when compared to a similar electrode tested by Li et al. with 80wt% NTP, carbon nanotubes, and a PTFE binder and cycled in neutral 1M Na_2SO_4[46]. There, the material's discharge capacity was found to fade to ~17% of its initial discharge capacity in 50 cycles. Though in this study both of the electrode materials still fade considerably upon cycling, the PPy coated composite fades at a significantly slower rate. It is possible that this improvement can be much more profound if a more complete and well distributed coating were to be achieved, since our data indicate that the current coating is not completely consistent and, as such, may be limiting.

The ultimate cause of capacity loss in this materials system is still not completely understood, however these results suggest that the effect can be diminished by protecting the NTP surface from the electrolyte environment. It also remains to be seen if optimizing the coating composition and conditions can result in even more improvement; work is ongoing to both understand the capacity loss phenomenon more completely as well as to generate a more complete/optimal coating solution based on the compelling preliminary results presented here.

6.4 Conclusion

In this work we have tested the feasibility of using polypyrrole as a coating for $NaTi_2(PO_4)_3$

anodes. Although the coated material shows considerable improvement in cyclability, the poor

sodium and lithium ion diffusion of PPy doped with DBSA at potentials below -0.9V vs.

Hg/Hg_2SO_4 limits the thickness of the coating that can be used. With the upper limit in thickness

that still allows for sodium ion diffusion lying somewhere between 10-20 nm, it may not be

possible to fully prevent interactions with the electrolyte using this particular form of

polypyrrole. Although at the redox potentials for $NaTi_2(PO_4)_3$ polypyrrole is almost fully

reduced and as such should not be electronically conducting, it appears to have a negligible

effect on the overall performance of the electrode material. Given the relatively pore adhesion

observed when attempting in situ polymerization of PPy in the presence of NTP, another method

for coating was considered. This will be discussed in the next chapter.

Chapter 7: Polydopamine Derived Coatings

7.1 Overview

Testing of the PPy coated NTP indicated that although the PPy improved the cycling stability compared to the uncoated material, significant capacity fade was still a problem. Furthermore, it is clear from the voltage vs capacity curves of the PPy coated NTP that dissolution was still an issue, as evidenced by the secondary reduction plateau during GCPL tests. This plateau was observed in Chapter 4 when NTP had been directly exposed to high pH solution. In hindsight, this poor coverage of PPy on NTP is not too surprising. Attempts to produce a conformal coating on NTP via in-situ oxidative polymerization proved difficult indicating unfavorable adhesion between the NTP surface and PPy, and so it is likely that even though the ball milling process managed to coat a large fraction of the particles, the unfavorable surface adhesion between the two materials prevented complete coverage. In order to get around this problem we turned to in-situ polymerization of polydopamine (PD) to produce conformal coatings that allow for further carbonization.

Polydopamine has been shown to be able to adhere to most surfaces through both covalent and non-covalent bonding mechanisms, including: hydrogen bonding, chelation, and π-π stacking. In particular, for metal oxide surfaces, the formation of coordination complexes with the metal are believed to be the primary mechanism of adhesion. Because of this some groups have used PD adhesion layers as precursors for nitrogen doped carbon coatings on battery electrode materials such as Fe_2O_3. For our purposes, the demonstrated proficiency of PD to adhere to TiO_2 surfaces is particularly interesting. Given that NTP consists of a network of PO_4 tetrahedra and TiO_6 octahedra, and polymerization of dopamine-HCl to PD occurs in slightly basic conditions, where

we expect some loss of surface phosphate but not loss of TiO_6, we should expect that polymerization of PD in the presence of NTP will lead to adhesion similar to that between PD and TiO_2.

7.2 Experimental

7.2.1 Materials synthesis

NTP produced from the solvothermal method describe in Chapter 3.2 was used for this experiment. A tris buffer solution was prepared by adding 1.21g of Tris to 90 mL of deionized water, then titrated to pH 8.5 using 1M HCl followed by the addition of deionized water to reach 100 mL total volume. A solution of dopamine was prepared by dissolving 75mg of dopamine hydrochloride into 5 mL of deionized water. Next, 500 mg of NTP particles were dispersed in 20 mL of Tris buffer (pH 8.5), then placed in an ultrasonic bath for 30 minutes to ensure a homogenous dispersion. The 5 mL of dopamine solution was then added drop wise to the NTP dispersion under moderate mixing. The final concentration of dopamine in solution was 3 mg/mL. Upon addition of the dopamine solution the color rapidly changed from a pure white to a yellowish-orange solution, followed by a slow transition to brown, and then gray. The mixture was allowed to stir for 24 hours. The PD coated NTP was collected by centrifuging, decanting, then dispersing in deionized water. This process was carried out four times, after which the sample tubes were placed in an oven at 80 °C overnight. The collected powder was brown in color. Half of the dried powder was then used to produce a carbon coated NTP sample (NTP-C), while the other half was used as in the uncarbonized form (NTP-PD). To produce the carbon coated sample, the powder was placed in an alumina crucible and then into a tube furnace, where it was heated at 2 °C/min to 300 °C, held for 2 hours, and then ramped to 550 °C at 5 °C/min,

and held for 6 hours before being allowed to cool to room temperature. The final product, NTP-C, was dark gray in appearance.

Electrodes were prepared by combining the coated NTP samples with carbon black and PVDF in a mortar and pestle. A mass ratio of 70:20:10 was used. After thorough mixing of the dry powder, enough NMP was added to the mortar to produce a thick paste. This paste was mixed thoroughly and allowed to smear out into a relatively even coating inside of the mortar. The mortar and pestle were then placed in an oven at 80 °C and allowed to dry overnight. The final product was scraped from the inside of the mortar before being granulated through a stainless-steel mesh screen. After granulation, 40 mg of the electrode granulate was placed into a 10 mm diameter steel pellet press and pressed to 3 metric tonnes. The electrode pellet was then cut into square sections of approximately equal size using a razor blade, after which each section was placed between a bent piece of stainless steel mesh and pressed to 6 metric tonnes to form the electrode current collector sample for testing.

7.2.2 Electrochemical Testing

Cyclic voltammetry was performed on three samples of each electrode in a voltage range of -1.5 to -0.5 V versus mercury sulfate. Each electrode underwent 11 cyclic voltammetry cycles at 10, 5, 2.5, 1, and 0.5 mV/s, before being place on extended cycling at 1 mV/s. The electrode set up was the same as described in other chapters and consisted of a platinum wire reference electrode, a mercury sulfate in saturated potassium sulfate reference electrode, and a glass or plastic beaker filled with electrolyte.

7.3 Results

Figure 7.1 shows the specific capacity as a function of cycle number for both coated samples and a control. The control electrode containing uncoated NTP shows a higher initial capacity than the NTP-C containing electrode, which in turn shows a higher initial capacity then the NTP-PD electrode. This is most likely due to the way in which the samples were weighed, since the normalization of capacity by mass of NTP-C and NTP-PD does not account for the mass fraction carbon or polydopamine. The actual mass of carbon and polydopamine in these samples is unknown, however. Comparing the capacities of the coated versus uncoated materials we see that the coated materials show an increase in specific capacity for the first several cycles whereas the control shows an immediate loss of capacity upon cycling. This could be due to a difference in the rate of deactivation of active material versus the rate of wetting of the electrode. In this case deactivation refers to any mechanism that leads to active material not being electrochemically accessible, whether it is due to dissolution of material, physical separation of material, or loss of ECSA due to gas occlusion of the pore network. In NTP-C and NTP-PD the total amount of material undergoing deactivation is lower than the rate of material activation that occurs as the electrodes pore network becomes fully wetted. This leads to a net increase in capacity over the first several cycles until the electrode has become fully wetted. The control sample, on the other hand, has material being deactivated at a rate faster than the rate at which material is becoming accessible to infiltration. If we also consider the stability of the capacity decay versus time, the controls rate of capacity fade is considerably noisier. Such instability can be attributed to the nature of gas generation, entrapment, and exclusion from the pores, which

leads to sudden losses/gains in surface area within the electrode. As a consequence, the total

accessible material can change suddenly between cycles.
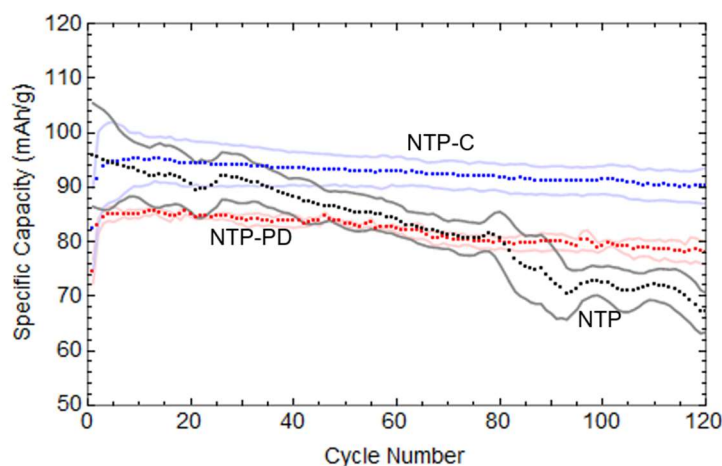
Figure 7.1 Specific capacity versus cycle number for the uncoated material, NTP (black), polydopamine coated material, NTP-PD (red), and the carbon coated material, NTP-C (blue). Mean values from three samples are shown as dotted lines and ± 1 standard deviation is shown as a solid but lighter colored line.

The rate of capacity fade is considerably lower for NTP-C and NTP-PD than for the control

samples. If the rate of capacity fade over the collected cycles is considered to be linear, then the

control sample shows a rate of capacity fade 3.6x larger than the rate of fade of NTP-PD, which

is 1.3x larger than the rate of fade of NTP-C. By coating the NTP particles with a layer of

polydopamine derived carbon the relative cycle life (under the assumption of linear capacity

fade) of the electrode increases by almost 5-fold.

Another interesting difference between the electrodes is the standard deviation of the capacities

for the three samples. The sample containing polydopamine coated material had a narrower

distribution of capacities than the carbon coated sample, which in turn had a narrower

distribution than the uncoated sample. This difference in the standard deviations of capacity is

not currently understood. It was also noted that jumps/drops in capacity for the control sample

were correlated between the samples leading to a smaller standard deviation than expected. This

phenomenon, we believe, is related to physical disturbance of the table the cells were being cycled on. It was observed that the uncoated control electrodes showed a large number of bubbles nucleating with in the cell (either on the surface of the electrode, or on the reference electrode tip). When the table the cells were resting on was bumped, bubbles would be released from certain surfaces, and on other surfaces bubbles would coalesce into a single larger bubble. This could lead to correlated capacity jumps between samples that were being cycled at the same time.

The shapes of the CV curves collected for the different samples show notable differences (Figure 7.2). The control material, showed a relatively broad oxidation peak compared to the other two samples, as well as an almost 50 mV shift of the peak current. This shift of the peak current to lower potentials during reduction and higher potentials during oxidation indicates that the uncoated material should be more rate limited than the coated materials, though this hypothesis has not currently been tested.

 A secondary reduction peak is present on the NTP-PD sample, that develops with increasing cycles before stabilizing. This peak was not observed in the voltammetry curves of either of the other samples and may be related to redox processes occurring within the polydopamine coating. Furthermore, the change in oxidative overpotentials during cycling experienced by the electrodes appear to be different. Looking at figure 7.2b (NTP-C), the oxidative current at potentials > -1 V increases with increasing cycle number and is indicative of some of the electrodes capacity not being accessible until higher potentials are reached. In comparison, the NTP-PD sample shows an almost negligible increase during cycling of the oxidative current at higher potentials. The nature of this difference in overpotentials is currently unknown.
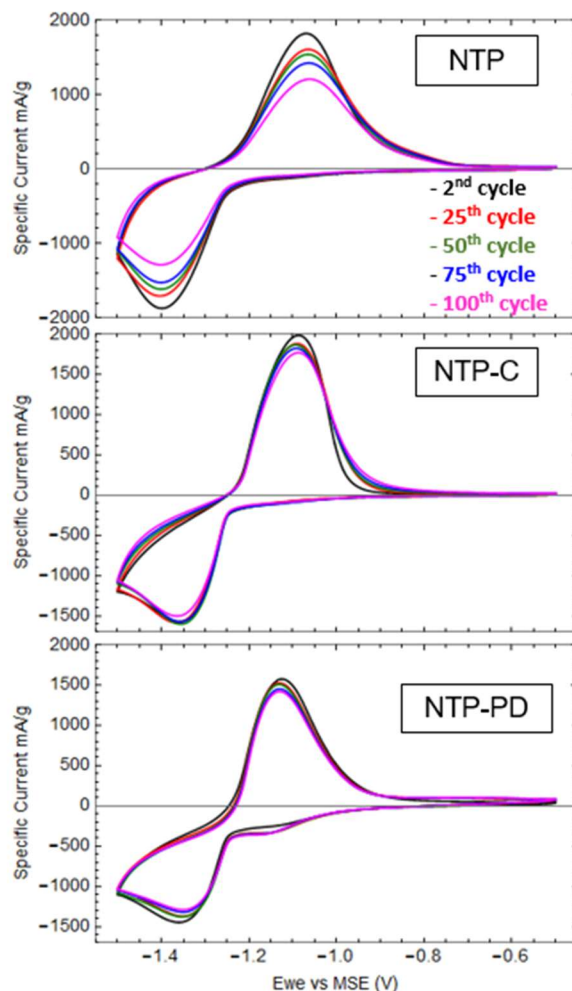
Figure 7.2 Cyclic voltammetry curves for (a) uncoated NTP, (b) carbon coated NTP, and (c) polydopamine coated NTP. The 2nd, 25th, 50th, 75th, and 100th cycles are shown.

Figure 7.3 shows results from the cyclic voltammetry performed at varying rates. From the voltammetry curves in Fig 7.3a-c, it is clear that the polydopamine coating greatly reduces the electrochemical performance of NTP at high rates. This is clearer when comparing the peak current versus square root of the scan rate for the different samples (Fig 7.3d); the NTP-PD deviates from the expected linear relationship much more than the other two samples. Remarkably, NTP-PD shows better performance than the NTP control at slow rates, with the

specific discharge capacity being comparable to the control, NTP, at 1 mV/s but 10 mAh/g higher at 0.5 mV/s (Fig 7.3e).
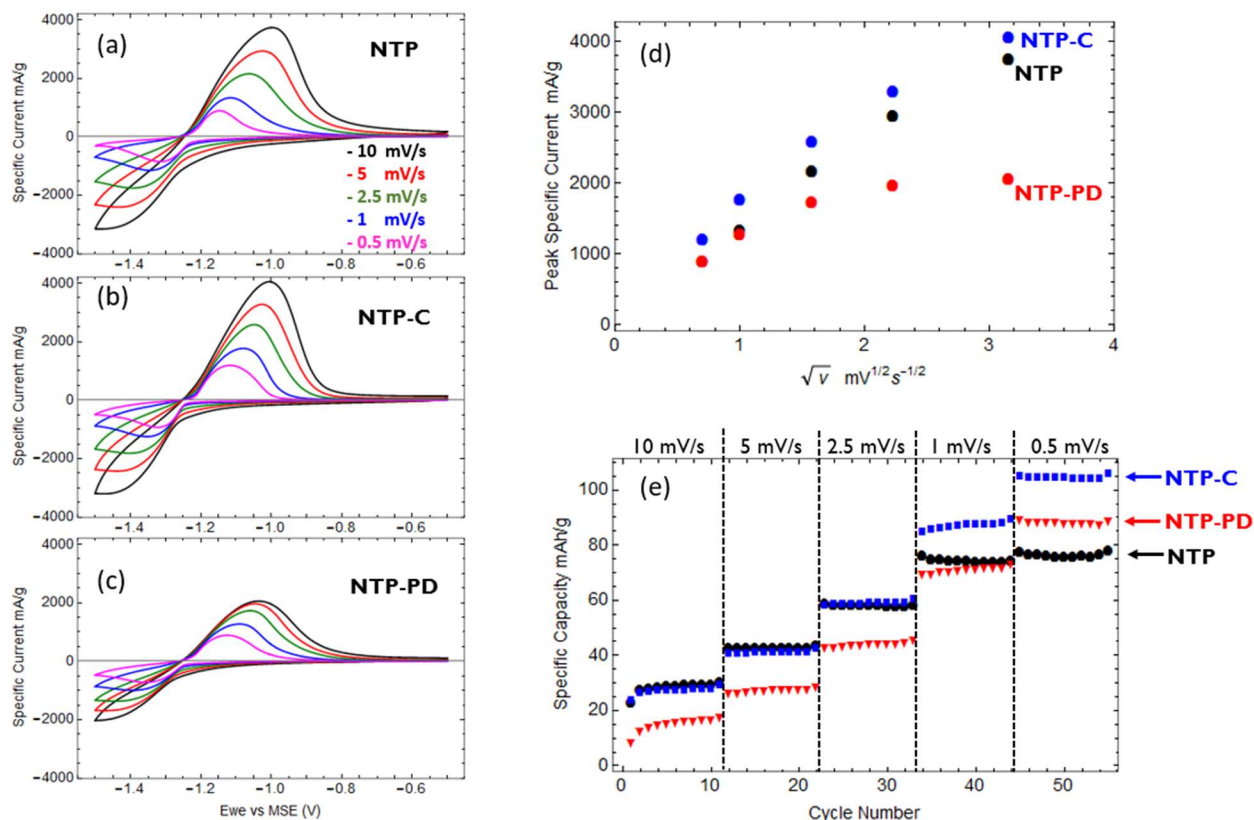
Figure 7.3 Results for cyclic voltammetry performed at 0.5, 1, 2.5, 5, and 10 mV/s on each of the samples. (a-c) Cyclic voltammetry curves of the tenth scan at each of the different rates, (a) NTP, (b) NTP-C, and (c) NTP-PD. (d) The peak specific current for oxidation as a function of the square root of the scan rate. (e) Specific capacity as a function of scan rate and cycle number.

7.4 Conclusions

Polydopamine was successfully polymerized onto the surface of NTP particles in aqueous solution. Both the raw polydopamine coating and the carbon coating produced from pyrolysis of polydopamine showed considerably slower rates of capacity fade during cycling than the control of uncoated NTP. Although the rate of capacity fade was slower for the carbon coated sample when compared to the polydopamine coated sample, the polydopamine sample showed a lower standard deviation in capacity and a slower increase of overpotentials during cycling. No

114

secondary reduction peak that would be indicative of dissolution NTP was observed in the coated samples. These results indicate that coating of NTP can greatly improve the cycle stability of the electrode material. However, it does not completely prevent capacity fade, indicating that some mechanism other than dissolution must also be contributing to the capacity fade. The next chapter will explore the effect of generated gas on the performance of NTP electrodes.

Chapter 8: Gas Generation in NTP Aqueous Anodes

8.1 Overview

The results of the in-situ pH measurement as well as the observation of bubbles forming on the CV test fixture during the experiments indicates that hydrogen evolution is definitely a problem for NTP based aqueous anodes. It has also been found that although coating NTP with PPy improves the cycle stability when compared to uncoated material, there is still a significant amount of capacity fade during cycling. Similarly, for the materials coated in polydopamine and carbon, capacity fade is greatly slowed, but remains a problem. We suspect that capacity fade must also be occurring due to loss of ECSA caused by entrapped gas.

In order for the active ions of a system to access the active material the electrode structure must contain a significant fraction of porous volume that can be back filled with electrolyte. If for some reason the electrolyte is prevented from entering into a given pore volume the surface area of the conductive additive and active material within this region will no longer be able to undergo redox processes and hence will become electrochemically inactive. If some reaction should occur within the electrode that causes the formation of a gas bubble, the bubble will prevent electrolyte from accessing the surface area within the pore where the bubble is located. What we are interested in is, given a particular amount of gas produced, what amount of ECSA are we losing? And as a consequence, what is the apparent loss of capacity of the electrode? We are also interested in whether or not it is possible to remove trapped gas and recover the capacity that has been lost.

We'll start by defining a few relationships. First, we know from thermodynamics that there exists a relationship between the moles of gas, pressure of the gas, and its volume, known as the ideal gas law:

$$PV = nRT$$

Where P is the pressure, V is the volume, n is the number of moles of gas, R is the gas constant, and T is the temperature in kelvin. We also know that the equilibrium pressure inside of a cylindrical pore is dependent on the surface tension of the liquid in the pore and the contact angle of the liquid, and is inversely proportional to the pore radius.

$$P = \frac{2\gamma \cos(\theta)}{r}$$

Where γ is the surface tension of the wetting phase, θ is the equilibrium contact angle between the two phases, and r is the pore radius. Combining the ideal gas law, the capillary pressure, assuming the contact angle to be zero (hydrophilic pores) and solving for the volume of gas gives:

$$V = \frac{nRT}{2\gamma} r$$

So we should expect that the volume of gas within a pore will be directly proportional to the radius of the pore. This implies that electrodes with smaller pores should experience less capacity fade due to gas entrapment.

The actual relationship between the volume of entrapped gas and the amount of ECSA that is lost is not so clear. Depending on the pore size distribution and geometry of the pores this relationship could be quite different. On top of this, it is not entirely clear how the fraction of ECSA lost relates to the fraction of active material that becomes electrochemically inactive,

since this relationship will depend largely on the rate of diffusion in the active material, and the size and geometry of the active material particles. That being said the amount of ECSA that is lost during cycling should still be a useful measure of capacity loss.

There are a few electrochemical techniques that can tell us about the ECSA of an electrode. One of these is potentiostatic titration, where a small step in the potential is applied and the current is allowed to relax to a steady-state. Using the Butler-Volmer equation we can relate the steady-state current to the exchange current, which is directly proportional to the ECSA. So by measuring the change in steady-state current over many cycles of a step potential test, we can determine the change in the ECSA and map this to a loss of capacity. We can also determine whether or not this loss of capacity is truly due to trapped gas or perhaps some other mechanism, by either removing gas that has been generated, or by decreasing the volume of the gas by increasing the hydrostatic pressure of the electrolyte solution. This can be accomplished by cycling an NTP electrode in a sealed vessel that can undergo both evacuation and pressurization.

8.2 Experimental

8.2.1 Materials

For this test NTP produce via the solvothermal synthesis described in chapter 3.2 was used because of its uniform particle size, high rate capability due to the small particle size, and relatively high phase purity. The small particle size helped ensure that steady state currents could be reached in relatively short times after applying a potential step.

In order to prepare the electrodes, the NTP was mixed in a mortar and pestle with carbon black and PVDF in a mass ratio of 70:20:10. After a homogenous powder was formed, several drops of NMP were added and the mixture was formed into a thick paste, after which it was placed into an oven at 80 °C overnight to dry. The dried electrode material was run through an 80x80 mesh screen to obtain a uniform sized electrode powder. Approximately 30 mg of powder was placed in a 10 mm diameter steel die and pressed to 3 tonne in order to form an electrode pellet of uniform thickness and density, which was then cut into several small rectangles. These rectangles, weighing ~5 mg, were then pressed into a folded piece of stainless steel mesh at 3 tonne in order to form the working electrode.

8.2.2 Potentiostatic Cycling

A half-cell set up using a platinum wire electrode and MSE (all reported potentials are versus MSE unless otherwise stated) reference electrode in 1 M Na_2SO_4 was used, with N_2 purge gas running for the duration of the experiment. Potential steps of 20 mV with a duration of 300 seconds for each step were used from -0.48 to -1.24 V, 10 mV steps with durations of 900 seconds each were used from -1.24 – 1.32 V since this is the region were NTP undergoes redox reactions, and 20 mV steps with durations of 300 seconds were used from -1.32 to -1.40 V. After the potential steps, a linear voltammetry sweep back to -0.48 V with a two hour potential hold and a 2 hour open circuit potential measurement were used. The test profile can be found in Figure 7.1, and was repeated for a total of ten cycles. In order to facilitate the fitting of the steady-state current, planar diffusion through the electrode with a no flux boundary condition at

the center of the electrode was assumed. This allows the current as a function of time for a small potential step to be defined as:

$$i(t) = \frac{QD^{1/2}}{L\pi^{1/2}}\frac{1}{\sqrt{t}} + \frac{2QD}{L^2}e^{-\frac{\pi^2 Dt}{4L^2}} + i_{eq}$$

Where Q is the amount of charge passed, D is the diffusion coefficient, and L is the characteristic diffusion length[106]. Note that as t tends towards infinity the first and second terms tend towards zero, leaving only the steady-state current term defined by the Butler-Volmer equation. Rather than trying to fit or define Q, D, and L, since we are only interested in the magnitude of the coefficient of the second term it is useful to rewrite the equation as:

$$i(t) = a\frac{1}{\sqrt{t}} + be^{-kt} + i_{eq}$$

This equation was fit to the measured current for each potential step using the Levenberg-Marquardt method. The coefficient, b, could then be taken as the steady-state current. Due to the redox process of NTP, the potential steps from -1.22 to -1.30 V were not fit using this equation.
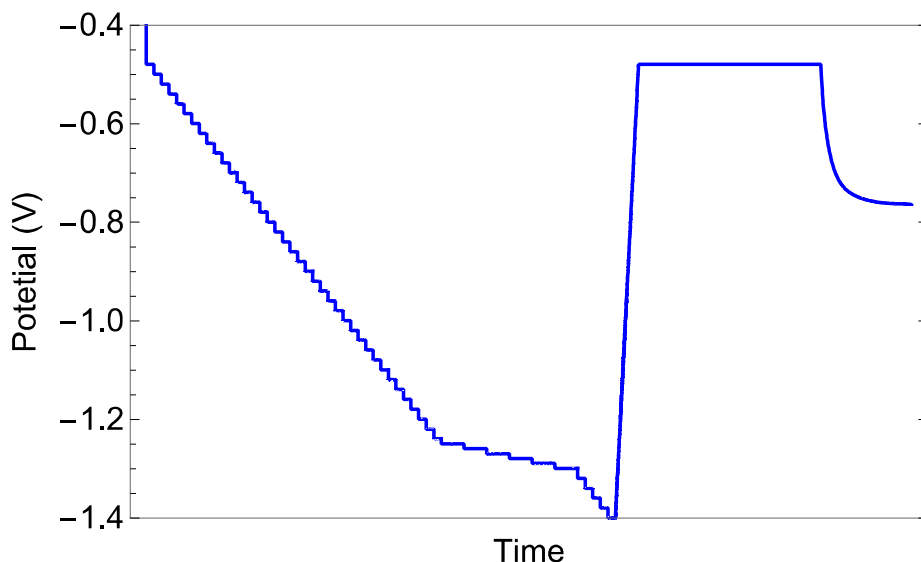
Figure 8.1 Representative test profile showing the potential steps followed by linear sweep voltammetry, constant voltage hold, and open circuit potential measurement.

8.2.3 Vacuum-pressure Cycling

A Parr instruments autoclave with four ports was modified so that two ports could be used as electrical feedthroughs, one port could be used to either release pressure or pump a vacuum, and one port could be used for pressurization. A picture of the apparatus can be found in Figure 8.2. A glass three electrode cell consisting of a platinum wire counter electrode, a mercury sulfate reference electrode, and an NTP working electrode was assembled and connected to the electrical feedthrough connections before being lowered into the vessel. In order to prevent a pressure differential between the inner chamber of the reference electrode and the vessel, a capillary tube was connected to the reference electrode's electrolyte fill port. This capillary tube allowed for pressure equalization without excess loss of the reference electrode fill solution during the evacuation process. Prior to the addition of the capillary tube, data was collected and is presented in this document. The point of failure of the reference electrode is noted and was determined based on a sudden change in the voltage profiles of both the counter and working electrodes, though the authors would like to emphasize that this data should be considered with a grain of salt.
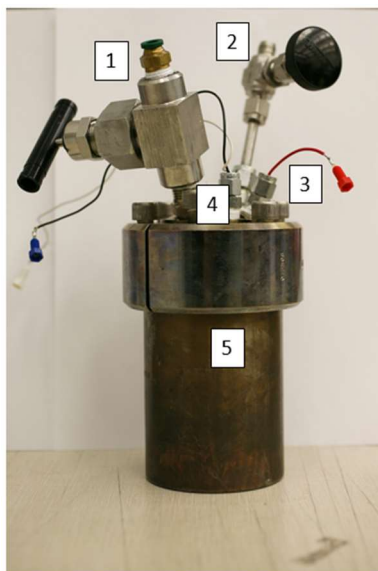
Figure 8.2 The modified autoclave used in the vacuum pressure experiments: (1) pressurized gas inlet, (2) vacuum port and pressure release, (3) working electrode connection, (4) counter and reference electrode connections, and (5) the steel vessel.

The electrochemical test procedure used for this test consisted of 6 or 11 GCPL cycles at 1 mA and 0.4 mA respectively, in which the NTP electrode was reduced to -1.4 V vs MSE and oxidized to -0.4 V vs MSE. The 6 cycles at 1 mA represents a relatively quick cycling regime, producing some gas but not an excessive amount. The 11 cycles at 0.4 mA represents a relatively slow cycling regime, and produces considerably more gas than the faster rate. After each set of cycles, there was a 4 hour open circuit period. During this time a vacuum pump was connected to the vessel, and a vacuum was pumped for 15 seconds before closing the needle valve connection. The cell was left in this evacuated state for 3 minutes before once again pumping a vacuum for 15 seconds. This process was repeated 5 times to removed trapped gas without excess boiling of the electrolyte. After the vacuum steps, the vacuum connection was removed and the vessel was pressurized to 60 psi using an Argon gas cylinder. After 3 minutes at pressure, the needle valve for the vacuum port was opened to release the pressure. The valve was then closed and the vessel was once again pressurized. This process was repeated 5 times. At the end of this process the cell

was left in the pressurized state for further testing. This vacuum-pressurization process was repeated after every two sets of galvanostatic cycling.

8.3 Results and Discussion

8.3.1 Potentiostatic Cycling

Figure 8.3 shows characteristic current responses for the potential steps between -1.32 and -1.40 V. The noise in the measured current arises from the agitation of electrolyte caused by nitrogen that was being bubbled through the system, as well as the formation and release of gas bubbles on the electrode surface.
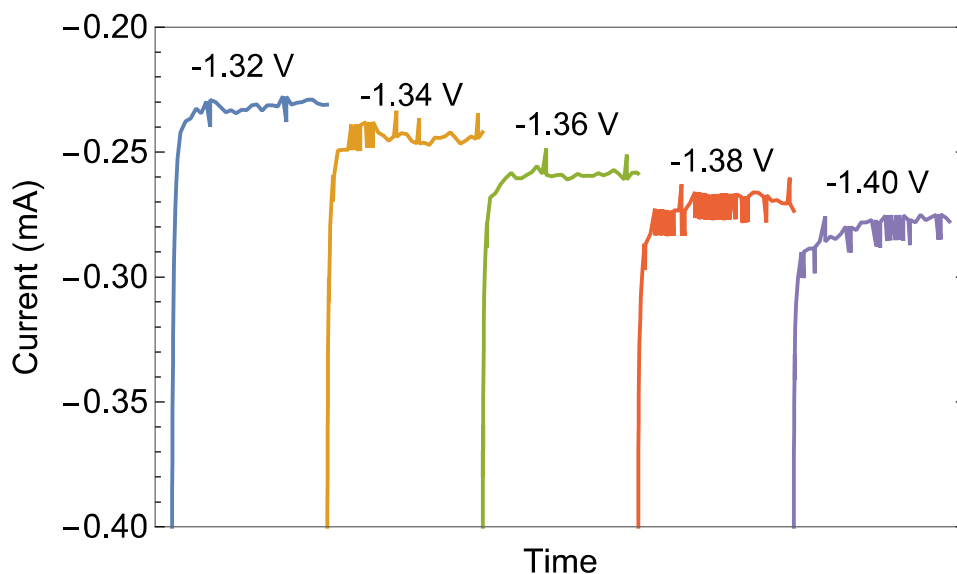
Figure 8.3 Measured relaxation currents from -1.32 to -1.4 V for a single cycle of the test.

Figure 8.4a shows a representative best fit line (black) used to obtain the steady-state current from the measured (blue) current relaxation. The change in steady-state current at potentials from -1.32 to -1.4 V can be found in Figure 8.4b. It was found that the steady-state current increased for the first three cycles, most likely due to wetting of the porous electrode, after which it

decreased an average of about 4.4% per cycle. It's not clear that a linear fit is the best for the collected data, as the rate of decrease in the measured current appears to slow down in the later cycles. Indeed, if we compared the change in the peak current (Figure 8.5c) measured during the linear voltammetry sweep back to -0.5 V we see that the rate at which the peak height decreases is nonlinear and decreases with each cycle.
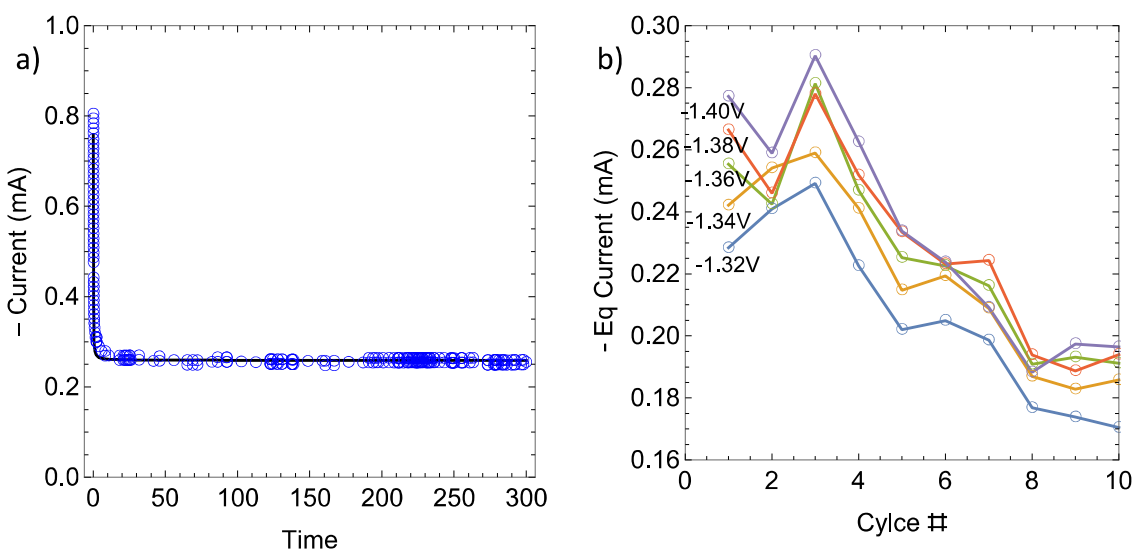
Figure 8.4 (a) The measured current relaxation (blue circles) and the best fit line (black) used to obtain the steady-state current. (b) The steady-state current for the highest potential steps, shown as a function of cycle number.

It is also useful to look at both the current relaxation during the constant voltage hold at -0.48 V and the drift in open circuit potential after the voltage hold is finished. Figure 8.5b shows the current relaxation for the first cycle and the 10th cycle. Since the magnitude of the current relaxation is increasing with each cycle, we can say that more and more material becomes inaccessible until well after the normal oxidation potentials. This indicates that there is a mass transport limitation in the electrode. This is also supported by the linear voltammetry curves, with increasing cycle number lower peak currents are observed but higher currents are observed at voltages greater than -1.0 V for increasing cycle number (Figure 8.5a). The increased current

124

at lower potentials rules out the possibility that the decrease in magnitude of the steady-state current was caused by loss of material from physical separation. The open circuit measurements point to a similar phenomenon (Figure 8.5d). As the number of cycles increases, the open circuit potential relaxes to lower and lower potentials, indicating that more of the electrode material is remaining in a reduced state even after the linear sweep and constant potential holds.
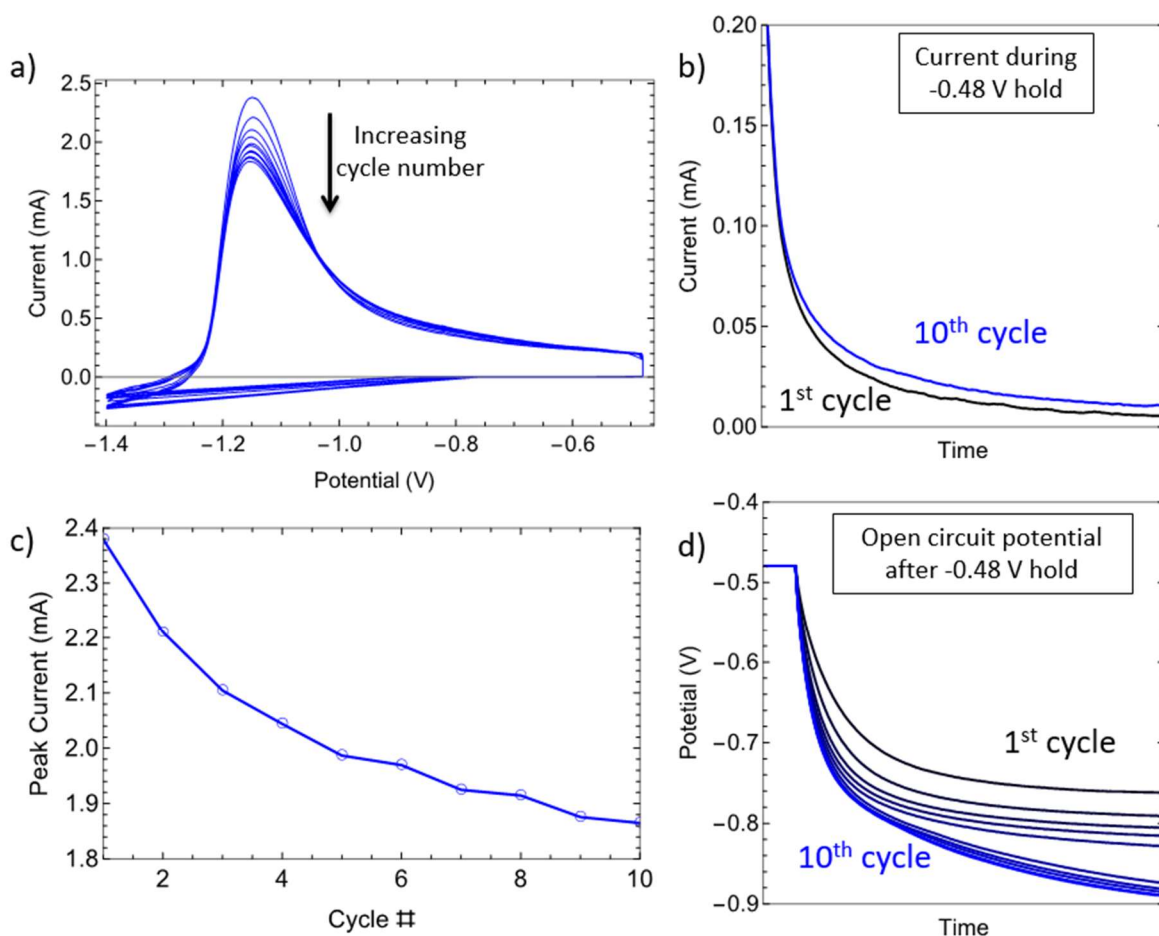
Figure 8.5 (a) Current measurements from the linear sweep voltammetry showing the decreasing peak current. (b) Current relaxation during the constant voltage hold at -0.48 V, only the 1st and 10th cycle are shown for clarity. (c) The measured peak current during each of the 10 cycles showing a nonlinear decrease with increasing cycle number. (d) Open circuit potential measurements, showing lower and lower equilibrium potentials with increasing cycle number.

8.3.2 Vacuum-Pressure Cycling

The results from the vacuum-pressure cycled cells show the effect of trapped gas much more clearly. Figure 8.6 shows the capacity as a function of cycle number for the fast cycling condition. The first few cycles show the highest rate of capacity loss. This is easy to explain from the perspective of lost ECSA based on the pH as a function of cycling presented in Chapter 5: early on, when the pH is low, the difference between the equilibrium potential for hydrogen evolution and the applied potential is at its greatest, and so the rate of hydrogen evolution is at its greatest. As the pH in the electrode increases during cycling, the rate of hydrogen evolution decreases. Not only does the decrease occur because of the higher pH but because as more hydrogen is generated, more surface area is lost for carrying out the HER.
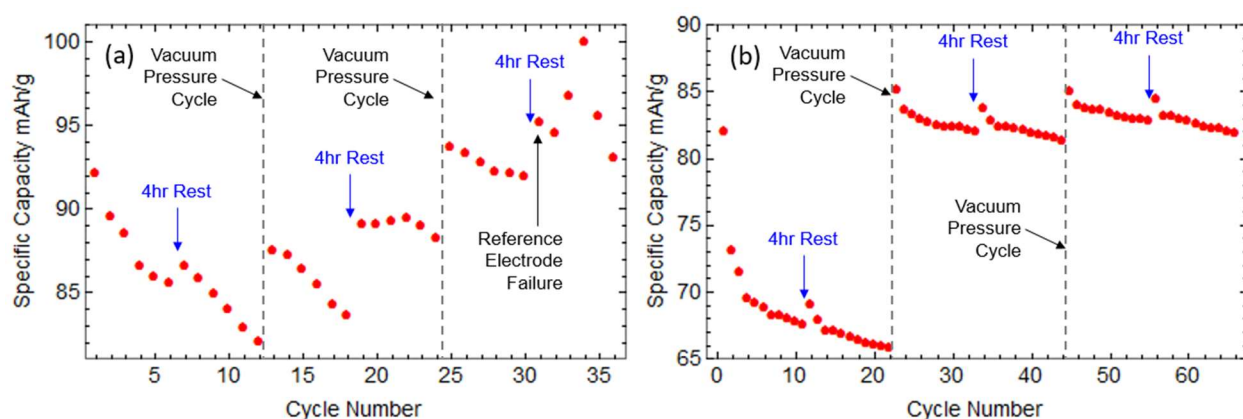
Figure 8.6 Capacity versus cycle number when a vacuum-pressure cycle is used to reinfiltrate electrodes. (a) Material cycled at a relatively fast rate, and (b) material cycled at a slower rate.

During the rest period between the first two sets of cycling, and prior to application of a vacuum-pressure step, a small increase in capacity is observed. This is consistent with electrolyte reinfilitrating pores that had originally become gas filled. This most likely occurs through dissolution of the hydrogen gas followed by transport out of the electrode into the bulk electrolyte of the glass electrochemical cell where the gas later nucleates as a bubble (usually on the reference electrode). After a single vacuum-pressure cycle, the electrode regained ~60% of

the total capacity it had lost during the first 12 cycles, but the rate of capacity fade during the first six cycles after the vacuum-pressure step remains comparable to what it was prior to the reinfilltration. After resting for 4 hours, the capacity of the electrode again increased. The rate of capacity fade during this cycle was also considerably lower than for the previous cycles (in fact the capacity increased for the first few cycles before beginning to decrease). The reader should be reminded that no further vacuum-pressure step has been conducted and so the increase in capacity between the first set of pressure cycles and the second set cannot be attributed to the reinfiltration through such means, though it remains unclear how capacity is being recovered in this case.

After a second vacuum-pressure step, the specific capacity once again increased, this time to 102% of the original capacity. This would indicate that the electrode has become better infiltrated than it was on the first discharge. Given that the materials used to produce the composite electrode are relatively hydrophobic, it is not difficult to believe that through repeated vacuum-pressure cycles the porous electrode had become more well infiltrated with electrolyte. The results of this particular experiment were collected before the capillary tube had been connected to the reference electrode, and so the results should be taken with a grain of salt. However, there was a clear difference in the apparent voltage of both the counter and working electrode at the point marked in Figure 8.6a, indicating the point at which the reference electrode was no longer acting as a stable reference electrode.

Results from the slow cycling conditions can be found in Figure 8.6b. It should be first noted that the specific discharge capacity is lower than what was seen at higher rates, as is the coulombic efficiency. This occurs for a couple of reason. First, a platinum wire counter electrode was used

in this system, which generate protons as well as oxygen when the NTP electrode is being reduced. The dissolved oxygen then reacts with the reduced NTP causing it to be chemically oxidized to its desodiated state. Thusly, less capacity can be recovered upon discharge of the electrode. Secondly, the longer time spent at potentials below the potential for hydrogen evolution, the more hydrogen gas will be produced. The more hydrogen gas produced, the higher the loss of ECSA, and the higher the loss of ECSA, the less capacity can be recovered. Because of these two mechanisms, not only is the discharge capacity lower than at higher rates, but the total lost capacity is much higher, after only six cycles 18% of the initial discharge capacity had been lost. This compares with the faster rates capacity loss after 6 cycles of only 8% of the initial capacity.

After application of the vacuum-pressure cycle, the discharge capacity increased to 105% of the original discharge capacity. This is a particularly striking result. It indicates that a single vacuum-pressure cycle after some break-in period can allow for full recovery of the initial discharge capacity, and then some. The rate of capacity fade in later cycles is comparable, and appears to not be effected by cycling at higher pressures.

8.4 Conclusions

From the potentiostatic cycling test, the increasing current during the potential hold at -0.48 V, larger and larger potential drift during the open circuit period, and the decreasing magnitude of steady-state currents all point towards loss of ECSA due to mass transfer limitations. Direct application of both vacuum and hydrostatic pressure indicate these limitations are a direct result of gas entrapment within the pore network of the electrode. After application of a single vacuum-pressure cycle during slow cycling of an electrode, a dramatic recovery of lost capacity was

observed. In fact, more capacity was recovered than had originally been lost. These results indicate that the major fraction of capacity loss during cycling of these electrodes is a result of lost ECSA due to trapped gas. So if thick porous electrodes of these materials (or any electrode of sufficiently low potential) are to be used in aqueous electrolytes, the detrimental effects of trapped gas must be addressed.

Chapter 9: Effect of Compositing and Modifying Wettability

9.1 Overview

From the results presented in Chapter 8 it is clear that loss of ECSA due to gas entrapment is the major factor in the capacity loss for NTP electrodes. Not only that, but gas entrapment should be a major contributor to apparent capacity loss for any anode of low enough potential in aqueous electrolyte. What can be done to minimize the negative impacts of hydrogen gas generation in porous electrodes?

As mentioned in the introduction, most materials systems in aqueous electrolyte show poor cycling performance, with the exception of systems that use activated carbon as an anode. So why does activated carbon allow for a long cycle life? Let's discuss how activated carbon operates when used as an aqueous anode.

Activated carbon electrodes rely on double layer capacitance for charge storage. Since the amount of charge storage per unit mass is directly proportional to the specific surface area of the activated carbon, surface areas on the order of 1500-3000 m^2/g are needed to obtain activated carbons with favorable specific capacities. In order to obtain such high surface areas, activated carbon needs a high density of pores on the order of 10-30 Å in diameter. As mentioned in the earlier section on gas generation within porous structures, the equilibrium pressure of a pore is inversely proportional to the size of the pore, if we assume a hydrophilic pore and aqueous electrolyte a 1 nm diameter pore will have an equilibrium pressure of ~2000 atm. Because of this, several groups have researched activated carbon as a material for the electrochemical storage of hydrogen. Notably, utilizing activated carbon in strongly alkaline aqueous electrolytes

allows for storage of as much as 2 wt% hydrogen gas with a well-defined discharge plateau. The overall quantity of hydrogen that can be adsorbed depends on the ability of H^*, generated during the Volmer reaction, to diffuse into the micropores. If the diffusion of H^* in the micropores is sluggish, then recombination via the Tafel or Heyrovsky reactions will occur[107,108]. That activated carbon is capable of reversibly storing hydrogen rather than simply generating hydrogen gas that blocks off active surface area, is the most likely explanation as to why aqueous batteries that have used it as an anode showed such high cycle life. Therefore, we believe it should be possible to add some mass fraction of activated carbon to an NTP based electrode in order to promote hydrogen storage within the activated carbon rather than hydrogen gas formation within the macropores of the electrode. The equilibrium volume of trapped gas is not only inversely proportional to the radius of the pores, but directly proportional to both the surface tension and the cosine of the wetting angle. Because the materials we use to produce a cohesive electrode tend to be hydrophobic, we should consider increasing the wettability of the electrode pores to further increase the equilibrium pressure of entrapped hydrogen gas. However, this is easier said than done.

The electrodes we have been using consist of a mixture of NTP, highly graphitized carbon black designed for organic Li-ion cells, and PVDF, both of which are hydrophobic, so to increase the wettability we would have to modify the surface chemistry of both the carbon black and the PVDF. It is unclear how this could be done for PVDF, but for carbon black, a partial oxidation of the carbon surface could enhance the wettability. This partial oxidation, however, could have deleterious effects on the conductivity (both from disordering of the carbon surface and possibly effecting the tendency of carbon black to form a particle gel network needed for efficient electrical percolation). So rather than attempt to change the hydrophilicity of the electrode

materials themselves, we opted for modifying relative hydrophilic/lipophilic properties of the electrolyte solution through the addition of a surfactant, Triton X-100. Fig 9.1 shows the chemical structure of Triton X-100. It consists of a hydrophilic tail of polyethylene oxide (PEO) and a 4-(1,1,3,3-tetramethylbutyl)-phenyl group as a hydrophobic head. We chose this particular surfactant because it has been well characterized, is widely used within the Li-ion battery community for dispersion of carbon within electrode slurries, and is used widely in electrochemistry to enhance transfer across water-oil interfaces[109–112]. Because of this we had good reason to believe it would be stable under our cycling conditions and perform well for enhancing the wettability of carbon black and PVDF.

M.W. = 647 g/mol
CMC = 1.55e-7 mol/mL
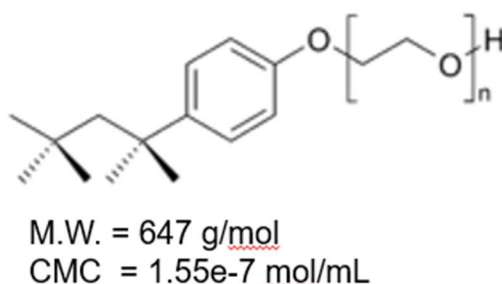
Figure 9.1 Molecular structure of the surfactant, Triton X-100. The PEO chain length, n, is between 9 and 10.

9.2 Experimental

9.2.1 Materials Preparation

The electrolyte was produced by dissolving anhydrous sodium sulfate into 18.2 MΩ deionized water to form a solution of 1 M Na_2SO_4. To 50 mL of the 1 M Na_2SO_4 electrolyte 20-30 mg of Triton X-100 was added. Upon mixing the solution became slightly cloudy. The final solution had a concentration of 7.7±1.7 e-7 mol/mL for the triton X-100. This concentration is above the CMC of 1.55e-7 mol/mL[113].

Solvothermally produced NTP, as described in Chapter 3.2, was used for this experiment. Electrode composites were produced by combining PVDF (Alfa Aesar), carbon black (Timcal Super-P), and NTP or NTP with activated carbon (Fuzhou Yihuan Carbon Co. YEC-8), in a mass ratio of 10:20:70. For the composites containing activated carbon a mass ratio of activated carbon to NTP was 1:6. This mixture was placed in a mortar and pestle and combined until the powder was well homogenized, after which a few drops of NMP were added. The material was then mixed until a thick, uniform, paste was formed. This paste was smeared into a thin layer within the mortar before being placed in an oven at 80 °C overnight to dry. After drying, the material was scraped from the inside of the mortar and then granulated through a stainless steel mesh screen. Approximately 40 mg of this granulate was then pressed to 3 metric tonnes in a 10 mm stainless steel die set to produced electrode pellets. These pellets were cut into small squares of ~4mg mass each, which were then placed between a folded piece of stainless steel mesh and then pressed to 6 metric tonnes.

9.2.2 Characterization

Two pellets were used to obtain images of electrolyte contact angles. A Canon 5D DSLR with a 50mm macro lens was used for imaging and placed so that the edge of the electrode pellet was in the center of view. A single drop of electrolyte (with or without Triton X-100) was placed on the center of the pellet using a plastic pipette and allowed to sit for 10 seconds before a photo was taken. ImageJ software was used to obtain an estimate of the contact angle.

Cyclic voltammetry was used to characterize the performance of electrodes with and without activated carbon, as well as with activated carbon and Triton X-100. The different electrode systems will be referred to as NC for the control, NCTX for the control with Triton X-100 in the

electrolyte, NAC for electrodes containing activated carbon, and NACTX for electrodes containing activated carbon with Triton X-100 in the electrolyte. Electrodes were cycled between -1.5 and -0.5 V versus mercury sulfate, at a scan rate of 1 mV/s. Cartoons of the electrochemical set up and electrodes are shown in Fig 3.1a.

9.3 Results

It is important to note that by adding a surfactant to the electrolyte we are not only decreasing the equilibrium contact angle of the electrolyte solution, but the surface tension. The efficacy of this method is then reliant on the product of the surface tension and cosine of the contact angle being larger with the surfactant than without. Figure 9.2 gives a qualitative depiction of the decrease in contact angle between 1 M Na_2SO_4 and our electrode upon addition of Triton X-100. Although this contact angle experiment was not performed in a rigorous manner, it still gives us a reasonable starting point to estimate the magnitude of the different capillary pressures. an angle of ~88° was found for 1 M Na_2SO_4 and ~30° for 1 M Na_2SO_4 upon addition of Triton X-100. This would imply and increase in capillary pressure by a factor of ~25 if only the contact angle is considered. It has been found that upon addition of Triton X-100 to deionized water, the surface tensions will decrease from 72 mN/m to 34 mN/m (at a concentration of triton x-100 one order of magnitude above the critical micelle concentration (CMC)) or 49mN/m (at CMC) [113]. This would imply a decrease in capillary pressure by a factor of ~2 if only surface tension is considered. Combining the decrease in contact angle and decrease in surface tension, we should expect the capillary pressure to increase by a factor of ~10. It should be mentioned that we have not accounted for phenomena such as electroosmotic pressure.
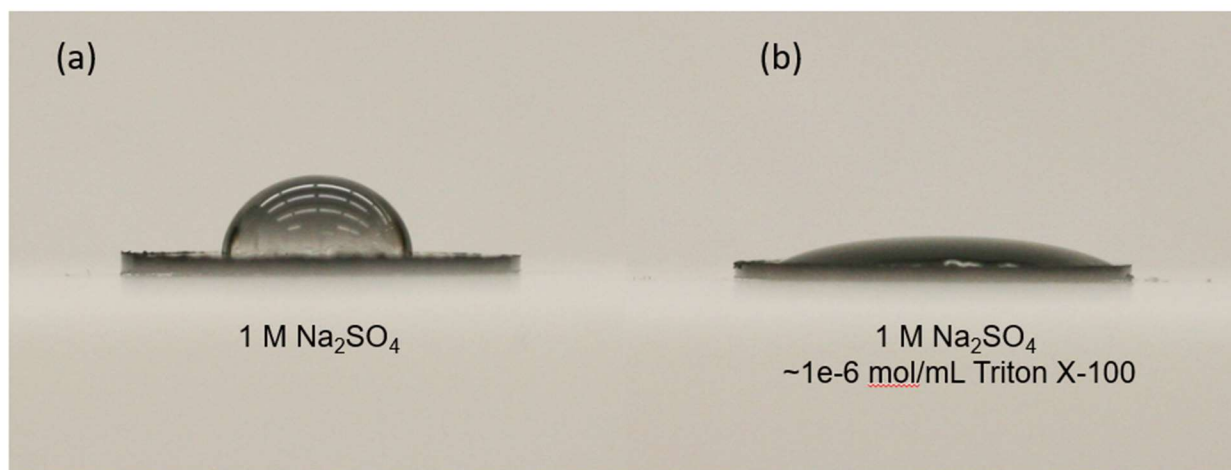
Figure 9.2 Contact angle images of (a) 1 M Na$_2$SO$_4$ and (b) 1 M Na$_2$SO$_4$ with Triton X-100 surfactant.

Figure 9.3 shows the specific capacity of the different electrode materials as a function of cycle number. Similar to the results from coating NTP with polydopamine or carbon, the control demonstrates the highest initial capacity. This is because activated carbon has a lower specific capacity than NTP and makes up 10 wt% of NAC and NACTX electrode systems. Compared to the control, NCTX and NAC show a much more stable and considerably slower decrease in capacity during cycling. From the results collected for NCTX, it is clear that the addition of Triton X-100 to the electrolyte can greatly decrease the rate of capacity fade. It is unclear however, whether this is due to higher capillary pressure and hence smaller volume of entrapped gas, or if it is due to the surfactant interfering with the proton adsorption step of the hydrogen evolution reaction.

The initial rates of capacity fade for NACTX compared to NAC, are a bit counter-intuitive. It was originally posited that by increasing the wettability of the electrodes, the equilibrium volume of the trapped hydrogen gas would be lower, and so we would expect to see a slower rate of capacity fade. Instead, the initial rate of capacity fade for NACTX samples was faster than either NC or NAC electrodes. A possible reason for this is that hydrogen gas generated within the other

electrodes does not have to fight high capillary pressures in order to expand and eventually nucleate as a bubble near the surface of the electrode. This mechanism of hydrogen gas removal through a gas filled pore ought to be fast compared to hydrogen dissolution and aqueous phase transport out of the electrode. So, although the total volume of a given quantity of hydrogen gas is smaller in NACTX, the overall quantity of hydrogen trapped is much larger. However, this trend of rapid capacity fade does not continue into later cycles. Unlike all other samples tested, NACTX shows an eventual increase in capacity during cycling, leading to capacities comparable to or slightly higher than the original capacity. What is happening within the electrode that could cause this?
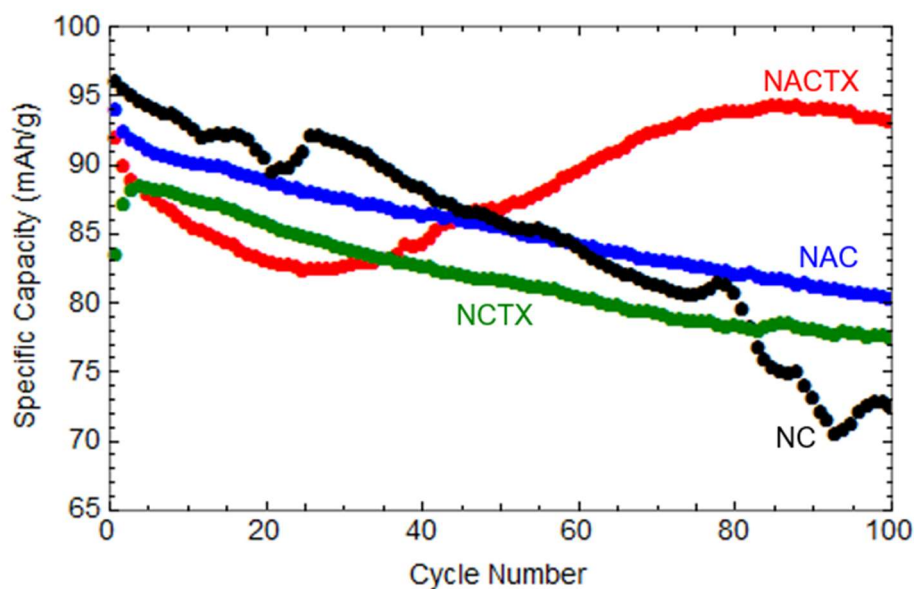
Figure 9.3 Specific capacity versus cycle number for the control, NC (black), the sample containing activated carbon but without surfactant in the electrolyte, NCTX (Green), NAC (blue), and the sample with both activated carbon in the electrode and surfactant in the electrolyte, NACTX (red).

Examining the CV curve of NACTX, shown in Figure 9.4, we see that the peak current of both the oxidation and reduction peaks decrease between the 2nd and 25th cycle. However, between the 25th and 50th cycles a notable increasing in the reduction current at potentials < -1.3 occurs and is

accompanied by the formation of a new, broad peak during oxidation. Such features are not observed in NC or NAC samples. These new features in the CV curve become more prominent in later cycles. The maximum discharge capacity occurs during the 85th cycle, after which the capacity begins to decrease again. It is unclear whether or not the capacity would continue to decrease during cycling, or if the system shows some oscillation in capacities.
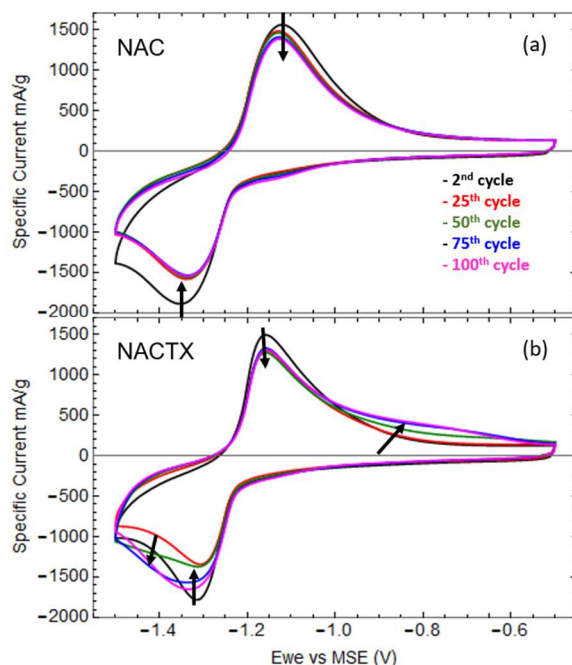
Figure 9.4 Cyclic voltammetry curves for the (a) NAC and (b) NACTX samples. The 2nd, 25th, 50th, 75th, and 100th cycle are shown with arrows indicating the direction of increasing cycle number.

The particular features observed in the CV curve are consistent with previous reports of reversible electrochemical storage of hydrogen within activated carbons[107]. Figure 9.5 shows CV curves of activated carbon in alkaline electrolyte, and the total reversible capacity of hydrogen as a function of the minimum vertex potential. In Figure 9.5, the curve that has an equivalent lower potential to the ones used for NACTX has been colored red. The obtained CV curves for NACTX show a combination of redox processes associated both with the normal intercalation mechanism of NTP as well as the reversible electrochemical storage of hydrogen in

the activated carbon. This reversible hydrogen storage was not observed in the CV curves for the activated carbon electrode that did not contain surfactant in the electrolyte. Though NAC does show the standard double layer capacitance current normally seen with activated carbon based electrodes.
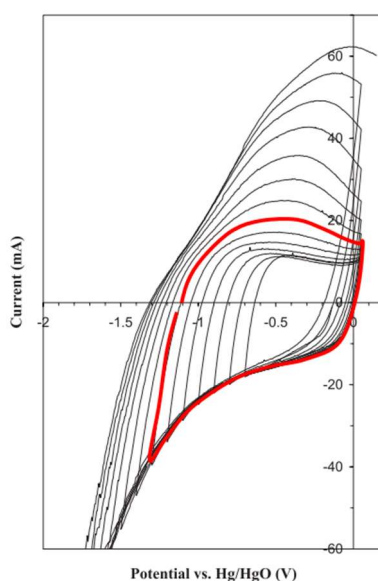
Figure 9.5 Dependence of the voltammetry characteristics of AC (15.2 mg) with the value of negative potential cut-off. Electrolyte: 3 M KOH. Scan rate of potential: 5 mV/s. The various loops are obtained by stepwise (100 mV) shifting the potential cut-off to more negative values. Reprinted from [107].

This data suggests that through modification of the electrode's wettability, we are able to promote the reversible storage of hydrogen within the electrode. Considering that the total amount of hydrogen undergoing pseudocapacitive reactions at the surface of the activated carbon will depend on the pressure of the hydrogen gas, these results are not too surprising. However, it is surprising that this process requires 25+ cycles before becoming measurably active. The reason for this delayed onset is unclear but it could be related to a minimum necessary pH for the reaction to proceed at a reasonable rate, or a minimum pressure of hydrogen having to be reached in order for the pseudocapacitive storage to become favorable.

9.4 Conclusions

Although the results presented here are preliminary, it appears that the addition of activated carbon and modification of the wettability of NTP electrodes offers a potential method for mitigating the detrimental effects of hydrogen gas generation within the electrode. This mitigation relies on the ability to reversibly store hydrogen within the composite electrode at high pressures. As of yet it is unclear whether this reversible hydrogen storage persists after several hundreds of cycles, or what effect a full cell configuration might have on the processes responsible for this hydrogen storage. Future work should focus on understanding the precise mechanism responsible for the observed effect, and whether or not it is possible to activate this mechanism from the start of cycling rather than having to wait for 25 cycles. Methods for enhancing the wettability of the electrode structure aside from the addition of surfactant to the electrolyte should also be explored.

Chapter 10: Concluding Remarks/Future directions

In this body of work, we set out to investigate the failure mechanism of $NaTi_2(PO_4)_3$ based electrodes when used in aqueous electrolytes. The primary mechanisms that were investigated were dissolution and effects of high pH solutions on performance, and loss of electrochemical surface area due to entrapment of hydrogen gas within the porous electrode. Both of these mechanisms occur due to the low potential of the NTP redox couple. This low potential coincides with the potentials at which the hydrogen evolution reaction becomes prominent, leading to the generation of OH^- and $H_2(g)$.

In order to address these degradation mechanisms, a few methods were employed to varying degrees of success. The initial attempt to coat NTP with a conjugate polymer, polypyrrole (PPy), worked to some degree but showed several unfavorable characteristics. In particular, the poor coverage of NTP due weak bonding between the PPy and NTP limited the overall performance enhancement due to the coating. Because of this, we turned to polydopamine to ensure sufficient adhesion and allow for a conformal coating of the NTP particles. This polydopamine coating performed best once it had been pyrolyzed into carbon. This was not too surprising since carbon coating is the most common method for enhancement of electrode material performance. Carbon coating of NTP particles improved the cycle stability of the electrode material by ~ 5 fold, but did not stop capacity fade entirely.

Further testing revealed that although high pH and dissolution may be a problem for full cells where the cathode to anode mass ratio was high, it was not significant enough to account for the observed capacity loss. A relatively simply vacuum-pressure experiment demonstrated that the

main cause of apparent capacity loss within these electrodes was the generation of hydrogen gas, and its entrapment within the pore network of the electrode. Preliminary results of compositing NTP with activated carbon and enhancing its wettability through addition of a surfactant to the electrolyte, indicate that it is possible to reverse the determinantal effects of trapped gas on the measure capacity. However, the mechanism responsible for this reversal of the HER does not become prominent until after ~25 cycles. This late onset of capacity recovery would not be useful in a full cell configuration as it would cause the cathode potential to drift to much higher potentials, limiting the overall capacity if voltage limited cycling was being utilized.

Future work should focus on determining the precise mechanism of the enhancement observed upon the addition of surfactant to the electrolyte. In particular, measuring the change in pH of composited electrodes will be necessary to understand whether the addition of activated carbon has effected the rate of HER, or the rate at which OH^- diffuses out of the electrode. It will also be necessary to determine to what extent this method works in a full cell configuration. It is possible that the presence of a properly sized cathode may prevent reversible hydrogen storage by neutralizing hydroxide ions necessary for the reaction to occur. It will also be necessary to investigate methods, other than surfactant addition, for enhancing the wettability of the electrodes.

Another area for future research should be understanding the mechanism by which coating of the material enhances the electrochemical performance. It remains unclear to what extent the tested coatings are enhancing performance by preventing dissolution of NTP, versus preventing excess generation of hydrogen gas. Considering both the vacuum-pressure data and the capacity

retention of coated samples during cycling, it would appear that the coated materials show a much slower rate of hydrogen gas generation. This would be the case if the NTP surface was more favorable for any of the HER steps (Volmer, Tafel, Heyrovsky) than the carbon surface or polydopamine surfaces. This particular hypothesis will require more work to be confirmed or rejected.

My last comment on this work, is that addressing the problem of gas entrapment for anode materials to be used in aqueous rocking chair type chemistries will be necessary if the materials are to be commercialized. Therefore, if academic research of aqueous alkali-ion battery chemistries is to remain relevant, significant effort should be put into further understanding gas entrapment and determining what methods are best suited for eliminating the detrimental effects it causes. Some effort should be put in to researching methods for either recombination of generated gases, or preventing the gas generation altogether (perhaps by preventing the first step of HER, hydrogen adsorption).

References

[1] B. Dunn, H. Kamath, J.-M. Tarascon, Electrical Energy Storage for the Grid: A Battery of Choices, Science (80-.). 334 (2011) 928–935. doi:10.1126/science.1212741.

[2] E. Hittinger, T. Wiley, J. Kluza, J. Whitacre, Evaluating the Value of Batteries in Microgrid Electricity Systems Using a Novel Energy System Model, Energy Convers. Manag. 89 (2015) 21. doi:10.1016/j.enconman.2014.10.011.

[3] D. Linden, T.B. Reddy, Handbook of Batteries: Third Edition, 2002.

[4] J. Kleperis, G. Wójcik, A. Czerwinski, J. Skowronski, M. Kopczyk, M. Beltowska-Brzezinska, Electrochemical behavior of metal hydrides, J. Solid State Electrochem. 5 (2001) 229–249. doi:10.1007/s100080000149.

[5] M. Jacoby, Safer Lithium-Ion Batteries, Chem. Eng. News. 91 (2013) 33–37.

[6] M. Zhao, Q. Zheng, F. Wang, W. Dai, X. Song, Electrochemical performance of high specific capacity of lithium-ion cell LiV3O8//LiMn2O4 with LiNO3 aqueous solution electrolyte, Electrochim. Acta. 56 (2011) 3781–3784. doi:10.1016/j.electacta.2011.02.057.

[7] Q. Qu, L. Fu, X. Zhan, D. Samuelis, J. Maier, L. Li, S. Tian, Z. Li, Y. Wu, Porous LiMn2O4 as cathode material with high power and excellent cycling for aqueous rechargeable lithium batteries, Energy Environ. Sci. 4 (2011) 3985. doi:10.1039/c0ee00673d.

[8] W. Li, J.R. Dahn, D.S. Wainwright, Rechargeable Lithium Batteries with Aqueous Electrolytes., Science. 264 (1994) 1115–1118. doi:10.1126/science.264.5162.1115.

[9] G.J. Wang, H.P. Zhang, L.J. Fu, B. Wang, Y.P. Wu, Aqueous rechargeable lithium battery (ARLB) based on LiV3O8 and LiMn2O4 with good cycling performance, Electrochem. Commun. 9 (2007) 1873–1876. doi:10.1016/j.elecom.2007.04.017.

[10] W. Wu, S. Shanbhag, A. Wise, J. Chang, A. Rutt, J.F. Whitacre, High Performance TiP2O7 Based Intercalation Negative Electrode for Aqueous Lithium-Ion Batteries via a Facile Synthetic Route, J. Electrochem. Soc. 162 (2015) A1921–A1926. doi:10.1149/2.0071511jes.

[11] W. Wu, S. Shabhag, J. Chang, a. Rutt, J.F. Whitacre, Relating Electrolyte Concentration to Performance and Stability for NaTi2(PO4)3/Na0.44MnO2 Aqueous Sodium-Ion Batteries, J. Electrochem. Soc. 162 (2015) A803–A808. doi:10.1149/2.0121506jes.

[12] J.F. Whitacre, a. Tevar, S. Sharma, Na4Mn9O18 as a positive electrode material for an aqueous electrolyte sodium-ion energy storage device, Electrochem. Commun. 12 (2010) 463–466. doi:10.1016/j.elecom.2010.01.020.

[13] A. D. Tevar, J.F. Whitacre, Relating Synthesis Conditions and Electrochemical Performance for the Sodium Intercalation Compound $Na_4Mn_9O_{18}$ in Aqueous Electrolyte, J. Electrochem. Soc. 157 (2010) A870. doi:10.1149/1.3428667.

[14] H. Wang, K. Huang, Y. Zeng, F. Zhao, L. Chen, Stabilizing Cyclability of an Aqueous Lithium-Ion Battery $LiNi_{1/3}Mn_{1/3}Co_{1/3}O_2/Li_xV_2O_5$ by Polyaniline Coating on the Anode, Electrochem. Solid-State Lett. 10 (2007) A199. doi:10.1149/1.2748637.

[15] G.J. Wang, N.H. Zhao, L.C. Yang, Y.P. Wu, H.Q. Wu, R. Holze, Characteristics of an aqueous rechargeable lithium battery (ARLB), 52 (2007) 4911–4915. doi:10.1016/j.electacta.2007.01.051.

[16] R. Ruffo, F. La Mantia, C. Wessells, R.A. Huggins, Y. Cui, Electrochemical

characterization of LiCoO2 as rechargeable electrode in aqueous LiNO3 electrolyte, Solid State Ionics. 192 (2011) 289–292. doi:10.1016/j.ssi.2010.05.043.

[17] W. Tang, L.L. Liu, S. Tian, L. Li, Y.B. Yue, Y.P. Wu, S.Y. Guan, K. Zhu, Electrochemistry Communications Nano-LiCoO 2 as cathode material of large capacity and high rate capability for aqueous rechargeable lithium batteries, 12 (2010) 1524–1526. doi:10.1016/j.elecom.2010.08.024.

[18] M. Minakshi, P. Singh, D.R.G. Mitchell, T.B. Issa, K. Prince, A study of lithium insertion into MnO2 containing TiS2 additive a battery material in aqueous LiOH solution, Electrochim. Acta. 52 (2007) 7007–7013. doi:10.1016/j.electacta.2007.05.018.

[19] I. Stojković, N. Cvjetićanin, I. Pašti, M. Mitrić, S. Mentus, Electrochemical behaviour of V2O5 xerogel in aqueous LiNO3 solution, Electrochem. Commun. 11 (2009) 1512–1514. doi:10.1016/j.elecom.2009.05.043.

[20] H. Zhao, A. Yuan, B. Liu, S. Xing, X. Wu, J. Xu, High cyclic performance of V2O5@PPy composite as cathode of recharged lithium batteries, J. Appl. Electrochem. 42 (2012) 139–144. doi:10.1007/s10800-012-0380-x.

[21] M. Zhao, B. Zhang, G. Huang, H. Zhang, X. Song, Excellent rate capabilities of (LiFePO4/C)//LiV 3O8 in an optimized aqueous solution electrolyte, J. Power Sources. 232 (2013) 181–185. doi:10.1016/j.jpowsour.2013.01.026.

[22] X.H. Liu, T. Saito, T. Doi, S. Okada, J.I. Yamaki, Electrochemical properties of rechargeable aqueous lithium ion batteries with an olivine-type cathode and a Nasicon-type anode, J. Power Sources. 189 (2009) 706–710. doi:10.1016/j.jpowsour.2008.08.050.

[23] H. Wang, K. Huang, Y. Zeng, S. Yang, L. Chen, Electrochemical properties of TiP2O7 and LiTi2(PO4)3 as anode material for lithium ion battery with aqueous solution electrolyte, Electrochim. Acta. 52 (2007) 3280–3285. doi:10.1016/j.electacta.2006.10.010.

[24] W. Wu, A. Mohamed, J.F. Whitacre, Microwave Synthesized NaTi2(PO4)3 as an Aqueous Sodium-Ion Negative Electrode, J. Electrochem. Soc. 160 (2013) A497–A504. doi:10.1149/2.054303jes.

[25] W. Tang, L. Liu, Y. Zhu, H. Sun, Y. Wu, K. Zhu, An aqueous rechargeable lithium battery of excellent rate capability based on a nanocomposite of MoO3 coated with PPy and LiMn2O4, Energy Environ. Sci. 5 (2012) 6909. doi:10.1039/c2ee21294c.

[26] Y. Liu, B. Zhang, Y. Yang, Z. Chang, Z. Wen, Y. Wu, Polypyrrole-coated α-MoO3 nanobelts with good electrochemical performance as anode materials for aqueous supercapacitors, J. Mater. Chem. A. 1 (2013) 13582. doi:10.1039/c3ta12902k.

[27] W. Tang, Y. Zhu, Y. Hou, L. Liu, Y. Wu, K.P. Loh, H. Zhang, K. Zhu, Aqueous rechargeable lithium batteries as an energy storage system of superfast charging, Energy Environ. Sci. 6 (2013) 2093. doi:10.1039/c3ee24249h.

[28] H. Manjunatha, G.S. Suresh, T. V. Venkatesha, Electrode materials for aqueous rechargeable lithium batteries, J. Solid State Electrochem. 15 (2010) 431–445. doi:10.1007/s10008-010-1117-6.

[29] H. Kim, J. Hong, K. Park, H. Kim, S. Kim, K. Kang, Aqueous Rechargeable Li and Na Ion Batteries, (2014).

[30] N. Alias, A.A. Mohamad, Advances of aqueous rechargeable lithium-ion battery : A review, J. Power Sources. 274 (2015) 237–251. doi:10.1016/j.jpowsour.2014.10.009.

[31] A. Yuan, Q. Zhang, A novel hybrid manganese dioxide/activated carbon supercapacitor using lithium hydroxide electrolyte, Electrochem. Commun. 8 (2006) 1173–1178. doi:10.1016/j.elecom.2006.05.018.

[32] Y. Wang, Y. Xia, Hybrid Aqueous Energy Storage Cells Using Activated Carbon and Lithium-Intercalated Compounds, J. Electrochem. Soc. 153 (2006) A450. doi:10.1149/1.2140678.

[33] X. Liu, N. Zhang, J. Ni, L. Gao, Improved electrochemical performance of sol-gel method prepared Na 4Mn9O18 in aqueous hybrid Na-ion supercapacitor, J. Solid State Electrochem. 17 (2013) 1939–1944. doi:10.1007/s10008-013-2044-0.

[34] R.B. Shivashankaraiah, H. Manjunatha, K.C. Mahesh, G.S. Suresh, T. V. Venkatesha, Electrochemical Characterization of LiTi2(PO4)3 as Anode Material for Aqueous Rechargeable Lithium Batteries, J. Electrochem. Soc. 159 (2012) A1074–A1082. doi:10.1149/2.074207jes.

[35] Y. Cui, Y. Hao, W. Bao, Y. Shi, Q. Zhuang, Y. Qiang, Synthesis and Electrochemical Behavior of LiTi2(PO4)3 as Anode Materials for Aqueous Rechargeable Lithium Batteries, J. Electrochem. Soc. 160 (2012) A53–A59. doi:10.1149/2.060301jes.

[36] W. Wu, J. Yan, A. Wise, A. Rutt, J.F. Whitacre, Using Intimate Carbon to Enhance the Performance of NaTi2(PO4)3 Anode Materials: Carbon Nanotubes vs Graphite, J. Electrochem. Soc. 161 (2014) A561–A567. doi:10.1149/2.059404jes.

[37] A.I. Mohamed, N.J. Sansone, B. Kuei, N.R. Washburn, J.F. Whitacre, Using Polypyrrole Coating to Improve Cycling Stability of NaTi $_2$ (PO $_4$) $_3$ as an Aqueous Na-Ion Anode, J. Electrochem. Soc. 162 (2015) A2201–A2207. doi:10.1149/2.0961510jes.

[38] G. Pang, P. Nie, C. Yuan, L. Shen, X. Zhang, J. Zhu, B. Ding, Enhanced Performance of Aqueous Sodium-Ion Batteries Using Electrodes Based on the NaTi $_2$ (PO $_4$) $_3$ /MWNTs-Na 0.44 MnO 2 System, Energy Technol. 2 (2014) 705–712. doi:10.1002/ente.201402045.

[39] Z. Li, D. Young, K. Xiang, W.C. Carter, Y.-M. Chiang, Towards High Power High Energy Aqueous Sodium-Ion Batteries: The NaTi $_2$ (PO $_4$) $_3$ /Na 0.44 MnO 2 System, Adv. Energy Mater. 3 (2013) 290–294. doi:10.1002/aenm.201200598.

[40] Z. Li, D.B. Ravnsbæk, K. Xiang, Y.M. Chiang, Na3Ti2(PO4)3 as a sodium-bearing anode for rechargeable aqueous sodium-ion batteries, Electrochem. Commun. 44 (2014) 12–15. doi:10.1016/j.elecom.2014.04.003.

[41] V. Srinivasan, J. Newman, Discharge Model for the Lithium Iron-Phosphate Electrode, J. Electrochem. Soc. 151 (2004) A1517. doi:10.1149/1.1785012.

[42] J. Wu, F.G. Risalvato, F.-S. Ke, P.J. Pellechia, X.-D. Zhou, Electrochemical Reduction of Carbon Dioxide I. Effects of the Electrolyte on the Selectivity and Activity with Sn Electrode, J. Electrochem. Soc. 159 (2012) F353–F359. doi:10.1149/2.049207jes.

[43] M.C. Henstridge, E. Laborda, N. V. Rees, R.G. Compton, Marcus-Hush-Chidsey theory of electron transfer applied to voltammetry: A review, Electrochim. Acta. 84 (2012) 12–20. doi:10.1016/j.electacta.2011.10.026.

[44] H. Pan, Y. Shao, P. Yan, Y. Cheng, K.S. Han, Z. Nie, C. Wang, J. Yang, X. Li, P. Bhattacharya, K.T. Mueller, J. Liu, Reversible aqueous zinc/manganese oxide energy storage from conversion reactions, Nat. Energy. (2016) 16039. doi:10.1038/nenergy.2016.39.

[45] Y. Liu, B.H. Zhang, S.Y. Xiao, L.L. Liu, Z.B. Wen, Y.P. Wu, A nanocomposite of MoO3 coated with PPy as an anode material for aqueous sodium rechargeable batteries with excellent electrochemical performance, Electrochim. Acta. 116 (2014) 512–517. doi:10.1016/j.electacta.2013.11.077.

[46] M. Manickam, P. Singh, S. Thurgate, K. Prince, Redox behavior and surface characterization of LiFePO4 in lithium hydroxide electrolyte, J. Power Sources. 158

(2006) 646–649. doi:10.1016/j.jpowsour.2005.08.059.

[47] R. Benedek, M.M. Thackeray, A. Van De Walle, Pourbaix-like phase diagram for lithium manganese spinels in acid, Society. (2010) 369–374. doi:10.1039/b913226k.

[48] A. Caballero, J. Morales, O.A. Vargas, Electrochemical instability of LiV3O8 as an electrode material for aqueous rechargeable lithium batteries, J. Power Sources. 195 (2010) 4318–4321. doi:10.1016/j.jpowsour.2010.01.030.

[49] N.F.D. John N. Lalena, David A. Cleary, Everett E. Carpenter, Solid–Liquid Reactions, in: Inorg. Mater. Synth. Fabr., 2008: pp. 141–181.

[50] X. Zhang, W. Shyy, A. Marie Sastry, Numerical Simulation of Intercalation-Induced Stress in Li-Ion Battery Electrode Particles, J. Electrochem. Soc. 154 (2007) S21. doi:10.1149/1.2793718.

[51] A.C.C. Tseung, Gas evolution on porous electrodes, J. Appl. Electrochem. 15 (1985) 575–580. doi:10.1007/BF01059299.

[52] Y.G. Chirkov, Gas-generating porous electrodes at low overvoltages: Allowance for the outside-electrode limitations, Russ. J. Electrochem. 36 (2000) 465–471. doi:10.1007/BF02757407.

[53] Y.G. Chirkov, a a Chernenko, Gas-Generating Porous Electrodes : The Nature of the Low-Polarizability Portion in the Polarization Curves, Russ. J. Electrochem. 37 (2001) 467–476. doi:1023-1935/01/3705-0467.

[54] Y.G. Chirkov, V.I. Rostokin, Gas-Generating Porous Electrodes : Allowing for the Ohmic Limitations, 37 (2001) 848–856.

[55] A.G. Pshenichnikov, Y.G. Chirkov, V.I. Rostokin, Gas-generating porous electrodes: Chlorine generation in DSA at low and intermediate overpotentials, Russ. J. Electrochem. 38 (2002) 213–219. doi:10.1023/A:1016832702152.

[56] J. Luo, W. Cui, P. He, Y. Xia, Raising the cycling stability of aqueous lithium-ion batteries by eliminating oxygen in the electrolyte, Nat. Chem. 2 (2010). doi:10.1038/NCHEM.763.

[57] H. Kanoh, W. Tang, Y. Makita, K. Ooi, Electrochemical Intercalation of Alkali-Metal Ions into Birnessite-Type Manganese Oxide in Aqueous Solution, Langmuir. 13 (1997) 6845–6849. doi:10.1021/la970767d.

[58] J. Shao, X. Li, Q. Qu, Y. Wu, Study on different power and cycling performance of crystalline K xMnO 2·nH 2O as cathode material for supercapacitors in Li 2SO 4, Na 2SO 4, and K 2SO 4 aqueous electrolytes, J. Power Sources. 223 (2013) 56–61. doi:10.1016/j.jpowsour.2012.09.046.

[59] J.H. Albering, Structural Chemistry of Manganese Dioxide and Related Compounds, Handb. Batter. Mater. (2011) 989. doi:10.1002/9783527637188.ch3.

[60] A. Kozawa, K. Yamamoto, M. Yoshio, Electrochemistry of Manganese Oxides, 2011. doi:10.1002/9783527637188.ch4.

[61] Y. He, X. Yu, Y. Wang, H. Li, X. Huang, Alumina-coated patterned amorphous silicon as the anode for a Lithium-Ion battery with high Coulombic efficiency, Adv. Mater. 23 (2011) 4938–4941. doi:10.1002/adma.201102568.

[62] S. Xun, B. Xiang, a. Minor, V. Battaglia, G. Liu, Conductive Polymer and Silicon Composite Secondary Particles for a High Area-Loading Negative Electrode, J. Electrochem. Soc. 160 (2013) A1380–A1383. doi:10.1149/2.034309jes.

[63] F. Han, D. Li, W.-C. Li, C. Lei, Q. Sun, A.-H. Lu, Nanoengineered Polypyrrole-Coated Fe2O3 @C Multifunctional Composites with an Improved Cycle Stability as Lithium-Ion

Anodes, Adv. Funct. Mater. 23 (2013) 1692–1700. doi:10.1002/adfm.201202254.

[64]   F. Wu, S. Wu, R. Chen, J. Chen, S. Chen, Sulfur–Polythiophene Composite Cathode Materials for Rechargeable Lithium Batteries, Electrochem. Solid-State Lett. 13 (2010) A29. doi:10.1149/1.3290668.

[65]   C. Lei, F. Han, D. Li, W.-C. Li, Q. Sun, X.-Q. Zhang, A.-H. Lu, Dopamine as the coating agent and carbon precursor for the fabrication of N-doped carbon coated Fe3O4 composites as superior lithium ion anodes., Nanoscale. 5 (2013) 1168–75. doi:10.1039/c2nr33043a.

[66]   S.H. Ng, J. Wang, K. Konstantinov, D. Wexler, S.Y. Chew, Z.P. Guo, H.K. Liu, Spray-pyrolyzed silicon/disordered carbon nanocomposites for lithium-ion battery anodes, J. Power Sources. 174 (2007) 823–827. doi:10.1016/j.jpowsour.2007.06.165.

[67]   H. Zhou, Z.R. Tian, S.S. Ang, Improving the cycling stability of Na3V2(PO4)3 nanoparticle in aqueous sodium ion batteries by introducing carbon support, Mater. Renew. Sustain. Energy. 5 (2016) 1–9. doi:10.1007/s40243-016-0067-z.

[68]   J. Liu, D. Chang, P. Whitfield, Y. Janssen, X. Yu, Y. Zhou, J. Bai, J. Ko, K.W. Nam, L. Wu, Y. Zhu, M. Feygenson, G. Amatucci, A. Van Der Ven, X.Q. Yang, P. Khalifah, Ionic conduction in cubic Na3TiP3O9N, a secondary Na-ion battery cathode with extremely low volume change, Chem. Mater. 26 (2014) 3295–3305. doi:10.1021/cm5011218.

[69]   M. Pasta, C.D. Wessells, N. Liu, J. Nelson, M.T. McDowell, R.A. Huggins, M.F. Toney, Y. Cui, Full open-framework batteries for stationary energy storage, Nat. Commun. 5 (2014) 3007. doi:10.1038/ncomms4007.

[70]   J.J. Reilly, Metal Hydride Electrodes, Handb. Batter. Mater. Second Ed. (2011) 239–268. doi:10.1002/9783527637188.ch9.

[71]   S. Malkhandi, B. Yang, A.K. Manohar, G.K.S. Prakash, S.R. Narayanan, "Self-assembled monolayers of n-alkanethiols suppress hydrogen evolution and increase the efficiency of rechargeable iron battery electrodes." *Journal of the American Chemical Society* 135.1 (2012): 347-353.

[72]   J.M. Larcher, D., Courjal, P., Urbina, R. H., Gerand, B., Blyr, A., Du Pasquier, A., & Tarascon, Synthesis of MnO2 Phases from LiMn2O4 in Aqueous Acidic Media Mechanisms of Phase Transformations, Reactivity, and Effect of Bi Species, J. Electrochem. Soc. 145 (1998) 3392–3400.

[73]   K. Kinoshita, Carbons, Handbook of Battery Materials (2011) 989. doi:10.1002/9783527637188.ch10.

[74]   H. Kabbour, D. Coillot, M. Colmont, C. Masquelier, O. Mentré, α-Na3M2(PO4)3 (M = Ti, Fe): Absolute cationic ordering in NASICON-type phases, J. Am. Chem. Soc. 133 (2011) 11900–11903. doi:10.1021/ja204321y.

[75]   P. Simon, Y. Gogotsi, Materials for electrochemical capacitors., Nat. Mater. 7 (2008) 845–854. doi:10.1038/nmat2297.

[76]   F. Mauvy, E. Siebert, P. Fabry, Reactivity of NASICON with water and interpretation of the detection limit of a NASICON based Na+ ion selective electrode, Talanta. 48 (1999) 293–303. doi:10.1016/S0039-9140(98)00234-3.

[77]   S. Hasegawa, N. Imanishi, T. Zhang, J. Xie, A. Hirano, Y. Takeda, O. Yamamoto, Study on lithium/air secondary batteries-Stability of NASICON-type lithium ion conducting glass-ceramics with water, J. Power Sources. 189 (2009) 371–377. doi:10.1016/j.jpowsour.2008.08.009.

[78]   Y. Shimonishi, T. Zhang, N. Imanishi, D. Im, D.J. Lee, A. Hirano, Y. Takeda, O.

Yamamoto, N. Sammes, A study on lithium/air secondary batteries - Stability of the NASICON-type lithium ion conducting solid electrolyte in alkaline aqueous solutions, J. Power Sources. 196 (2011) 5128–5132. doi:10.1016/j.jpowsour.2011.02.023.

[79]   T. Kida, K. Shimanoe, N. Miura, N. Yamazoe, Stability of NASICON-based CO2 sensor under humid conditions at low temperature, Sensors Actuators, B Chem. 75 (2001) 179–187. doi:10.1016/S0925-4005(01)00549-4.

[80]   J. Yang, H. Wang, P. Hu, J. Qi, L. Guo, L. Wang, A High-Rate and Ultralong-Life Sodium-Ion Battery Based on NaTi2(PO4) 3 Nanocubes with Synergistic Coating of Carbon and Rutile TiO2, Small. 11 (2015) 3744–3749. doi:10.1002/smll.201500144.

[81]   K.G. Knauss, M.J. Dibley, W.L. Bourcier, H.F. Shaw, Ti(IV) hydrolysis constants derived from rutile solubility measurements made from 100 to 300 C, Appl. Geochemistry. 16 (2001) 1115–1128. doi:10.1016/S0883-2927(00)00081-0.

[82]   Y. V. Kolen'ko, K.A. Kovnir, A.I. Gavrilov, A. V. Garshev, J. Frantti, O.I. Lebedev, B.R. Churagulov, G. Van Tendeloo, M. Yoshimura, Hydrothermal synthesis and characterization of nanorods of various titanates and titanium dioxide, J. Phys. Chem. B. 110 (2006) 4030–4038. doi:10.1021/jp055687u.

[83]   Y. Wang, H. Liu, Preparation and characterizations of Na 2 Ti 3 O 7 , H 2 Ti 3 O 7 and TiO 2 nanobelts, Adv. Mater. Res. 306–307 (2011) 1233–1237. doi:10.4028/www.scientific.net/AMR.306-307.1233.

[84]   V. S. Kurazhkovskaya, A.I. Orlova, V.I. Petkov, D. V. Kemenov, L.N. Kaplunnik, IR study of the structure of rhombohedral zirconium and alkali metal orthophosphates, J. Struct. Chem. 41 (2000) 61–66.

[85]   F. Sun, R. Wang, H. Jiang, W. Zhou, Synthesis of sodium titanium phosphate at ultra-low temperature, Res. Chem. Intermed. 39 (2013) 1857–1864. doi:10.1007/s11164-012-0720-9.

[86]   V.I. Pet'kov, E.A. Asabina, A. V. Markin, N.N. Smirnova, Synthesis, characterization and thermodynamic data of compounds with NZP structure, J. Therm. Anal. Calorim. 91 (2008) 155–161. doi:10.1007/s10973-007-8370-7.

[87]   Y.W.L. Lim, Y. Tang, Y.H. Cheng, Z. Chen, Morphology, crystal structure and adsorption performance of hydrothermally synthesized titania and titanate nanostructures., Nanoscale. 2 (2010) 2751–2757. doi:10.1039/c0nr00440e.

[88]   C.M. Rodrigues, O.P. Ferreira, O.L. Alves, Interaction of sodium titanate nanotubes with organic acids and base: Chemical, structural and morphological stabilities, J. Braz. Chem. Soc. 21 (2010) 1341–1348. doi:10.1590/s0103-50532010000700021.

[89]   Z. Huang, L. Liu, L. Yi, W. Xiao, M. Li, Q. Zhou, G. Guo, X. Chen, H. Shu, X. Yang, X. Wang, Facile solvothermal synthesis of NaTi2(PO4)3/C porous plates as electrode materials for high-performance sodium ion batteries, J. Power Sources. 325 (2016) 474–481. doi:10.1016/j.jpowsour.2016.06.066.

[90]   J.F. Whitacre, S. Shanbhag, A. Mohamed, a. Polonsky, K. Carlisle, J. Gulakowski, W. Wu, C. Smith, L. Cooney, D. Blackwood, J.C. Dandrea, C. Truchot, A Polyionic, Large-Format Energy Storage Device Using an Aqueous Electrolyte and Thick-Format Composite NaTi2(PO 4)3/Activated Carbon Negative Electrodes, Energy Technol. 3 (2015) 20–31. doi:10.1002/ente.201402127.

[91]   A. Karantonis, Numerical Solution of Reaction-Diffusion Equations by the Finite Difference Method, (2001).

[92]   A. Soffer, M. Folman, The electrical double layer of high surface porous carbon

electrode, J. Electroanal. Chem. Interfacial Electrochem. 38 (1972) 25–43. doi:10.1016/S0022-0728(72)80087-1.

[93] Q. Qu, Y. Zhu, X. Gao, Y. Wu, Core-shell structure of polypyrrole grown on V2O5 nanoribbon as high performance anode material for supercapacitors, Adv. Energy Mater. 2 (2012) 950–955. doi:10.1002/aenm.201200088.

[94] W. Tang, X. Gao, Y. Zhu, Y. Yue, Y. Shi, Y. Wu, K. Zhu, A hybrid of V2O5 nanowires and MWCNTs coated with polypyrrole as an anode material for aqueous rechargeable lithium batteries with excellent cycling performance, J. Mater. Chem. 22 (2012) 20143. doi:10.1039/c2jm34563c.

[95] G.G. Wallace, G.M. Spinks, L.A.P. Kane-Maguire, P.R. Teasdale, Conductive Electroactive Polymers: Intelligent Polymer Systems, 2009.

[96] P. Novák, K. Müller, K.S. V. Santhanam, O. Haas, Electrochemically Active Polymers for Rechargeable Batteries., Chem. Rev. 97 (1997) 207–282.

[97] R. Holze, Y.P. Wu, Electrochimica Acta Intrinsically conducting polymers in electrochemical energy technology : Trends and progress, 122 (2014) 93–107. doi:10.1016/j.electacta.2013.08.100.

[98] J.F. Mike, J.L. Lutkenhaus, Recent advances in conjugated polymer energy storage, J. Polym. Sci. Part B Polym. Phys. 51 (2013) 468–480. doi:10.1002/polb.23256.

[99] N. Dimov, M. Yoshio, Towards creating reversible silicon-based composite anodes for lithium ion batteries, J. Power Sources. 174 (2007) 607–612. doi:10.1016/j.jpowsour.2007.06.118.

[100] M. Wu, X. Xiao, N. Vukmirovic, S. Xun, P.K. Das, X. Song, P. Olalde-Velasco, D. Wang, A.Z. Weber, L.-W. Wang, V.S. Battaglia, W. Yang, G. Liu, Toward an ideal polymer binder design for high-capacity battery anodes., J. Am. Chem. Soc. 135 (2013) 12048–56. doi:10.1021/ja4054465.

[101] M.K. Song, Y.T. Kim, B.S. Kim, J. Kim, K. Char, H.W. Rhee, Synthesis and characterization of soluble polypyrrole doped with alkylbenzenesulfonic acids, Synth. Met. 141 (2004) 315–319. doi:10.1016/j.synthmet.2003.07.015.

[102] S. Patoux, C. Masquelier, Lithium insertion into titanium phosphates, silicates, and sulfates, Chem. Mater. 14 (2002) 5057–5068. doi:10.1021/cm0201798.

[103] A. Rudge, J. Davey, I. Raistrick, S. Gottesfeld, J.P. Ferraris, Conducting polymers as active materials in electrochemical capacitors, J. Power Sources. 47 (1994) 89–107. doi:10.1016/0378-7753(94)80053-7.

[104] X. Ren, P.G. Pickup, Ion transport in polypyrrole and a polypyrrole/polyanion composite, J. Phys. Chem. 97 (1993) 5356–5362. doi:10.1021/j100122a029.

[105] C. Basavaraja, N.R. Kim, E.A. Jo, R. Pierson, D.S. Huh, A. Venkataraman, Transport Properties of Polypyrrole Films Doped with Sulphonic Acids, 30 (2009).

[106] C.J. Wen, B.A. Boukamp, R.A. Huggins, W. Weppner, Thermodynamic and Mass Transport Properties of "LiAl," J. Electrochem. Soc. 126 (1979) 2258. doi:10.1149/1.2128939.

[107] K. Jurewicz, E. Frackowiak, F. Béguin, Towards the mechanism of electrochemical hydrogen storage in nanostructured carbon materials, Appl. Phys. A Mater. Sci. Process. 78 (2004) 981–987. doi:10.1007/s00339-003-2418-8.

[108] A.S. Oberoi, Reversible Electrochemical Storage of Hydrogen in Activated Carbons From Victorian Brown Coal and Other Precursors, RMIT University, 2015.

[109] T.C. Girija, M. V. Sangaranarayanan, Polyaniline-based nickel electrodes for

electrochemical supercapacitors-Influence of Triton X-100, J. Power Sources. 159 (2006) 1519–1526. doi:10.1016/j.jpowsour.2005.11.078.

[110] S. Devaraj, N. Munichandraiah, The effect of nonionic surfactant Triton X-100 during electrochemical deposition of MnO2 on its capacitance properties., J. Electrochem. Soc. 154 (2007) A901–A909. doi:10.1149/1.2759618.

[111] C. Gouveia-Caridade, C.M.A. Brett, The influence of Triton-X-100 surfactant on the electroanalysis of lead and cadmium at carbon film electrodes - An electrochemical impedance study, J. Electroanal. Chem. 592 (2006) 113–120. doi:10.1016/j.jelechem.2006.05.005.

[112] Z. Zhang, C. Qu, T. Zheng, Y. Lai, J. Li, Effect of Triton X-100 as Dispersant on Carbon Black for LiFePO4 Cathode, Int. J. Electrochem. Sci. 8 (2013) 6722–6733.

[113] A.V. Makievski, V.B. Fainerman, P. Joos, Dynamic Surface Tension of Micellar Triton X-100 Solutions by the Maximum-Bubble-Pressure Method, J. Colloid Interface Sci. 166 (1994) 6–13. doi:10.1006/jcis.1994.1264.